

© 2017

DANIELLE GROLMAN

ALL RIGHTS RESERVED

SELF-ORGANIZATION AND CONTROLLED SPATIAL DISTRIBUTION OF
CELLULOSIC NANOFILLERS IN POLYMER THIN FILMS

A Dissertation

Presented to

The Graduate Faculty of The University of Akron

In Partial Fulfillment

of the Requirements for the Degree

Doctor of Philosophy

Danielle Grolman

May, 2017

SELF-ORGANIZATION AND CONTROLLED SPATIAL DISTRIBUTION OF
CELLULOSIC NANOFILLERS IN POLYMER THIN FILMS

Danielle Grolman

Dissertation

Approved:

Accepted:

Advisor
Dr. Alamgir Karim

Department Chair
Dr. Sadhan Jana

Committee Member
Dr. Sadhan Jana

Dean of the College
Dr. Eric Amis

Committee Member
Dr. Younjin Min

Dean of the Graduate School
Dr. Chand Midha

Committee Member
Dr. Yu Zhu

Date

Committee Member
Dr. Jutta Luettmmer-Strathmann

ABSTRACT

Polymer nanocomposites have generated widespread interest towards the development of engineered multifunctional materials and novel hybrid assemblies for high performance applications. The addition of anisotropic nanofillers in a polymer matrix can potentially modify the material's optical, thermal, electrical, or mechanical properties due to the high surface area to volume ratio, with increasing advances and focused efforts toward the development of environmentally friendly, reinforced materials from sustainable resources. In this regard, cellulose nanocrystals (CNCs) are promising nanomaterials derived from the world's most abundant natural polymer. However, one of the key challenges and current barriers towards commercialization is controlling uniform dispersion within the polymer matrix in order to achieve effective reinforcement. The objective of this research aims to gain a fundamental understanding on how to control the dispersion and spatial organization of cellulose nanocrystals in polymer thin films by tailoring the thermodynamic interactions between the host polymer matrix and rod-like nanoparticles.

The first part of this dissertation focuses on developing a facile strategy to manipulate the spatial distribution of cellulose nanocrystals in polymer thin films, which are highly susceptible to particle aggregation due to strong hydrogen bonding interactions. A model symmetric diblock copolymer poly(styrene-block-methyl methacrylate) (PS-*b*-PMMA) was utilized as an ideal nanostructured template to selectively sequester and

organize the cellulose nanocrystals *via* directed self-assembly wherein the CNCs were subjected to a degree of confinement within the multilayered structure. The incorporation of anisotropic nanofillers was observed to perturb the block copolymer (BCP) morphology at relatively low nanofiller concentrations. Surface chemistry modification of the nanoparticle was employed to alter interparticle and particle-polymer interactions and subsequently control nanoparticle distribution. Furthermore, significant enhancement in the mechanical performance of these polymer nanocomposite systems were attributed to the multiscale interfacial interactions between the polymer matrix and fillers.

To gain insight into the stabilization and wetting behavior of polymer nanocomposite thin films, the presence of anisotropic nanofillers in a polymer matrix was investigated on non-wetting, low surface energy substrates. Control measurements on the film morphology of homopolymer systems without nanoparticles exhibited immediate film rupture and dewetting due to unfavorable interactions between the substrate and polymer thin film. The addition of cellulose nanocrystals was observed to significantly retard dewetting kinetics and resulted in dewetting suppression where thin film stabilization was achieved at a critical particle threshold. These findings exploit the tunable wettability and nanoparticle-induced stabilization of nanoscale films without any required substrate modification which could have significant ramifications towards the development of novel functional coatings.

DEDICATION

To my parents, Kerry and Mylan Grolman, my brothers Joshua, Caleb, Micah, and my sister Rachael.

ACKNOWLEDGEMENTS

I would like to convey my sincere gratitude to those individuals that helped me throughout my PhD. To my advisor, Dr. Alamgir Karim, for the wonderful opportunity to work in his research group and being allotted the creative freedom to pursue any research avenue that was of interest to me. I'd also like to extend my appreciation to my committee members Dr. Sadhan Jana, Dr. Younjin Min, Dr. Yu Zhu, Dr. Jutta Luettmmer-Strathmann, Dr. Mesfin Tsige, and Dr. Matthew Shawkey for their valuable feedback and taking time out of their busy schedules for my proposal and dissertation.

I would like to acknowledge my collaborators at NIST and McMaster University, in particular Stephanie Kedzior and Dr. Emily Cranston for synthesizing the polymer grafted nanoparticles, as well as Dr. Chelsea Davis, Dr. Bharath Natarajan, and Dr. Jeffrey Gilman for fruitful discussions. Special acknowledgement to Dr. Chelsea Davis for her contagious enthusiasm in our collaborative work that has been an absolute pleasure to work with. I also would like to express my sincere gratitude to Dr. Guangcui Yuan and Dr. Joseph Strzalka at NIST Center for Neutron Research and Argonne National Laboratory for an incredible experience running experiments at the beamlines in state-of-the-art facilities.

I would also like to acknowledge Dr. Zhorro Nikolov and Rong Bai for their help with instrumentation training and Ed Laughlin for his assistance on building a customized assembly. I want to thank all of my groupmates in KRG for making the last five years so

memorable with special mention to my group mates Dr. Saumil Samant and Namrata Salunke. I'd also like to extend special thanks to the administrative assistants and to my wonderful group of friends in Akron.

And last but certainly not least, my heartfelt gratitude to my family for their endless support throughout this journey.

TABLE OF CONTENTS

	Page
LIST OF FIGURES.....	x
CHAPTER	
I. INTRODUCTION.....	1
II. BACKGROUND AND LITERATURE REVIEW.....	7
2.1 Fundamentals of Dewetting and Wetting.....	7
2.2 Polymer Nanocomposites.....	14
2.3 Cellulose Nanocrystals	27
2.4 Strategies for Controlling Spatial Distribution.....	31
III. CONTROLLED DISPERSION AND ORGANIZATION OF CELLULOSE NANOCRYSTALS USING BLOCK COPOLYMER SCAFFOLDS	46
3.1 Introduction.....	46
3.2 Experimental Section.....	49
3.3 Results and Discussion.....	55
3.4 Conclusion.....	89
IV. NANOPARTICLE-INDUCED STABILIZATION AND WETTABILITY OF POLYMER THIN FILMS.....	91
4.1 Introduction.....	91
4.2 Experimental Section.....	94
4.3 Results and Discussion.....	96
4.4 Conclusion.....	113

V. MECHANICAL REINFORCEMENT OF SUB-MICRON POLYMER NANOCOMPOSITE FILMS VIA BUCKLING MECHANICS.....	115
5.1 Introduction.....	115
5.2 Experimental.....	117
5.3 Results and Discussion.....	120
5.4 Conclusion.....	128
VI. SUMMARY.....	130
REFERENCES.....	134

LIST OF FIGURES

Figure	Page
2.1. Schematic illustrating various different wetting and stability cases for a liquid on a substrate where A and E are the initial states, B and D denotes the equilibrium states, and C represents the excess free energy as a function of thickness, h. The initial state A represents a drop placed on the substrate while E describes a thin film that is forced to spread on the solid substrate in its initial state.....	9
2.2. Optical micrographs displaying morphology evolution of PS ultrathin film on PDMS exposed to solvent vapor as a function of time. The representative images display different stages of dewetting from a) initiation of holes, b) hole growth, and c) hole coalescence and ribbon formation to d) droplet formation.	11
2.3. Thin films with a) monofunctional PS chains and b) difunctional PS chains where the black circles denote ionic end groups	13
2.4. Schematic of polymer nanocomposites comprised of a polymer matrix and nanoparticles	15
2.5. Examples of different nanoparticle geometries (spheres, rods, plates) with its respective surface area to volume ratio.....	17
2.6. RAFT polymerization to synthesize a bimodal brush.....	19
2.7. Phase diagram of nanoparticle morphologies compiled from literature with regions of different states	20
2.8. Young's modulus of carbon nanotube/poly(methyl methacrylate) composite material as a function of CNT aspect ratio from MD simulations and micromechanical model	22
2.9. TEM micrographs of MWCNT-PS thin film with crack initiation and propagation induced by local thermal stresses	25
2.10. Schematic illustrating the rupture behavior of a PAN-CNT fiber in which the mechanism involves a) the formation of voids under tension, b) crazing fibrils form as the void extends and CNTs align parallel to the fibril direction, c) crazing extension with well-aligned CNTs along the crazing, and d) composite fiber rupture and CNT pull-out.....	26

2.11. Schematic illustrating the extraction of cellulose nanocrystals derived from plants.....	28
2.12. Molecular structure of cellulose.....	29
2.13. Representative model consisting of rigid phase (R) and soft phase (S).....	30
2.14. a) Microlayer coextrusion assembly with multilayered PC-coPVDF films comprised of b) 32 layers and c) 256 layers	33
2.15. (a) Equilibrium morphologies of microphase-separated A-B diblock copolymers as a function of increasing volume fraction f of block A and (b) phase diagram of A-B diblock copolymer predicted by self-consistent theory	35
2.16. Scenarios of symmetric wetting, asymmetric wetting, and neutral wetting of BCP thin films due to preferential surface energetics and relative film thickness.....	37
2.17 Nanoparticle localization in block copolymer systems dependent on the selective or non-selective nature of the particles with the BCP components and the nanoparticle size relative to the polymer radius of gyration.....	38
2.18. Cross-sectional TEM micrographs of a) PS-grafted gold NPs in PS- <i>b</i> -PVP and its corresponding b) histogram displaying the majority of particles localized in the center of the PS domain, c) PS ad PVP grafted gold NPs in PS- <i>b</i> -PVP with its d) corresponding histogram of particle location at the interface. The histogram represents the number of particles as a function of the normalized distance from the center of the PS domain.....	40
2.19. a) Schematic of nanorods in lamellar block copolymer with nanorods confined within the center of PMMA domains and b) frequency distribution of nanorod orientation with respect to the lamellae	42
2.20. Representative model of nanorod in lamellae block copolymer at orientation a) 0° and b) θ° with respect to lamellae. The arrows represent the force exerted to accommodate for the nanorod.	43
3.1 a) Molecular structure of poly(styrene- <i>block</i> -methyl methacrylate), b) cellulose nanocrystals “unmodified CNCs”, and c) DMF	50

3.2 Synthesis of PMMA-grafted-CNCs	51
3.3. Modified flowcoating assembly with a heating stage placed below the silicon wafer to facilitate solvent evaporation and generate films of uniform thickness	52
3.4. Grazing incidence small angle X-ray scattering (GISAXS) geometry.....	54
3.5. Typical geometry of neutron reflectivity with a reflectivity curve and model obtained from fitting.....	55
3.6. AFM micrographs of height and phase images displaying pure cellulose thin films drop cast on silicon substrates from dilute aqueous suspensions	56
3.7. TGA curve of unmodified CNCs with sulfate half-ester groups from hydrolysis reaction.....	58
3.8. Prepared solutions of unmodified CNCs in glass vials of a) polystyrene and b) poly(methyl methacrylate) after sonication.....	59
3.9 AFM height (a-c) and phase (d-f) images obtained with tapping mode as a function of unmodified CNC concentration in PMMA homopolymer. The nanorod concentration is varied from (a,d) 1wt%, (b,e) 5wt%, and (c,f) 10wt% in PMMA.....	61
3.10 FTIR absorbance spectra of cellulose nanocrystals in PS-b-PMMA with varying CNC concentration	63
3.11 2D Grazing Incidence Small Angle X-ray Scattering (GISAXS) patterns revealing morphology of annealed block copolymer thin films with the incorporation of unmodified CNCs as a function of nanorod concentration at a) 0wt% (neat BCP film), b) 0.5wt% CNCs, c) 1wt% CNCs, d) 2wt% CNCs, e) 5wt% CNCs, and f) 10wt% CNCs. GISAXS measurements were taken above the film critical angle such that the entire film is probed.	65
3.12 GISAXS 1D profiles which reflect out-of-plane linecuts offset for each nanofiller concentration in PS-b-PMMA. Film thickness is approximately 400nm	68
3.13 TEM images of BCP cross-sectional profiles prepared by a focused ion beam (FIB) lift-out technique. The representative micrographs of annealed a) neat BCP thin film with lamellar microdomains ordered parallel to the substrate and b) PS-b-PMMA with addition of 5wt% unmodified CNCs.....	70
3.14. AFM phase images of PMMA-grafted-CNCs in a PMMA matrix in which the particle dispersion state is studied as a function of grafting density and nanorod concentration.	74

3.15. AFM Height images of MD PMMA-g-CNCs in BCP.....	75
3.16. Height profile corresponding to AFM linecuts across the holes which correspond to a step height of L_0	77
3.17. Neutron reflectivity profiles of annealed dPS-b-PMMA thin films with the addition of a) unmodified CNCs, b) PMMA-grafted-CNCs of low grafting density (LD), c) PMMA-grafted- CNCs of medium grafting density (MD), and d) PMMA-grafted- CNCs of high grafting density (HD). The BCP nanostructure is studied as a function of varying nanorod concentration at 1wt%, 5wt%, 10wt%, and 20wt% CNCs. The raw data is represented by the circles and solid lines corresponds to the fit. SLD profiles are shown as insets.....	78
3.18. Domain spacing as a function of CNC nanofiller concentration for unmodified CNCs and PMMA-grafted-CNCs of low grafting density (LD), medium grafting density (MD), and high grafting density (HD).....	81
3.19. Measured interfacial width as a function of CNC nanofiller concentration for unmodified CNCs (u-CNC) and PMMA-grafted-CNCs of low grafting density (LD), medium grafting density (MD), and high grafting density (HD).	83
3.20. Illustration of a possible scenario of a random orientation of PMMA-grafted-CNCs in annealed diblock copolymer thin films which is unaffected by domain swelling or increased layer thickness. The length of an individual cellulosic nanorod is approximately ten times larger than each PS and PMMA layer ($L_0/2$)	85
3.21. Schematic of a soft lithography strategy to generate well-ordered arrays of cellulose nanocrystals through patterned in-plane confinement.....	86
3.22. AFM phase micrographs of 1 wt% PMMA-grafted-CNCs in PMMA homopolymer with average molecular weight of 3 kg/mol after thermal annealing at 140°C for A) 10 min and b) 16 hrs. Scale bar is 2 μm	87
3.23 AFM phase micrographs of 1 wt% PMMA-grafted-CNCs in PMMA homopolymer with molecular weight of 30 kg/mol. A) 10 min, b) 4 h and c) 16 h.....	88
4.1. Optical micrographs of neat PMMA annealed on SiO _x of molecular weight 3 kg/mol for film thickness of a) 40 nm and b) 100 nm and PMMA molecular weight 15 kg/mol for film thickness of c) 40 nm and d) 100 nm.....	97
4.2. Schematic of experimental approach to determine equilibrium dewet morphology.....	98
4.3. Optical micrograph of poly(methyl methacrylate) on PDMS substrate a) before thermal annealing and b) after thermal annealing at 180°C for 24 hours....	100

4.4. Optical micrographs of annealed thin films of a) PMMA, b) PMMA with 1wt% unmodified CNCs, c) PMMA with 2wt% unmodified CNCs, and d) PMMA with 5wt% unmodified CNCs.	102
4.5. Optical micrographs of annealed thin films of a) PMMA, b) PMMA with 1wt% HD PMMA-grafted-CNCs, c) PMMA with 2wt% HD PMMA-grafted-CNCs, and d) PMMA with 5wt% HD PMMA-grafted-CNCs.	103
4.6. Net polymer area fraction as a function of nanofiller concentration for unmodified CNCs (u-CNC) and HD PMMA-grafted-CNCs in poly(methyl methacrylate) homopolymer of molecular weight 15 kg/mol.....	104
4.7. Net area fraction of polymer as a function of nanofiller concentration from 0 to 10wt% for unmodified CNCs in PMMA. The molecular weight of PMMA was varied from 15 kg mol ⁻¹ (triangular symbols) to 30 kg mol ⁻¹ (squares).....	106
4.8. Optical micrographs of annealed a) poly(styrene) and b) PS-b-PMMA (average molecular weight 37 kg/mol) on PDMS	108
4.9. Optical micrographs of PS-b-PMMA a) after film transfer (prior to annealing), and b) annealed PS-b-PMMA (neat system) with c,d) 1 mass% CNCs, e,f) 2 mass% CNCs, g,h) 5 mass% CNCs, where c,e,g are unmodified CNCs (u-CNCs) and d,f,h are PMMA-grafted-CNCs.....	110
4.10. AFM height image of annealed PS-b-PMMA with a) 10wt% HD PMMA-grafted-CNCs and b) corresponding line cut extracted from the height profile.....	112
5.1. Sodium chloride (NaCl) window utilized as an alternative substrate for film transfer to different substrates. The rectangular sections denote the films cast directly on the surface via flowcoating.	119
5.2. Schematic of buckling with a system comprised of a rigid polymer film of thickness h on a soft elastomer substrate. A small compressive strain applied to the system results in periodic buckling with wavelength due to large difference in moduli....	121
5.3. Optical micrographs of polymer nanocomposite system after floating films onto PDMS to confirm homogeneous films before applying compressive strain for systems containing varying concentrations of CNCs in PMMA at a) 0 wt% (neat PMMA), b) 1 wt% CNCs, c) 5 wt% CNCs, and d) 10 wt% CNC.....	122
5.4. Optical micrographs of unmodified CNCs/PMMA system after applying compressive strain for thin film systems with varying concentrations of CNCs in PMMA at a) 0 wt% (neat PMMA), b) 1 wt% CNCs, and c) 5 wt% CNCs.....	123

5.5. Optical micrographs of PMMA-grafted-CNCs/PMMA system after applying compressive strain for each thin film system with varying concentrations of CNCs in PMMA at a) 1 wt% CNCs, b) 5 wt% CNCs, and c) 10 wt% CNCs.....124

5.6. Elastic moduli calculated from buckling wavelength as a function of nanofiller concentrations for the thin film systems of unmodified CNCs (u-CNC) in PMMA and PMMA-grafted CNCs of low grafting density in PMMA homopolymer...125

5.7. Schematic representation of different polymer thin film systems on silicon substrates comprised of poly(methyl methacrylate) homopolymer and poly(styrene-block-methyl methacrylate) in the as-cast and annealed states.....126

5.8. Optical micrographs of annealed BCP films transferred to PDMS from the salt crystal substrate with a scale bar of a) 50 μm and b) 200 μm127

CHAPTER I

INTRODUCTION

To be at the forefront of scientific and technological innovation, there is a continuous impetus to develop high-performance materials to meet the rising demands and needs of society. As technology continues to advance, more stringent demands are being placed on optimization of material performance and durability to generate devices with increasingly smaller dimensions that are thinner and lightweight. Nanoscale thin films have enormous technological potential in applications ranging from optical coatings to dielectric layers to microelectronics with characteristic properties that may deviate from the bulk materials. Whether utilized as coatings to alter substrate wetting properties, tailor adhesion properties, or protect metal surfaces from rust, it becomes crucial to maintain a smooth, homogeneous film throughout processing and its use. However, polymer thin films are often heated above its glass transition temperature wherein thermodynamically unfavorable interactions between the polymer film and substrate, heterogeneities, and/or residual stresses within the film can lead to film rupture where the film can spontaneously break up into droplets through a phenomenon known as *dewetting*.¹⁻⁵ This phenomenon has attracted much interest in the scientific community on the stabilization of polymer thin films to investigate viable routes to suppress dewetting or develop techniques to control the self-organization process through substrate modification⁶ or confinement⁷⁻¹⁰ for

instance. While thick films can be stabilized due to gravity, intermolecular forces begin to influence and govern film stability as films approach molecular dimensions.¹¹ In this regard, it becomes of critical importance to gain a fundamental understanding on how a liquid wets the solid substrate and what underlying intermolecular forces govern thin film stability.

Nanoscale films with confined geometry exhibit unique physical or thermal properties that can deviate from the bulk material response.¹²⁻¹⁵ To meet the everchanging needs of society, there exists a rising demand in the development of high performance, lightweight materials by fabrication of multicomponent systems for applications including nanoscale sensors, barrier coatings, or self-healing materials. Multiphase polymer nanocomposites (PNCs), which are generally comprised of a host matrix and dispersed phase, have emerged as a prominent area in the field of nanotechnology.¹⁶ The presence of particles with dimensions at the nanoscale (<100 nm) has the unique capability to induce intrinsic property change with a relatively low filler concentration due to the high surface area to volume ratio. Most notably, this allows for mechanical reinforcement of polymeric materials with significant weight reduction in comparison to conventional additives. The nanoscale size features of the particles have been demonstrated to significantly enhance the thermal stability, mechanical integrity, electrical conductivity, and optical properties of the polymer system. Nanoparticles such as montmorillonite nanoclays, polyhedral oligomeric silsesquioxane (POSS), carbon nanotubes, silica, and titanium oxide have been utilized in research and development to fabricate hybrid multicomponent materials with enhanced gas barrier properties,¹⁷ flame-retardancy,^{18,19} or structural properties.^{20,21} However, the macroscopic properties of polymer nanocomposites are controlled by the

constituent nanomaterials and influenced by variables such as the particle spatial arrangement, NP orientation, and the degree of interactive strengths between the polymer and nanofillers which yield interfacial characteristics. Control over the homogeneous dispersion of nanoparticles and the controlled assembly of constituents remains a current challenge and poses limitations in converging technologies wherein high-throughput manufacturing processes and high-resolution characterization are desired for commercialization.

Furthermore, greener approaches have been recently pursued for implementation to meet environmental regulations by developing nanomaterials that are derived from renewable sources.²²⁻²⁴ Cellulose is the most abundant biopolymer in the world and cellulose nanocrystals (model 1-D anisotropic materials) offer a new route to product development due to its biocompatibility, low density, biodegradability, and impressive mechanical properties. Incorporation of cellulose nanocrystals in polymeric systems to create novel sustainable nanomaterials have shown great potential as effective reinforcing agents.²⁵⁻²⁷ Recent studies have recognized the natural strength of these biodegradable nanomaterials for use as fillers in composite structures in drug delivery systems,²⁸ water purification membranes,²⁹ and as templates for recyclable printed electronics.³⁰ However, one of the main challenges in property enhancement or system optimization is the susceptibility of cellulose to aggregate due to strong intramolecular and intermolecular hydrogen bonding interactions between the individual cellulosic fillers.³¹ In this regard, various strategies seek to improve the dispersion of the particles as well as the compatibility with the host polymer matrix *via* surface functionalization techniques.

The objective of this work was to design novel multiphase materials with controlled nanorod distribution into well-defined structured arrays through self-organization of cellulose nanocrystals. The self-assembly behavior of polymer systems provides a versatile platform to generate engineered structures with nanoscale feature sizes. Diblock copolymers are a class of functional materials comprised of two chemically distinct polymers connected by a covalent bond, which can microphase separate into a wide array of morphologies such as spheres, cylinders, lamellae, and gyroid structures. The generated nanostructures can vary from 5 to 100 nm and are dependent on the interaction parameter, degree of polymerization, and the volume fraction of the block components. To that end, block copolymers can act as ideal nanostructured templates due to their ability to selectively sequester and organize nanofillers. A self-assembled lamellar block copolymer ordered parallel to the substrate was utilized in this study as an efficient platform to create multi-layer thin film sheets with tailored functionality in-lieu of traditional multi-layer co-extrusion or layer-by-layer techniques. The interparticle interactions between cellulose nanocrystals (CNCs) and particle-polymer interactions were tailored by utilizing polymer grafted nanoparticles. Through microscopy and X-ray scattering techniques, the spatial organization of CNCs was examined in a model diblock copolymer poly(styrene-block-methyl methacrylate) (PS-*b*-PMMA) as a function of nanofiller concentration and grafting density through the interplay of entropic and enthalpic driving forces.

Furthermore, a novel strategy to control polymer thin film dewetting was demonstrated through the incorporation of anisotropic nanofillers in a polymer matrix on non-wetting, ultralow surface energy flexible substrates. The presence of cellulose nanocrystals in thermoplastics resulted in the stabilization of thin films, in comparison to

thermal induced dewetting for neat homopolymer systems. Film stabilization was achieved at a critical nanorod concentration threshold, which was attributed to strong hydrogen bonding interactions between the nanorods and polymer matrix. This was further extended to multilayered nanostructures attained through the quasi 2D organization of cellulose nanocrystals directed by self-assembly of diblock copolymers. This demonstration of nanoparticle-induced stabilization has important technological significance in a broad array of applications by providing a more universal approach to increase the compatibility of the surface while minimizing additional processing steps.

Finally, the mechanical properties of sub-micron polymer nanocomposite (PNC) thin films were characterized *via* Strain Induced Elastic Buckling Instability for Mechanical Measurements (SIEBIMM). This buckling mechanics approach entailed the application of a small compressive strain to the PNC thin film on a pre-stretched PDMS elastomeric substrate. The large difference in moduli between the rigid polymer film and flexible substrate resulted in a periodic buckling wavelength which was correlated to the Young's modulus of the nanocomposite film for varying nanofiller concentrations. The modulus was studied as a function of nanofiller concentration for each CNC system and grafting density and related to the nanoparticle dispersion states.

This dissertation is organized as follows. In Chapter I, a detailed background discussion is given and a comprehensive literature review is provided in Chapter II on polymer nanocomposites and subsequent structure-property relationships. In Chapter III, the dispersion and spatial arrangement of cellulose nanocrystals is controlled within a polymer matrix to tailor thermodynamic interactions and further confined within self-assembled nanostructured templates (out-of-plane, q_z) *i.e.* block copolymers. The

stabilization and wetting behavior of cellulose-reinforced thin film systems are addressed in Chapter IV through dewetting studies of thermoplastics and further examined on ultrahigh surface energy flexible substrates to transition past conventional, rigid substrates. Chapter V provides mechanical characterization on substrate-supported polymer nanocomposite films *via* buckling mechanics. Finally, Chapter VI gives an overall summary of the research work from the previous chapters and discusses potential areas for future work.

CHAPTER II

BACKGROUND AND LITERATURE REVIEW

2.1 Fundamentals of Dewetting and Wetting

The stability of a film is governed by the effective interface potential $\varphi(h)$ which is defined as the excess free energy per unit area required to bring the solid-liquid interface and liquid-air interface from infinity to a finite distance (h). The excess intermolecular interaction free energy ΔG accounts for the short-range and long-range interactions as a function of local distance or thickness (h) which is described by the relationship in Equation 1.1.

$$\Delta G = \frac{-A}{12\pi h^2} + S e^{-h/l} \quad (1.1)$$

Here, A is defined as the Hamaker constant, S is the spreading coefficient parameter, and l is the decay length. A negative Hamaker constant denotes long-range repulsion which promotes film stability, whereas a positive value implies a negative disjoining pressure with attractive interactions between the substrate-air interface that can lead to film rupture. If the second derivative of the excess free energy with respect to local thickness (h) is negative, the film is unstable. The spreading coefficient S is determined from the

relationship in Equation 1.2 where γ_A and γ_B is the surface tension of the liquid and substrate, respectively and γ_{AB} is the interfacial tension between the substrate and liquid:

$$S = \gamma_B - \gamma_A - \gamma_{AB} \quad (1.2)$$

There are three different proposed cases of the possible interactions between a liquid and solid substrate in terms of its stability and wetting nature, which is summarized in Figure 2.1.³² Two different equilibrium states are described in terms of thin film stability and wetting behavior for each case based off the initial states of a liquid with a solid where 1) a droplet of finite volume is initially placed on the solid substrate and 2) a film is forced to spread onto the substrate. In the first scenario, the liquid droplet can completely spread over the entire substrate leading to complete wetting. In Case 1, the interaction forces are repulsive and the spreading coefficient is positive such that $S > 0$. An absolute minimum is observed in the excess free energy curve as a function of finite thickness from the substrate in Case 2. In this case, pseudo partial wetting occurs above a critical thickness when a drop is placed on the substrate. When the thin film is forced to spread over the substrate in its initial state, morphological phase separation (MPS) is observed above the critical thickness. In Case 3, the liquid droplet is unable to completely spread due to attractive forces such that $S < 0$ and displays partial wetting. The film is unstable at all film thicknesses when forced to spread over the solid substrate which leads to dewetting.

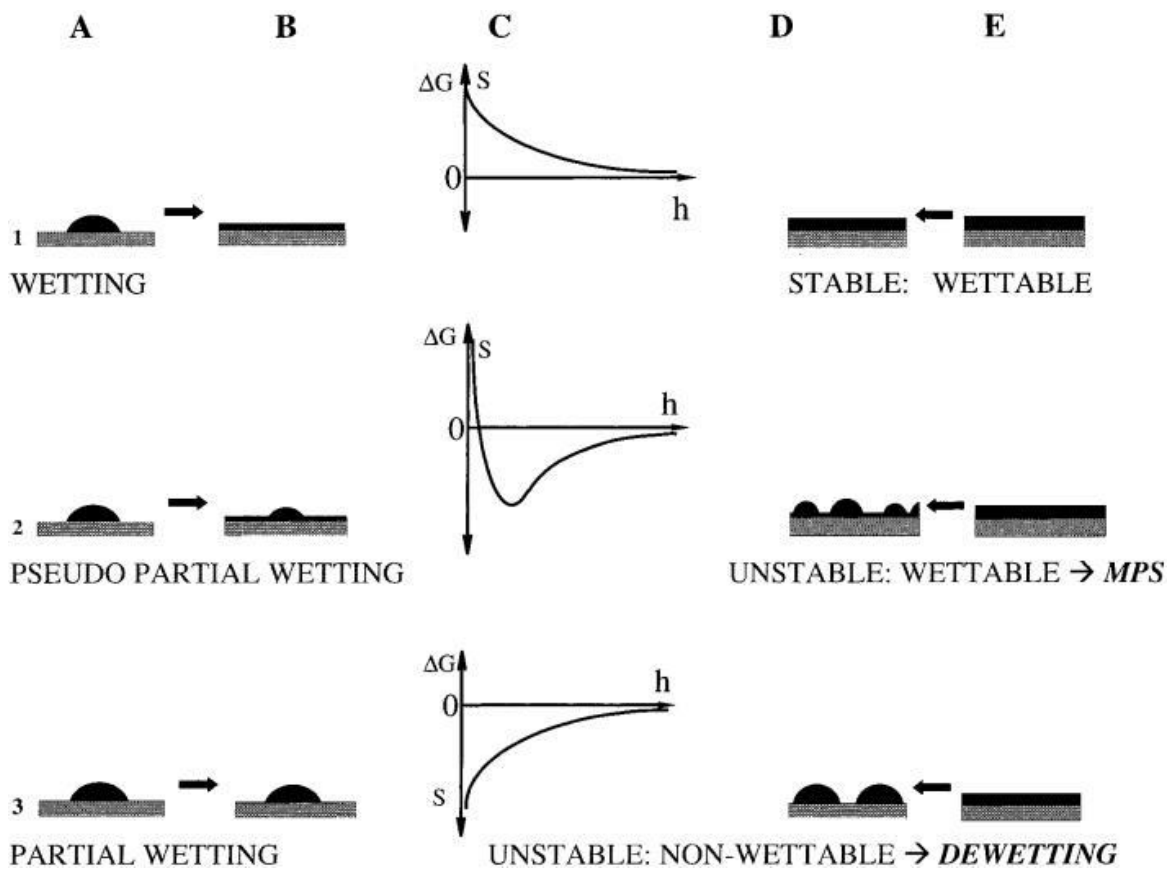


Figure 2.1 Schematic illustrating various different wetting and stability cases for a liquid on a substrate where A and E are the initial states, B and D denotes the equilibrium states, and C represents the excess free energy as a function of thickness, h . The initial state A represents a drop placed on the substrate while E describes a thin film that is forced to spread on the solid substrate in its initial state. Reprinted with permission from (32). Copyright (1999) American Chemical Society.

2.1.1 Dewetting Mechanisms

Polymer thin film dewetting can proceed *via* spinodal dewetting or nucleation and growth of holes. Spinodal dewetting occurs from amplification of capillary waves by thermal fluctuations on the surface.^{33–35} Hole nucleation, on the other hand, proceeds through heterogeneous or homogeneous (“thermal”) nucleation where nucleation can typically be initiated by dust particles, defects, or chemical inhomogeneities introduced on the surface.³⁶

There exist typical characteristic stages throughout the pattern formation process which is illustrated and summarized in Figure 2.2.³⁷ The initially smooth, uniform thin film can rupture when thermodynamically unstable, arising from amplification of surface undulations. The fastest growing wave vector is $q_M = \sqrt{3/2} (a/h^2)$ where $a^2 = |A|/6\pi\gamma$ and h represents film thickness. These perturbations of the film surface may propagate to the substrate, leading to the formation of holes. In the intermediate stage, excess material is removed and pushed towards the edges of the holes, subsequently forming a rim. Holes continue to grow in size until merging which leads to hole coalescence. The dynamics of the hole growth process is dependent on the polymer slippage or viscous flow, which influences the kinetics (hole growth velocity) and resulting patterned structures formed. The hole growth rate v is dependent on the wettability of the polymer on the underlying substrate such that $v \propto \theta^3$ where θ is the contact angle. In this regard, a substrate with a relatively high contact angle implies decreased wettability, resulting in characteristic fingering instabilities. Upon coalescence, this forms a continuous network structure of polymer ribbons which then spontaneously breaks up into droplets of size proportional to the ribbon diameter due to Rayleigh instability.³⁸

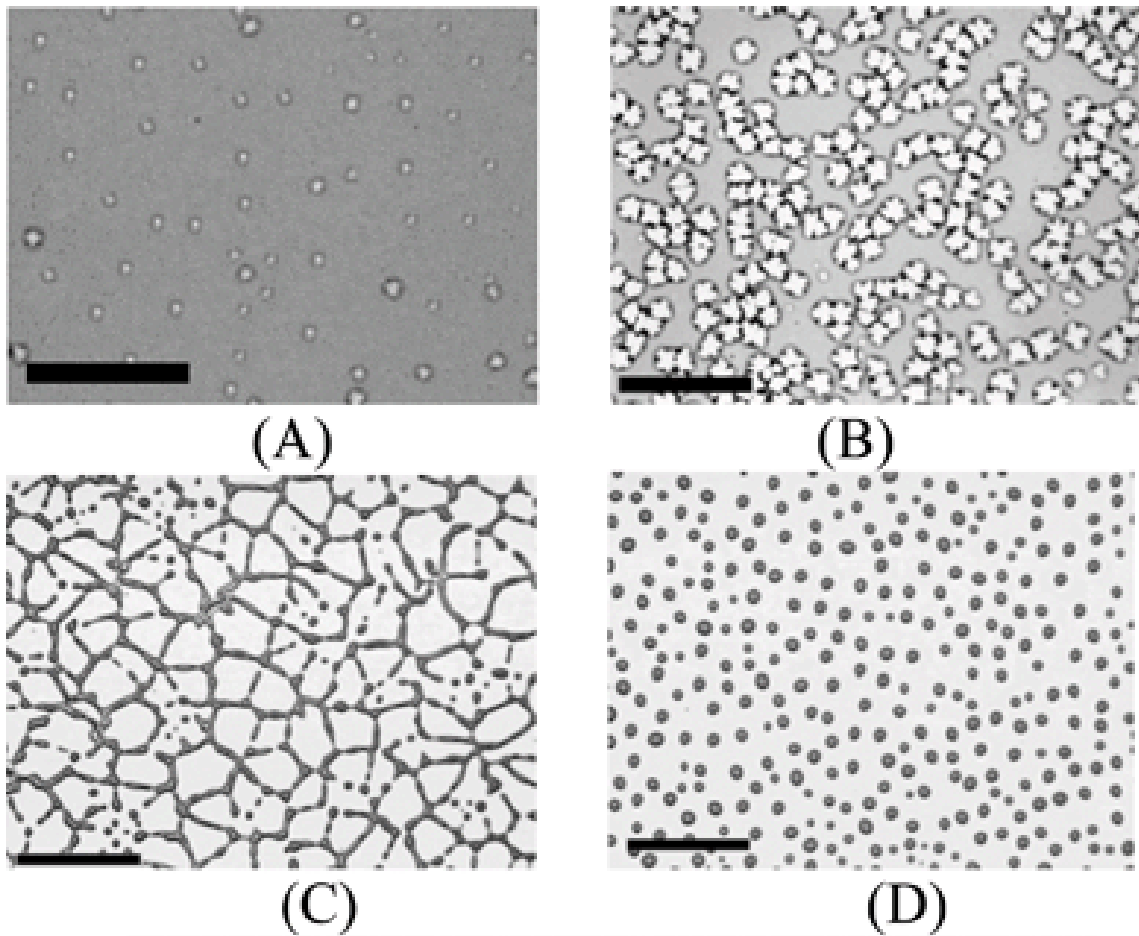


Figure 2.2 Optical micrographs displaying morphology evolution of PS ultrathin film on PDMS exposed to solvent vapor as a function of time. The representative images display different stages of dewetting including the a) initiation of holes, b) hole growth, and c) hole coalescence and ribbon formation to d) droplet formation. The scale bar is 50 μm for the micrographs in (a), (b), and (d), and 30 μm for (c). Reproduced from Ref. 37 with permission from The Royal Society of Chemistry.

More recently, the self-organization of polymer thin films has been exploited by controlling the dewetting pathways using chemically modified and topographically

patterned substrates.^{10,39-43} Template-directed dewetting provides a promising route to fabricate arrays of well-ordered structures over a large area with feature sizes on the micro- and nanoscale. Film morphology can be tailored to generate a myriad of complex structures through controlled pattern formation by manipulating parameters such as the film thickness, wettability, confinement, periodicity and geometry of patterns, and annealing conditions.

2.1.2 Strategies for Controlling Thin Film Stability

Various strategies have been explored to promote thin film stabilization and prevent dewetting. For instance, the use of polymers with a high molecular mass or chain entanglement can stabilize films over appreciable time scales, as well as aging of a polymer film below its glass transition temperature to allow relaxation of non-equilibrium polymer conformations after rapid solvent evaporation. Other approaches involve modifying interfacial interactions between the polymer film and substrate surface by grafting polymer chains onto the surface to alter the wettability,^{44,45} sulfonation and metal complexation of the polymer,⁴⁶ addition of block copolymers,^{47,48} or altering the roughness or surface chemistry *via* irradiation.⁴⁹ The introduction of functionalized end groups with a high affinity for the substrate was also demonstrated as an effective means to retard or inhibit dewetting, as shown in Figure 2.3.⁵⁰

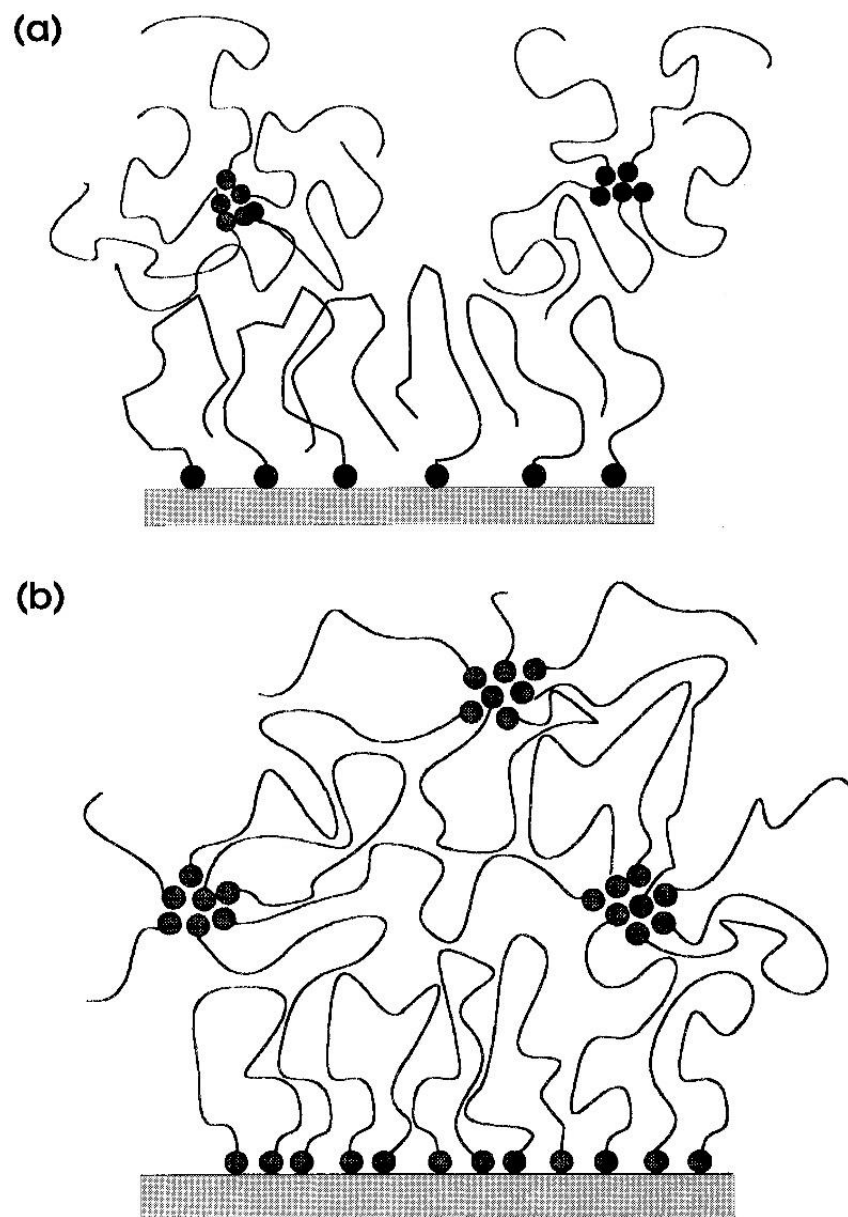


Figure 2.3. Schematic of thin films with a) monofunctional PS chains and b) difunctional PS chains where the black circles denote ionic end groups. Reprinted with permission from (50). Copyright (1996) American Chemical Society.

However, these approaches typically involve chemical modification of the polymer or substrate which requires specific tailoring of the system. To avoid chemical modification, alternative universal approaches have been exploited to stabilize films or delay dewetting kinetics, for instance, through incorporation of nanoparticles in polymer thin films. This will be discussed in further detail in Chapter IV.

2.2 Polymer Nanocomposites

Polymer nanocomposites have recently attracted great technological interest over the years in the development of multi-component advanced materials.⁵¹⁻⁵⁴ Polymer nanocomposites consist of engineered multiphase materials that are comprised of a host polymer matrix (continuous phase) and nanoparticles (dispersed phase) having at least one dimension less than 100 nm, as shown in Figure 2.4. The incorporation of nanoparticles in a polymer matrix offers tremendous potential to tailor material properties, which can lead to significant enhancement in the optical, thermal, mechanical, and/or electrical performance that otherwise cannot be attained in conventional polymer materials or either phase alone.⁵⁴⁻⁵⁷

The commercialization of polymer nanocomposites was first demonstrated by Toyota in 1991 by introducing nylon-6/clay nanocomposites in collaboration with Ube for application in the timing belt covers of Toyota automotive vehicles. The incorporation of 5 wt% organophilic clay displayed considerable enhancement in the composite material properties in comparison to the pure polyamide, resulting in a significant increase in the heat distortion temperature and mechanical reinforcement.⁵⁸⁻⁶⁰ This was shortly followed by production of engine covers through injection molding that was comprised of nylon-6

nanocomposites on Mitsubishi GDI engines by Unitika Co. and offered a 20% weight reduction. Other examples include a step-assist automotive component consisting of polyolefin/clay nanocomposites for General Motors' GMC Safari and Chevrolet Astro vans and then extended for application in the doors of Chevrolet Impalas. In addition to automotive applications, the use of polymer nanocomposites has recently attracted considerable interest in aerospace applications, microelectronics, and improved barrier resistance through multilayer films and bottles in food packaging.^{16,17}

The development of unique macroscopic properties can be attributed to the synergistic effect between the polymer chains and filler, especially for nanoparticles with feature sizes approaching the length scale of a single polymer coil. The nanoscale dimensions of incorporated particles offer a distinct advantage over conventional micron-sized fillers where the ability to induce intrinsic property change with relatively low filler content (typically less than 5%) can be ascribed to the characteristic high surface area to volume ratio, in comparison to conventional additives.

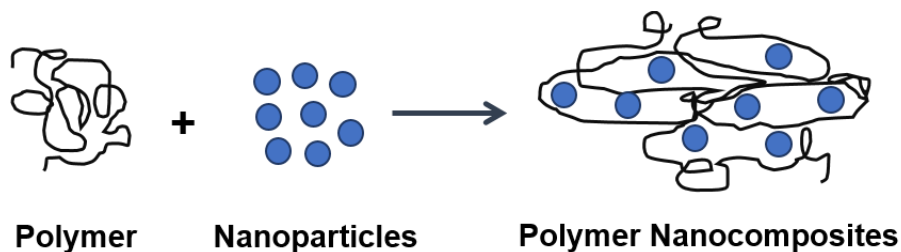
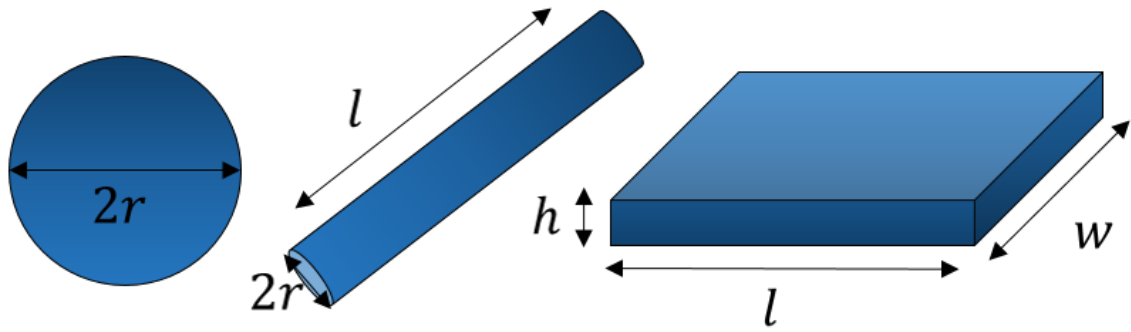


Figure 2.4 Schematic of polymer nanocomposites consisting of a polymer matrix and nanoparticles, in which one of the constituent phases has at least one dimension on the order of nanometers.

The nanoparticle surface chemistry, size, and shape are variables that have been demonstrated to influence the overall property changes on the molecular scale. Figure 2.5 represents examples of typical particle geometries including spheres, rods, and platelet structures with their respective surface area to volume ratios. The available surface area to volume ratio is indicative of the interfacial area compared to bulk and these interfacial interactions vary according to the filler dimensions as shown in Figure 2.5. Depending on the matrix-filler interactions, the interfacial region can influence novel material properties that significantly deviate from the bulk material.

For a spherical particle, the magnitude of the surface to volume ratio has an inversely proportional relationship to the particle radius where $S/V = (4\pi r^2)/(4/3\pi r^3) = 3/r$. At a fixed volume fraction, the surface area per volume increases as the radius of the spherical particle decreases in size, which implies an increased quantity of available interactions between the polymer chains and fillers. For cylindrical fillers with a particle radius (r) and length (l), the surface area to volume ratio is given as $S/V = 2/r + 2/l$. However, as the nanoparticle aspect ratio increases, *i.e.* cylindrical and platelet geometries, it becomes increasingly more difficult to attain well-dispersed states of nanoparticles which is mainly attributed to particle packing and excluded volume effect where two rigid particles can not occupy the same area of space at a given time. The aspect ratio (AR) is defined as the particle length to width ratio, or $AR = L/w$.



Surface area-to-volume ratio of fillers:

$$\frac{S}{V} = \frac{3}{r}$$

$$\frac{S}{V} = \frac{2}{r} + \frac{2}{l}$$

$$\frac{S}{V} = \frac{2}{h} + \frac{2}{l} + \frac{2}{w}$$

Figure 2.5. Examples of different nanoparticle geometries (spheres, rods, plates) with its respective surface area (S) to volume (V) ratio where r is the radius, l is the length, h is the height, and w is the width.

2.2.1 Surface Chemistry Modification

To maximize the interfacial area and optimize macroscopic property enhancement, the challenge lies in controlling the dispersion of nanoparticles within the polymer matrix. The controlled nanofiller dispersion is governed by thermodynamic mechanisms through the interplay of entropic and enthalpic interactions. For instance, consider the athermal case of a chemically similar polymer matrix and brush system. Despite the absence of enthalpic penalties, entropically-driven depletion forces existing between nanofillers can induce the clustering and agglomeration of nanoparticles. To mitigate the attractive particle-particle interactions and increase favorable interactions between the nanoparticles and polymer

matrix, ligands can be attached to the nanoparticle surface by using small molecules or polymer brushes.

One method to control the spatial dispersion is to increase the interactions between the nanoparticles and polymer chains by surface chemistry modification of nanoparticles. Attachment of a polymer brush to nanoparticles can be achieved using a “grafting-from” technique where the grafting reaction can proceed by polymerization from the surface or a “grafting-to” process where end-functionalized polymer chains are pre-formed prior to attachment to the nanoparticle surface. While “grafting-to” offers a fairly straightforward route to attach pre-formed chains, the steric hindrance effects between already attached polymer chains and chains approaching the surface presents current limitations to achieve a high grafting density. In the “grafting-from” approach, the surface is functionalized in the presence of an initiator and the chain is grown from the nanoparticle surface using methods such as atom transfer radical polymerization (ATRP), reversible-addition fragmentation chain transfer (RAFT), or nitroxide-mediated polymerization (NMP). ATRP is a robust technique for surface-initiated polymerization with controlled molecular weight and low polydispersity.⁶¹ The polymerization is controlled through the equilibrium of dormant and radical species which essentially involves a reversible homolytic transfer between a dormant chain end and a transition metal complex, inducing chain propagation of the radical. Figure 2.6 shows an example of a controlled radical polymerization to synthesize bimodal polymer brush on nanoparticles in which the step-by-step RAFT polymerization is demonstrated.⁶²

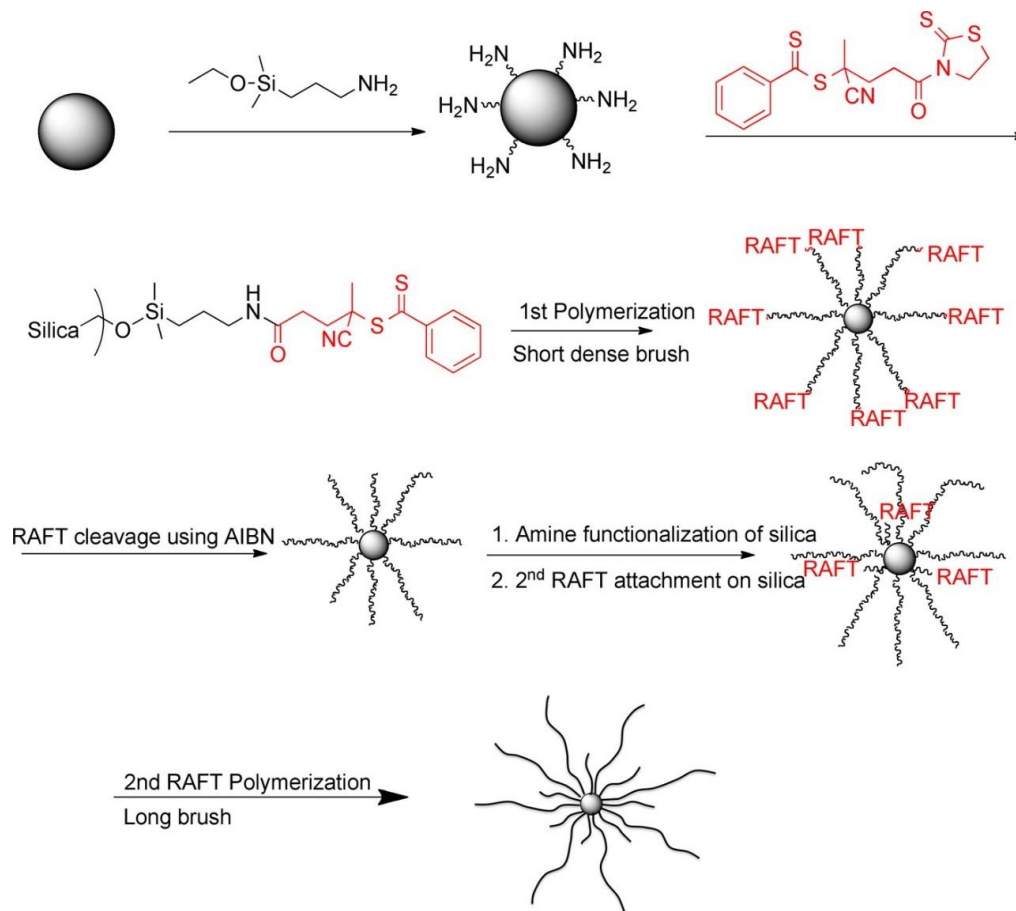


Figure 2.6. RAFT polymerization to synthesize bimodal polymer brush on nanoparticles.

Reprinted with permission from (62). Copyright (2012) American Chemical Society.

Factors such as the grafting density σ and the degree of polymerization of the grafted polymer chain (N) relative to the free polymer matrix chain (P) influence the regimes known as the ‘wet brush’ or ‘dry brush’ regime. The relative interactive strength and degree of interpenetration between the free polymer chains from the matrix and the grafted chain directs the localized organization of nanoparticles. In a chemically identical polymer matrix and brush system, the total free energy of the system is mainly governed by 1) the mixing entropy of the free chains and grafted chains and 2) the elastic deformation of the grafted chains which could result from chain stretching or compression. For nanoparticles

with low grafting density, increasing attractive particle-particle interactions and insufficient surface coverage can induce particle aggregation and/or give rise to new morphological structures. Recent work have demonstrated that for $P < N$, the shorter chain lengths of the polymer matrix can penetrate into the grafted corona, which results in swelling or namely, a wet brush. In the case of $P > N$, the elastic deformation term dominates and the free chains are expelled from the brush. This leads to a dry brush where the grafted chains are in a compressed state.

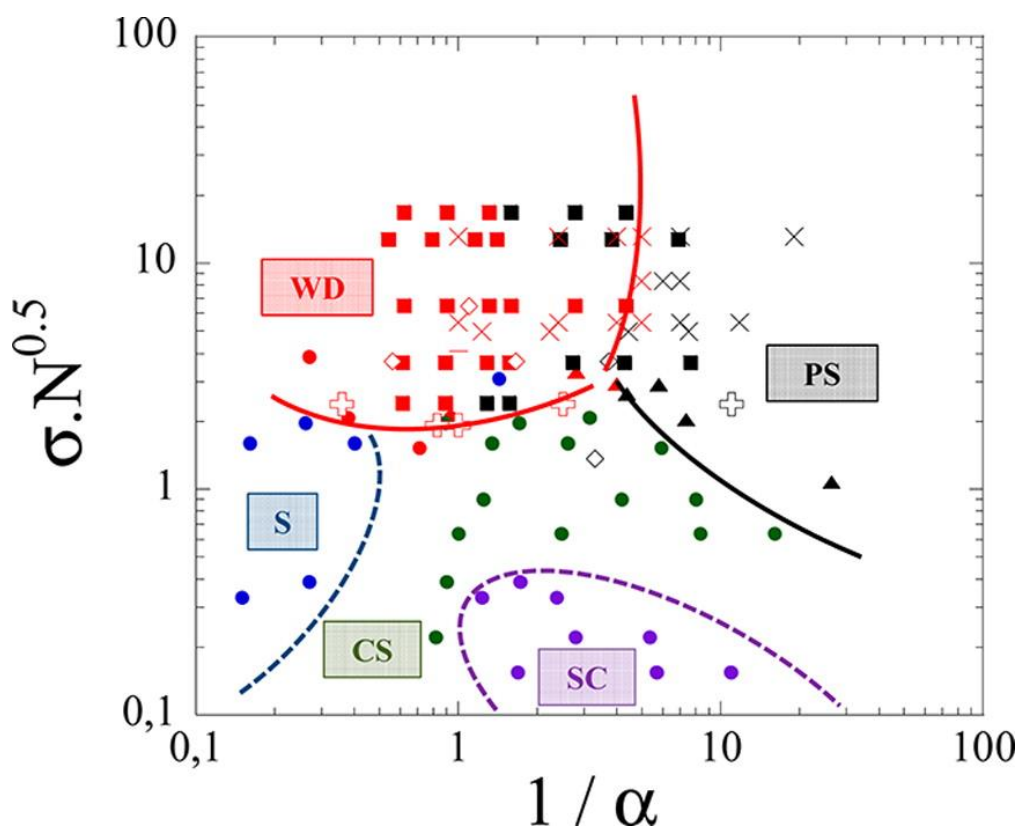


Figure 2.7. Phase diagram of nanoparticle morphologies compiled from literature with regions displaying well-dispersed (WD) states denoted by red, strings (S) by blue circles, connected sheets (CS) by green, small clusters (SC) represented by purple, and phase separated (PS) particles shown in black. Reprinted with permission from (63). Copyright (2013) American Chemical Society.

The nanocomposite morphology diagram in Figure 2.7 summarizes the data trends compiled from literature.⁶³ The nanoparticles used for these studies are reported to be similar in size with diameters ranging from 7 to 27 nm and NP concentrations typically around 5 vol%. The phase diagram is comprised of well-defined regions that are plotted as a function of $\sigma\sqrt{N}$ and $1/\alpha$ where $\alpha = P/N$ to account for the degree of crowding by the brush. At relatively high grafting densities such that $\sigma\sqrt{N} > 2$, composite systems are likely to exhibit well-dispersed (WD) states or phase-separated (PS) morphologies. This regime corresponds to steric stabilization where a high grafting density ensures screening of interparticle attractive forces. However, lower grafting densities can result in different morphologies such as stringlike (S), connected sheets (CS), or small clusters (SC) due to brush physics and core-core attractions.

2.2.2 Anisotropic Nanofillers for Mechanical Reinforcement

Nanofillers of cylindrical and plate geometries, in particular, have been exploited as effective reinforcing agents in polymer systems where the composite material response or potential enhancement of macroscopic properties can be anisotropic in nature. For effective reinforcement of a polymer matrix, there are several factors of the nanofiller to be considered such as the aspect ratio, nanoparticle alignment, dispersion, and interfacial stress transfer. The aspect ratio of a nanoparticle is defined as the length-to-diameter ratio. Increasing the NP aspect ratio results in the increased stress transfer to the nanoparticles. Figure 2.8 displays the effect of aspect ratio on the CNT reinforcement through molecular dynamics (MD) simulations and three-phase micromechanical model by accounting for the

matrix, reinforcement phase, and interfacial region. In this study, Arash *et al.*⁶⁴ examined the fracture behavior of CNT/PMMA composites under tension. The incorporation of CNTs of infinite length was observed to significantly increase the modulus approximately 16 times that of pure PMMA from 2.86 GPa to 46.73 GPa. Strong interfacial bonding between the matrix and filler is critical in maximizing effective reinforcement by distribution of the applied external stress load of the nanocomposite film to the nanorods. In addition to these parameters, individual well-dispersed nanoparticles result in a uniform stress distribution for efficient load transfer to the nanofiller, whereas agglomeration of particles can potentially yield localized stress-concentrated areas. The alignment of nanorods have also been demonstrated to contribute to a higher composite strength and stiffness.

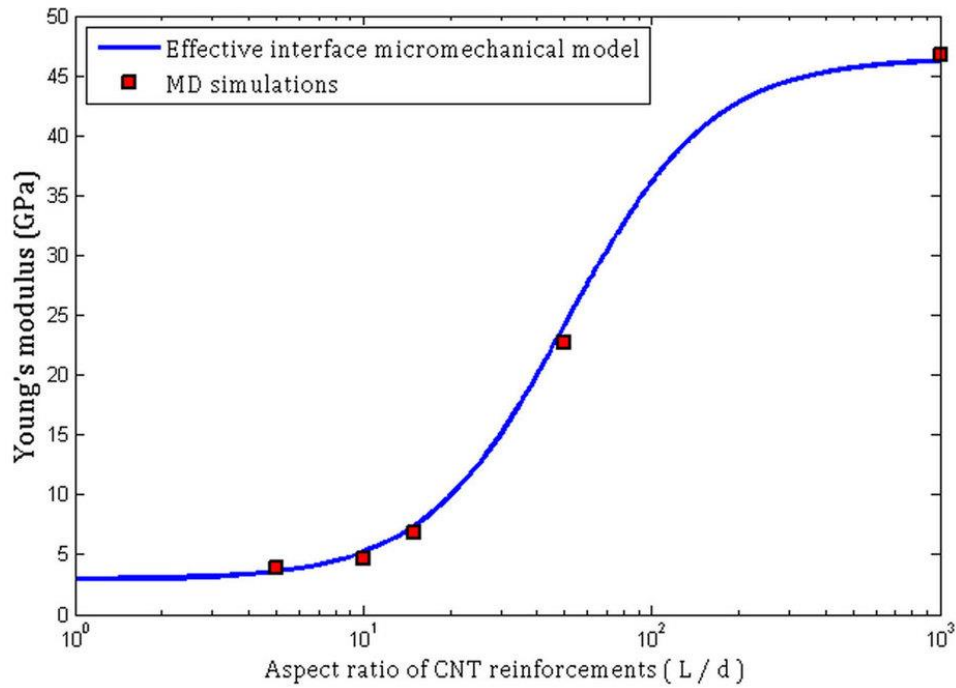


Figure 2.8. Young's modulus of carbon nanotube/poly(methyl methacrylate) composite material as a function of CNT aspect ratio (L/d) from MD simulations and micromechanical model. Reprinted with permission from [64].

Micromechanical models have been proposed to predict the elastic properties of composite materials. The mechanical behavior of multiphase systems is dependent on several variables including the mechanical properties of each constituent, interfacial region properties, volume fractions, as well as the spatial arrangement or orientation of fillers in the matrix. One of the simplest mechanical models is based on the rule of mixtures of a system comprised of two components in parallel or series which is expressed as:

$$E_C = fE_f + (1 - f)E_m$$

where E_C , E_f , and E_m are the moduli of the composite material, filler, and matrix, respectively, and f corresponds to the volume fraction of the filler. The rule of mixtures represents the upper bound of the modulus of the composite whereas the inverse rule of mixtures denotes the lower bound, as represented in the equation below:

$$1/E_C = f/E_f + (1 - f)/E_m$$

However, the rule of mixtures is a simplified theory that solely accounts for the volume fraction of the components and assumes perfect bonding between the filler and matrix. In this regard, Halpin-Tsai model serves as a common approach to determine the Young's modulus. The modulus of the composite in the longitudinal (L) and transverse (T) directions can be expressed in the following semi-empirical Halpin-Tsai equations⁶⁶:

$$E_L = \frac{1 + 2(l/d)\phi\eta_L}{1 - \phi\eta_L} E_m$$

$$E_T = \frac{1 + 2\phi\eta_T}{1 - \phi\eta_T} E_m$$

where l and d represents the length and diameter of the filler, respectively.

$$\eta_L = \frac{E_f - E_m}{E_f + 2(l/d)E_m}$$

$$\eta_T = \frac{E_f - E_m}{E_f + 2E_m}$$

There are several assumptions associated with the Halpin-Tsai model including that the matrix and fillers are linearly elastic, the fillers are perfectly aligned, and the fillers are uniform in size/shape and homogenous. While the Halpin-Tsai model proves to be fairly accurate at low filler volume fraction, it deviates at higher particle concentrations which is attributed to interparticle interactions that are not taken into consideration.

Qian et al. studied the load transfer and deformation mechanism through tensile tests and *in situ* transmission electron microscopy (TEM) measurements with multiwall carbon nanotubes (MWCNTs) dispersed in a polystyrene (PS) matrix.⁶⁵ The addition of 1 wt% MWCNT in PS resulted in an increased elastic modulus by approximately 35% and 42% for MWCNTs with an aspect ratio of 446 ($l \sim 15 \mu m, d \sim 30 nm$) and 1167 ($l \sim 50 \mu m, d \sim 30 nm$), respectively. The fracture mechanism was examined by condensing the electron beam onto the polymer composite thin film which induced localized thermal stresses and subsequent crack initiation. The cracks were observed to nucleate at regions that contained a low density of nanotubes and propagate along these regions or at weak particle-polymer interfaces. Initially, the nanotubes were observed to align in a direction perpendicular to the crack in attempt to bridge the crack, however, after reaching a critical crack displacement, the MWCNTs are observed to break and/or pull out of the matrix.

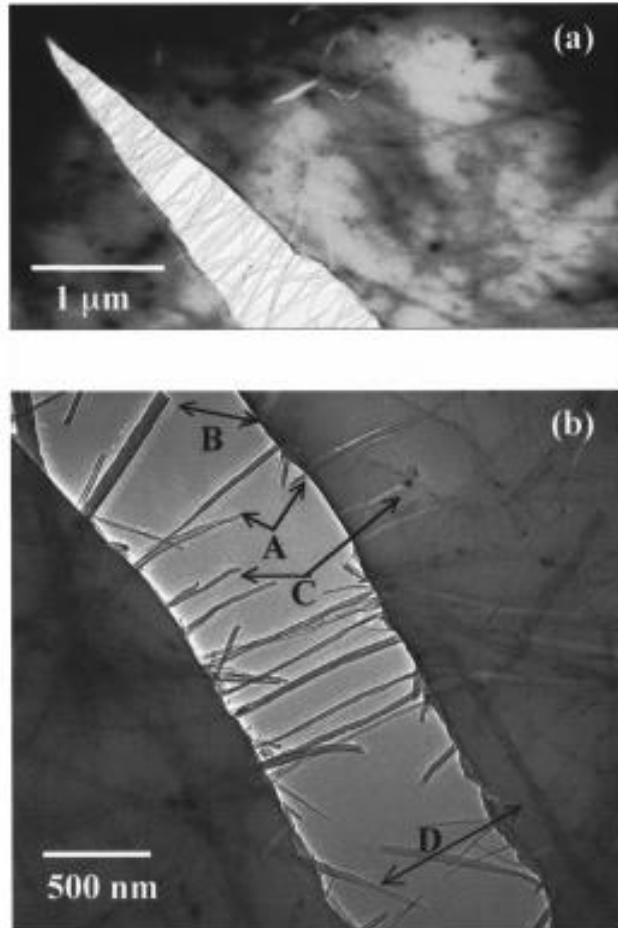


Figure 2.9. TEM micrographs of MWCNT-PS thin film with crack initiation and propagation induced by local thermal stresses. Reprinted with permission from [65].

The rupture mechanism was further illustrated by Ye et al.⁶⁷ with carbon nanotube-polymer composite fibers under tension. The presence of defects or impurities can initiate crazing and ultimately lead to rupture from these weak points, due to the presence of a large stress concentration. Single-walled carbon nanotube (SWCNT)-PAN composite fibers produced *via* electrospinning were observed to undergo a toughening mechanism shown in Figure 2.10 where homogeneously dispersed SWCNTs align along a craze to hinder crazing extension and significantly reduce stress concentration. In Figure 2.10d, the

crazing fibrils break and the CNTs undergo a pull-out mechanism to reinforce the fibers by energy dissipation. The extent of reinforcement is determined by the interfacial adhesion and homogeneous distribution of nanotubes which can uniformly transfer the stress to the CNTs. Further rupture of the fiber can not be prevented in some cases, dependent on the size of the individual nanorods. Similarly, this mechanism was also demonstrated for cellulose nanocrystals and cellulose microfibrils in poly(ethylene oxide), differentiating the effect of aspect ratio on its reinforcing properties.²⁷

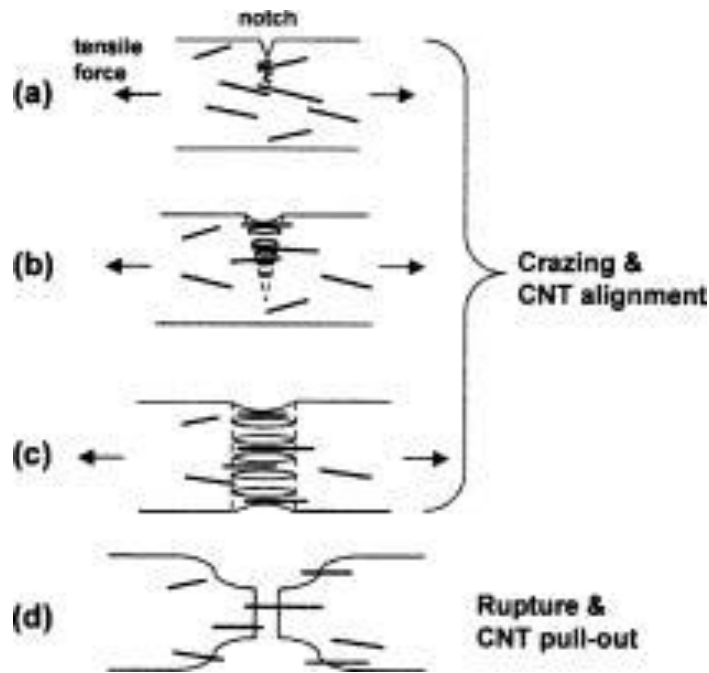


Figure 2.10 Schematic illustrating the rupture behavior of a PAN-CNT fiber in which the mechanism involves a) the formation of voids under tension, b) crazing fibrils form as the void extends and CNTs align parallel to the fibril direction, c) crazing extension with well-aligned CNTs along the crazing, and d) composite fiber rupture and CNT pull-out. Reprinted with permission from [67].

2.3 Cellulose Nanocrystals (CNCs)

The development of nanomaterials from renewable sources has become increasingly popular over the last decade to find greener alternatives to create high performance materials that are non-toxic, recyclable, environmental-friendly, and lightweight. Cellulose nanocrystals (CNCs) are the main reinforcing unit derived from sources such as trees, plants, algae, and bacteria where the hierarchical structure designed by nature gives rise to the impressive mechanical strength of CNCs. Cellulose can be extracted from the cell walls where lignin and hemicellulose are removed *via* mechanical methods to attain cellulose microfibrils which consist of amorphous and crystalline regions. Cellulose nanocrystals are acquired by further breaking down the microfibril and removing the amorphous regions within these fibrils through hydrolysis techniques to produce highly crystalline rod-like nanoparticles. Hydrolysis involves a diffusion-controlled mechanism into the fibers and subsequent cleavage of glycosidic bonds using acids such as hydrochloric acid, sulfuric acid, phosphoric acid, and nitric acids. Sulfuric acid serves as an effective hydrolyzing agent by distribution of sulfate ester groups ($-\text{OSO}_3^-$) on the cellulose surface. The presence of negatively charged sulfate ester groups promotes CNC dispersion in an aqueous, stable suspension due to the electrostatic repulsion between individual nanorods. The dimensions of individual CNCs, nanoparticle aspect ratio, crystallinity, and surface chemistry are influenced by the species that the cellulose was extracted from, along with the processing conditions and extraction methods. These parameters result in a large degree of variation in the characteristics of cellulose nanocrystals that are reported.

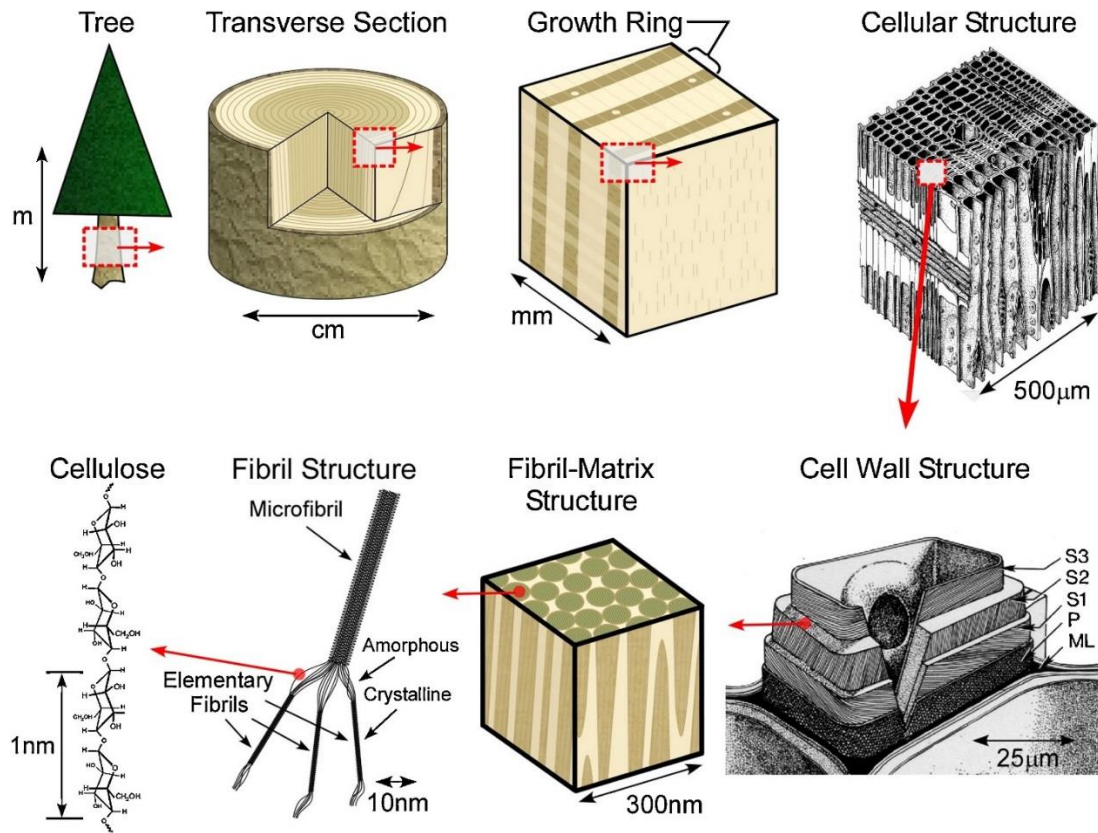


Figure 2.11. Schematic illustrating the hierarchical design of a tree to produce cellulose nanocrystals. Reprinted with permission from [103].

Cellulose is comprised of repeating anhydroglucose units ($C_6H_{10}O_5$)_n connected by a β -(1,4) glucosidic covalent bond, as shown in Figure 2.12. The intrachain hydrogen bonding between hydroxyl groups and oxygens of the adjoining ring molecules stabilizes the linkage and results in the linear configuration of the cellulose chain. Due to its anisotropic nature and appealing mechanical properties, CNCs can be used in a number of versatile applications, including packaging, membranes, drug delivery, hydrogels for its water retention/absorption properties, and lightweight body armor. This high-performance nature can be attributed to its unique properties of having a low density of 1.6 g/cm^3 , a high strength and stiffness comparable to Kevlar, and low thermal expansion coefficient. As

such, this sustainable nanomaterial compares quite well in terms of specific strength and modulus with other well-known reinforcing materials when accounting for the material's density. CNCs surpass Kevlar in this regard, and ideally, could possibly serve as a cheaper, renewable alternative. However, the main challenges in utilizing CNCs as effective reinforcing agents include current limitations in controlling the dispersion of nanorods and the stability of the system due to particle aggregation. This can be ascribed to strong intramolecular and intermolecular hydrogen bonding interactions.

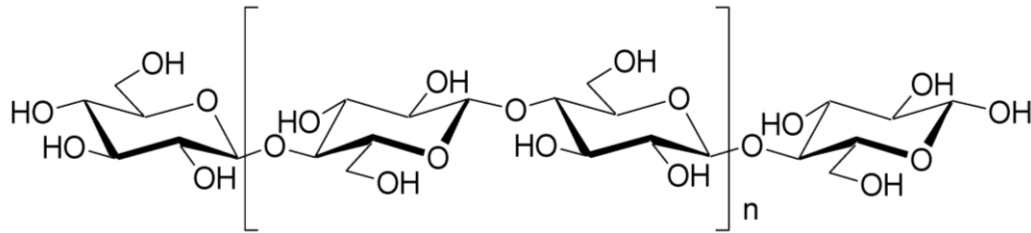


Figure 2.12. Chemical structure of cellulose.

To determine the reinforcing effect of cellulose nanocrystals in multiphase materials, mechanical modeling of CNC-based composites is sought by accounting for each of the three phases that comprise a typical composite: the matrix, the fillers, and percolating network. The percolation threshold is the critical volume fraction that separates the dispersed (disconnected) components from a state of infinitely connected network.⁶⁸ There are several variables such as the particle dimensions and shape, particle-particle interactions, and the orientation that influence the critical volume fraction. The formation of a continuous filler network above a given percolation threshold leads to the unique mechanical behavior of cellulose reinforced nanocomposites due to the presence of strong hydrogen bonding interactions. In this regard, the adaptation and extension of the series-

parallel model of Takayanagi *et al.*⁶⁹ has been used to account for the strong interparticle interactions and its mechanical percolation effect.

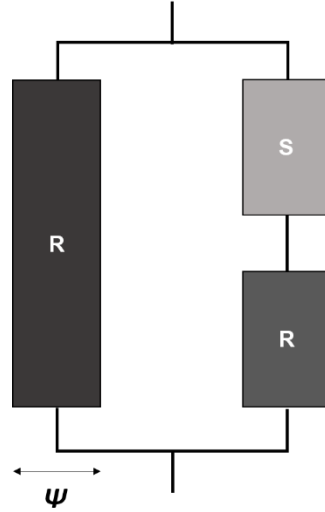


Figure 2.13. Schematic illustrating the model consisting of a rigid phase (R) and soft phase (S). The rigid phase accounts for the percolating filler network (black) in addition to the dispersed fillers (grey).

A schematic representation of the series-parallel model is displayed in Figure 2.13, which is comprised of a soft phase (S) corresponding to the polymer matrix and rigid phase (R) denoted by the cellulose nanocrystals. Ouali *et al.*⁷⁰ modified the model to account for the arrangement of particles and interparticle interactions where the composite elastic tensile modulus was given by the relationship below:

$$G_C = \frac{(1 - 2\Psi + \Psi\phi_R)G_S G_R + (1 - \phi_R)\Psi G_R^2}{(1 - \phi_R)G_R + (\phi_R - \Psi)G_S}$$

In this relationship, the G_C , G_S , and G_R correspond to the moduli of the composite, soft phase, and rigid phase, respectively, ϕ_R is the volume fraction of the rigid phase, and Ψ denotes the volume fraction of the percolating phase. The Ψ is an adjustable parameter where b is the critical percolation exponent that can be expressed as $b = 0.4$ for a three-dimensional network system.⁶⁸ The percolation threshold ϕ_c for rod-like particles can be determined by the relation which accounts for the aspect ratio of the cylindrically shaped particle such that $\phi_c = 0.7/(L/d)$.^{31,71}

$$\Psi = 0 \quad \text{for } \phi_R < \phi_c$$

$$\Psi = \phi_R \left(\frac{\phi_R - \phi_c}{1 - \phi_c} \right)^b \quad \text{for } \phi_R > \phi_c$$

2.4 Strategies for Controlling Spatial Distribution

Polymeric materials under confinement exhibit unique property responses that have been observed to significantly deviate from bulk material responses, among which includes variation in the mechanical properties,^{72–76} diffusion coefficients,^{77,78} physical aging,^{79–81} and polymer glass transition temperature T_g .^{15,82–89} Samples in the thin film geometry can manipulate the physical or thermal behavior of a material system, for instance, by reduction of the film thickness to a similar length scale of the polymer chains. This deviation from the bulk properties is attributed to the constraint of the polymer chains and segmental mobility influenced by confinement and interfacial interactions.^{13,14,90} There are several techniques currently utilized to exploit thin film confinement through fabrication of

controlled multilayer structures at the micro- and nanoscale such as co-extrusion processes, layer-by-layer (LBL) assembly, and directed self-assembly of block copolymers which additionally can be employed as methods for controlling the organization of nanoparticles.

2.4.1 Multi-layer Coextrusion

Coextrusion is an efficient processing method in which two or more polymers are extruded to produce a sheet or film comprised of multilayer structures. Figure 2.14 represents an example of the microlayer coextrusion assembly with AFM micrographs displaying cross-sections of multilayered PC-coPVDF films.⁹⁴ This technique allows for the tunability of desired functionalities and enhancement of property characteristics that otherwise cannot be attained from a single polymeric material. In a typical coextrusion process, multiple polymers are extruded from different streams which then pass through a series of multiplier dies to accordingly obtain a specific number of layers and overall total film thickness. The ability to tailor material performance such as gas permeability or mechanical toughness for commercial applications in flexible packaging can be realized by varying the thickness of individual layers and interphase through a continuous processing technique.⁹¹⁻⁹³

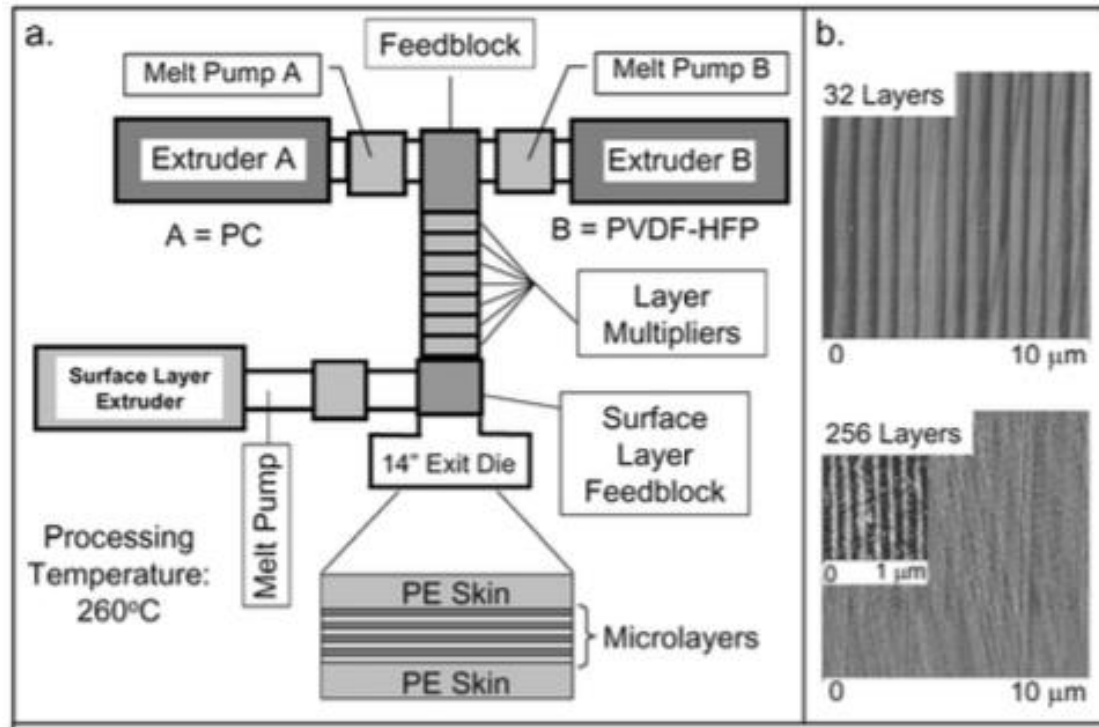


Figure 2.14 a) Schematic of the microlayer coextrusion assembly. AFM images of the cross-sections of multilayered PC-coPVDF films with b) 32 layers and c) 256 layers. Reproduced with permission from [94].

However for optimal performance, it becomes critical to maintain layers of uniform thickness for the tens to thousands of alternating layers. Current limitations include layer non-uniformities or thickness variations, interface distortions, and flow instabilities that arise during the manufacturing process, which can be caused by differences in the polymer viscosities, surface tensions, and elasticity.^{95–98} To this end, many studies have focused on the optimization of processing conditions and polymer rheology to minimize distortions in the layered materials for technological applications in gas barriers, capacitors, or food packaging.

2.4.2 Microphase Separation in Block Copolymers

Block copolymers (BCPs) are comprised of two or more chemically distinct, immiscible polymers linked by covalent chemical bonds. Due to the incompatibility of these blocks, segregation tends to occur below the order-to-disorder transition temperature T_{ODT} , however the spatial extent is limited to the level of molecular dimensions owing to the chemical bond, which leads to microphase separation. As a result, block copolymers self-assemble and microphase separate into well-defined periodic nanostructures on a characteristic length scale ranging from 5 to 100 nm. There are various architectures that exist such as linear block copolymers and branched copolymers including graft, star, dendritic, and cyclic copolymers. The simplest form of a BCP is a linear diblock copolymer comprised of two distinct blocks, A and B.

The phase behavior is influenced by three main factors: the volume fraction of blocks f , Flory-Huggins interaction parameter χ , and the degree of polymerization N . Microphase separation is governed by an interplay between enthalpy of demixing and entropic driving forces. The Flory-Huggins interaction parameter has an inversely proportional relationship to the temperature as shown in the equation below:

$$\chi = \frac{\alpha}{T} + \beta$$

where α and β are constants that are system-dependent and T is the temperature. A higher χ value denotes a higher phase incompatibility of the blocks and the product of χN denotes segregation strength. Depending on the product of χN and volume fraction of the block components f , block copolymer chains can undergo directed self-assembly to form a wide

array of different morphologies such as spheres (S), cylinders (C), gyroid (G), and lamellae (L) as shown in Figure 2.15. For symmetric diblock copolymer systems where $f_A = f_B = 0.5$, lamellar microdomains are formed when $\chi N \geq 10.5$.

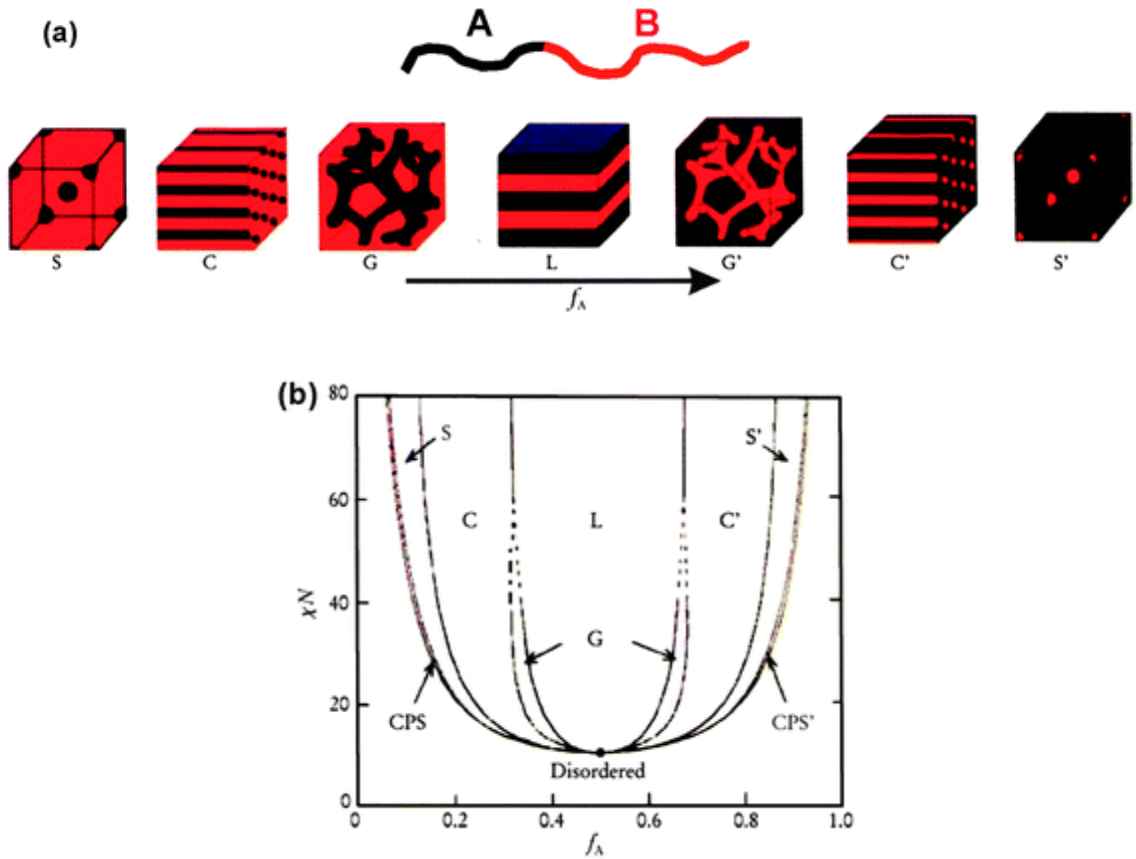


Figure 2.15. (a) Equilibrium morphologies of microphase-separated A-B diblock copolymers as a function of increasing volume fraction f of block A and (b) phase diagram of A-B diblock copolymer predicted by self-consistent theory. Reproduced from Ref. 88 with permission from The Royal Society of Chemistry.

In addition to variables such as the volume fraction of the blocks and segregation strength, BCP thin films are subjected to a degree of confinement which influences the

morphologies. The surface energies and interfacial tension, in particular, govern the subsequent morphology and orientation of the block copolymer thin films by minimizing energetic penalties associated with chain stretching or compression.

Consider a linear symmetric AB diblock copolymer where one block (either A or B) has an affinity to both the substrate and free surface, which results in *symmetric wetting*. In this case, the total film thickness h follows the relationship, $h = nL_0$ where n represents an integer such as $n = 1, 2, 3, 4$. If block A preferentially wets the substrate surface and block B segregates to the film-air interface, the microphase separated BCP exhibits *asymmetric wetting* where $h = (n + 1/2)L_0$.

On the other hand, if neither block A or B exhibit preferential interactions with the given boundary conditions, this results in a neutral wetting case. The surface topography can be determined from the total film thickness relative to the domain spacing L_0 where the formation of islands or holes on the film surface is due to incommensurate film thickness. If the commensurability condition is attained or deviation is small such that polymer chains can stretch or compress accordingly, then islands and holes will not be observed at the free surface. Figure 2.16 summarizes the different wetting scenarios and morphologies of lamellar block copolymer thin films of varying preferential interactions with the boundary conditions.⁹⁹

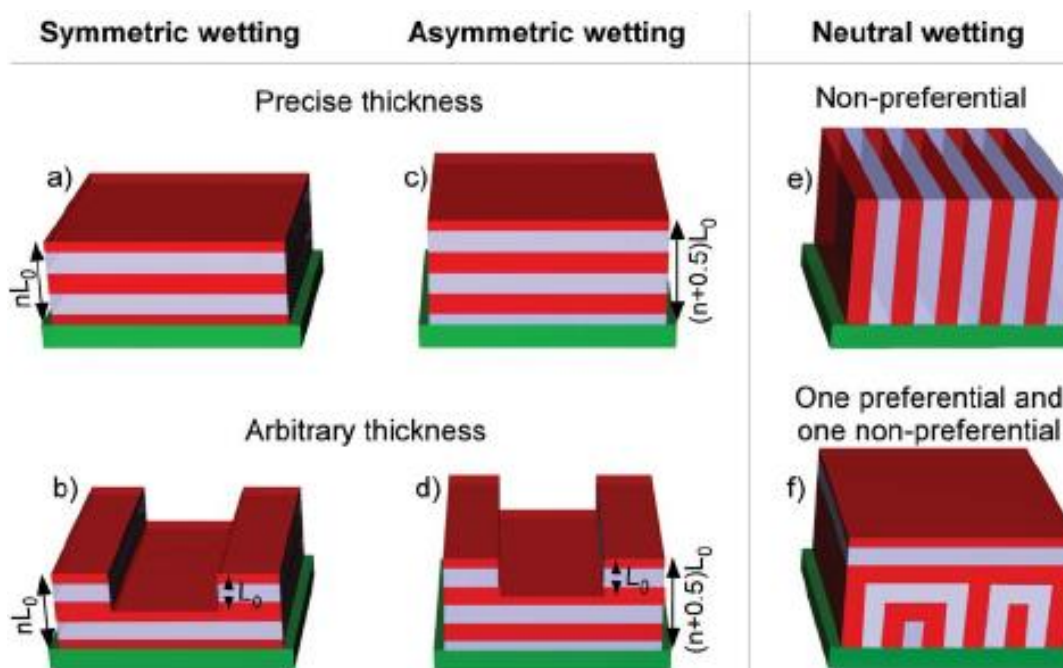


Figure 2.16 Symmetric wetting, asymmetric wetting, and neutral wetting scenarios of BCP thin films due to preferential surface energetics and relative film thickness. Reproduced from Ref. 99 with permission from The Royal Society of Chemistry.

Block copolymers (BCPs) can act as ideal nanostructured templates for fillers due to its ability to self-assemble into periodic microdomain structures ranging from 5 to 100 nm. The organization of nanoparticles in ordered block copolymers allows for facile control over hybrid assemblies, the morphological structure, and processability of polymer nanocomposites. The distribution of nanoparticles and spatial orientation in a selective domain is governed by factors such as thermodynamic interactions and NP geometry (size and shape) relative to polymer chains (matrix). The localization of nanoparticles in block copolymers is summarized in Figure 2.17 with a system comprised of spherical NPs and diblock copolymer with blocks A and B.¹⁰⁰ The distribution of small, non-selective

particles tend to locate at the interface, whereas larger non-selective nanoparticles that are unable to be incorporated in the BCP domains typically undergo phase separation. Selective nanoparticles that are relatively small and compatible with a particular domain tend to uniformly distribute within the selective block, while larger NPs locate at the center of the selective block to minimize unfavorable entropic penalties associated with polymer deformation. Nanoparticles that are selective to both blocks, *i.e.* Janus nanoparticles, are driven to the interfacial region.

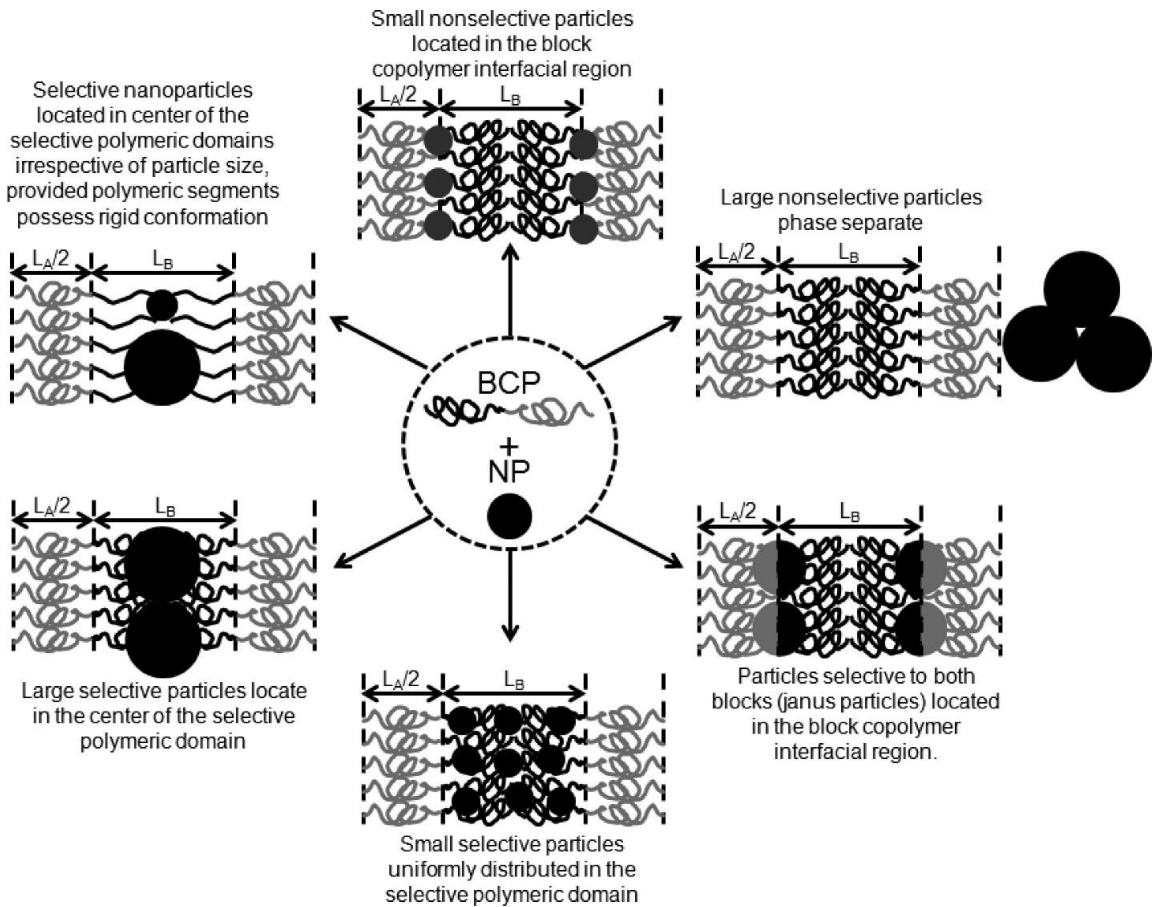


Figure 2.17. Nanoparticle localization in block copolymer systems dependent on the selective or non-selective nature of the particles with the BCP components (block A and block B of size $L_A/2$ and $L_B/2$, respectively) and the nanoparticle size relative to the

polymer radius of gyration. Reprinted with permission from (100). Copyright (2012) American Chemical Society.

The spatial organization and dispersion of nanoparticles in block copolymers are governed by the interplay of entropic and enthalpic driving forces. Surface modification of the NP can be employed to improve enthalpic interactions by grafting polymer ligands with control over variables such as the grafting density, grafted chain length relative to free polymer chain, and brush architecture. For instance, Chiu *et al.*^{101,102} demonstrated precise control over nanoparticle location in lamellar diblock copolymers by altering the composition of ligands on the NP surface. Figure 2.18 displays cross-sectional TEM micrographs with polymer-coated (PS and PVP) gold NPs dispersed in poly(styrene-*b*-2 vinyl pyridine) (PS-*b*-P2VP) and the corresponding histograms to determine particle location.¹⁰¹ The PS-coated gold NPs segregated near the center of the preferential PS domain where the BCP chain ends can move apart to accommodate for nanoparticles rather than incurring a large chain stretching penalty. The gold nanoparticles coated with a mixture of both PS and PVP thiols exhibit a different distribution behavior where modified NPs are driven to the interface between the PS and PVP blocks. This strong adsorption of PS- and PVP-coated nanoparticles to the BCP interface is denoted by a sharp peak in the histogram.

Furthermore, factors such as the size of the nanoparticle d relative to the polymer domain L and particle volume fraction, also influence the location and assembly of nanoparticles.^{103,104} As the volume fraction of PS-coated NPs in PS-*b*-P2VP is increased from approximately 0.07 to 0.32, nanoparticle segregation towards the center of the PS

domain is observed with an absence of particles in the P2VP domains. The normalized distribution profiles denote a slight decrease in the width of the particle distribution with increasing NP concentration. Additionally, the d/L ratio is varied from 0.13 to 0.44 by changing the molecular weight of the BCP. At a fixed particle volume fraction of 0.15, a larger BCP molecular weight results in a broader distribution of particles centralized in the corresponding domain which can be ascribed to entropic contributions to the free energy of the system.¹⁰²

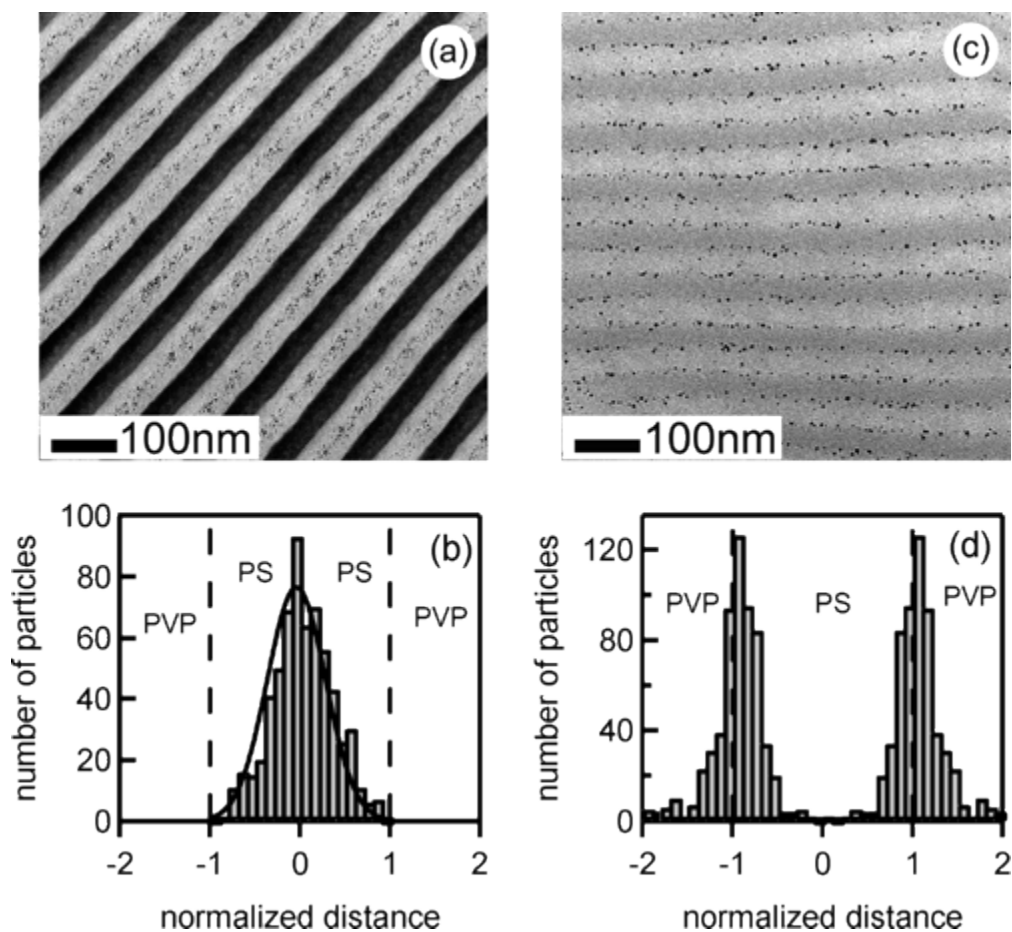


Figure 2.19. Cross-sectional TEM micrographs of a) PS-grafted gold NPs in PS-b-PVP and its corresponding b) histogram displaying the majority of particles localized in the center

of the PS domain, c) PS ad PVP grafted gold NPs in PS-b-PVP with its d) corresponding histogram of particle location at the interface. The histogram represents the number of particles as a function of the normalized distance from the center of the PS domain. Reprinted with permission from (101). Copyright (2005) American Chemical Society.

Recent studies have further examined the dynamics of equilibrium morphology with the incorporation of anisotropic nanoparticles through simulation and experimental work.^{102,104-110} Factors such as the rod length, interaction between the nanofiller and blocks, and nanorod concentration were found to play a key role in the phase ordering process and control over the spatial organization. Through simulations, He *et al.*¹¹¹ investigated the self-assembly and phase behavior of mixtures comprised of mono- or bidisperse nanorods in diblock copolymers. Kim *et al.*¹¹⁰ observed phase transitions from lamellar to other BCP morphologies induced with a significant nanoparticle concentration. In addition to manipulating the nanostructure and localization of particles, the orientation of anisotropic nanoparticles can be controlled by varying the size of the polymer domain relative to the NP which is displayed in Figure 2.20.^{112,113}

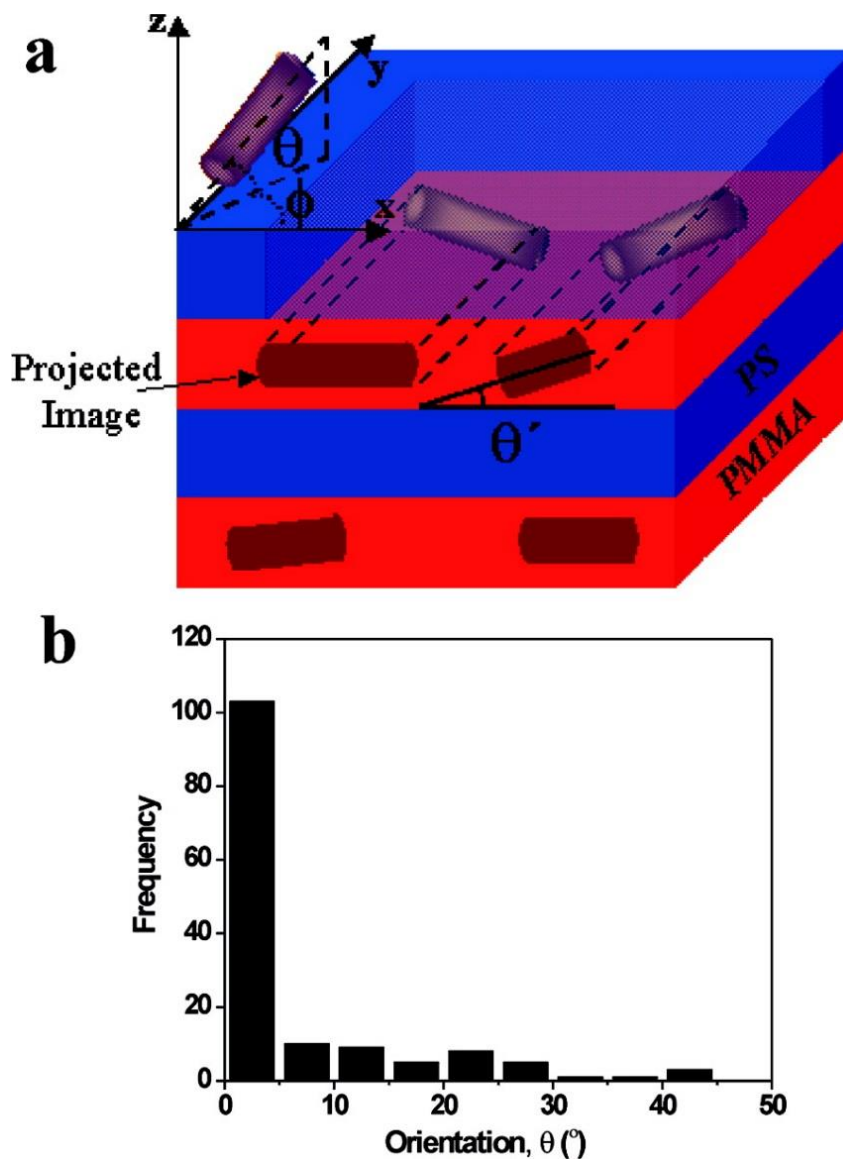


Figure 2.20. a) Schematic of nanorods in lamellar block copolymer with nanorods confined within the center of PMMA domains and b) frequency distribution of nanorod orientation with respect to the lamellae. Reprinted with permission from (112). Copyright (2007) American Chemical Society.

Deshmukh *et al.*¹¹² examined the self-assembly and orientation of gold nanorods modified with a poly(ethylene glycol) (PEG) brush in poly(styrene-block-methyl methacrylate) (PS-*b*-PMMA) with the majority of nanorods oriented parallel to the lamellae. The NRs are subjected to a degree of confinement imposed by the polymer domain by varying the nanorod dimensions with respect to the lamella period L , where the average NR length, NR diameter, and lamellar width of the PMMA domain are $0.71L$, $0.27L$, and $0.5L$, respectively. The nanorods were selectively sequestered in PMMA domains due to favorable interactions between the PMMA block and PEG brush wherein the two-dimensional confinement effect subsequently orients approximately 71% of the nanorods with their long axis within $\pm 5^\circ$ of the lamellae plane. This preferred NR orientation was ascribed to the enthalpic penalty that would result from unfavorable interactions between PEG and PS, as well as the entropic penalty associated with the deformation of PMMA chains to accommodate for the inserted NR.

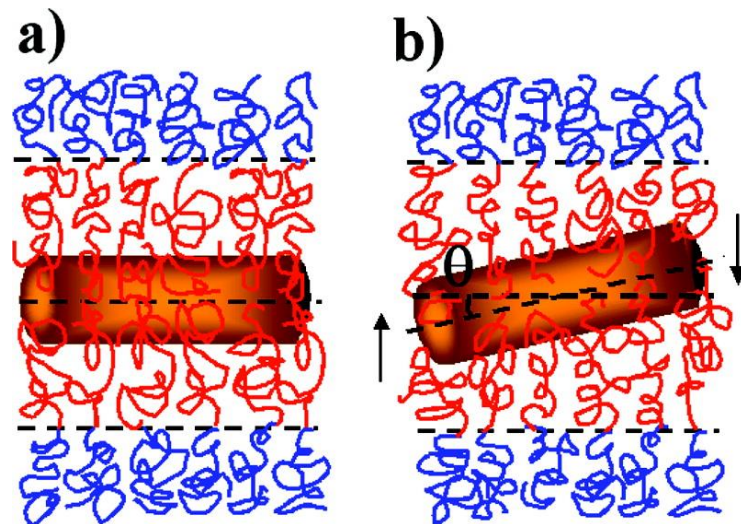


Figure 2.21. Representative model of nanorod in lamellae block copolymer at orientation a) 0° and b) θ° with respect to lamellae. The arrows represent the force exerted to

accommodate for the nanorod. Reprinted with permission from (112). Copyright (2007) American Chemical Society.

Lo and Lin¹¹⁴ also investigated the effect of rod length and orientation distribution of PVP-grafted magnetic nanorods in PS-*b*-P2VP through microscopy and X-ray scattering techniques. However the increasing van der Waals (vdW) interactions and magnetic interactions between particles were shown to initiate extensive nanorod aggregation which amplify local fluctuations, perturb the BCP morphology, and induce a transition from well-ordered to completely disordered nanostructures where the NR-BCP system undergoes macrophase separation.

Moreover, Balazs *et al.*¹¹⁵ determined the equilibrium morphology of confined rod-like particles in microphase separated diblock copolymer mixtures and the material's subsequent elastic properties. The spatial distribution of nanorods was controlled by tailoring the aspect ratio of the particles, as well as the particle-polymer interactions. For selective interactions, smaller particles acquire a higher degree of translational entropy than larger particles and thus uniformly distribute within the compatible BCP domain whereas larger particles localize at the center of the domain to minimize the corresponding conformational entropy loss. Through Self Consistent Field Theory (SCFT) and Density Functional Theory (DFT), the Young's modulus was correlated to the particle dimensions in terms of varying aspect ratio (AR) from 2 to 12, resulting in a significant increase in modulus with increasing aspect ratio. In comparison to low AR particles, the longer rods display a more efficient stress transfer from the matrix to the particles and exhibit larger stress concentrations. The spatial organization of high AR particles was reflected in the

elastic properties where a uniform distribution of particles contributed more to the overall material reinforcement, as compared to enhancement in small, localized regions from the selective rods confined within its compatible domain.

CHAPTER III

CONTROLLED DISPERSION AND SPATIAL ORGANIZATION OF CELLULOSE NANOCRYSTALS USING BLOCK COPOLYMER SCAFFOLDS

3.1 Introduction

The development of engineered hybrid multiphase materials has technological importance in emerging applications ranging from smart coatings, biodegradable anti-microbial food packaging, microelectronics, advanced membranes, capacitors, and photonic devices.^{105,116–121} Nanoparticles offer a unique ability to impart functionalities to polymeric materials with facile tunability in the desired optical, thermal, mechanical, or electrical properties due to their high surface area to volume ratio. The particle geometry (namely size and shape) plays a key role on the inherent macroscopic performance of polymer nanocomposites. The anisotropic nature of the nanoparticle, in particular, has been demonstrated to drastically enhance the mechanical integrity and robustness of composite materials. As a result, rod-like nanofillers have been recently exploited as effective reinforcing agents within a polymer matrix through both experimental and simulation studies. Factors such as nanoparticle aspect ratio (*length/width*), alignment, dispersion, and interfacial stress transfer contribute to the distribution of the applied external stress load on the polymer film to the nanorods.^{67,122–124} This mechanical enhancement is attributed to the synergistic effect arising from the incorporated additives, the polymer

matrix chains, and more importantly, from the interfacial region (termed '*interphase*') resulting from the strong interactions and interfacial adhesion between the particle and polymer matrix.

However, to optimize the composite's desired properties, the challenge lies in controlling the self-organization and dispersion of nanoparticles within the polymer matrix. The organization of NP arrays is mainly governed and driven by the interplay of entropic and enthalpic interactions.^{51,125} The incorporation of nanoparticles within a polymer matrix may result in an enthalpic penalty due to unfavorable interactions between the "free" polymer chain and nanoparticle whereas an entropic penalty may arise from polymer chain stretching to accommodate for the NP. Surface chemistry modification is a widely used technique to improve weak enthalpic interactions where parameters such as the grafting density, chain length, and grafting architecture influence the NP dispersion and film morphology.^{63,126,127}

While controlled thermodynamic interactions are observed to direct the spatial distribution of nanoparticles, recent studies have shown techniques such as layer-by-layer assembly or multi-layer co-extrusion as a means of fabricating layers of controlled thickness and have been demonstrated to act as templates to organize nanoparticles to tune desired functionalities. However, as the number of layers increase, non-uniformity and consequent heterogeneities throughout the film can have detrimental effects on material performance. In this regard, block copolymers (BCPs) are sought as an alternative and efficient approach to generate complex hierarchical nanostructures through directed self-assembly (DSA). Block copolymer chains can undergo microphase separation to form spheres, cylinders, lamellae, and gyroid morphology with periodic structures typically on

a length scale of 5-100 nm. In this regard, BCPs can act as ideal nanostructured templates to selectively sequester and organize nanofillers. Recent studies have examined the dynamics of equilibrium morphology with the incorporation of nanoparticles of varying geometry (particle size and shape) through simulation and experimental work.^{102,103,110,112,128,129} Factors such as the rod length, interaction between the nanofiller and blocks, and nanorod concentration were found to play a key role in the phase ordering process.¹¹¹ The shape and size of the nanoparticle relative to the radius of gyration have been investigated and demonstrated to control the nanorod alignment within the center of its preferential confined domains to minimize the associated chain stretching penalty. Furthermore, the translational particle entropy and molecular mobility of polymer segments can govern the NP spatial distribution in microphase separated morphologies whether localized within a selective block or at the interface to reduce interfacial tension between the blocks.

In this work, we exploit a model symmetric diblock copolymer (PS-*b*-PMMA) as an ideal nanostructured template to selectively sequester and organize rod-like nanofillers *i.e.* cellulose nanocrystals (CNCs). Cellulose nanocrystals (model 1-D anisotropic nanomaterials) have been demonstrated to act as effective reinforcing agents when incorporated into polymer matrices such as PLA, PVA, PMMA, and PEO to create novel sustainable nanomaterials.¹³⁰⁻¹³³ Cellulose is the world's most abundant biopolymer and incorporation of CNCs in polymers offers a greener route in product development due to its high strength to weight ratio (low density of 1.6g/cm³), low thermal expansion coefficient, high crystallinity, liquid crystalline nature, and non-toxic properties. However, strong inter- and intra-molecular hydrogen bonding interactions between individual CNCs

result in nanoparticle aggregation. We demonstrate the controlled dispersion of bio-based nanorods by manipulating the interparticle and particle-polymer interactions *via* hydrogen bonding between the cellulose nanocrystals and diblock copolymer. Short polymer chains, namely PMMA, are grafted onto the CNC surface to increase miscibility between the polymer matrix and grafted brush, and selective dispersion within the preferential domain block due to favorable enthalpic interactions. While the brush length and grafting density play a considerable role on nanoparticle dispersion, the grafted brush was fixed in this study while the grafting density was varied. As a result, thermodynamic interactions are tailored to develop a fundamental understanding on the nanoparticle orientation, dispersion, and spatial distribution within a polymer matrix and its subsequent BCP morphology. By dispersing CNCs in a self-assembled nanostructured BCP, we seek to understand the nanoconfinement constraints and packing frustrations associated with the self-assembly and phase behavior of nanorods as a function of nanofiller concentration.

3.2. Experimental Design

Materials: Poly(methyl methacrylate) (PMMA) with average molecular weight 27 kg/mol and poly(styrene-block-methyl methacrylate) (PS-b-PMMA) with total molecular weight of 66 kg/mol were purchased from Polymer Source Inc. and used as received. The reported polydispersity index (PDI) for both polymers was 1.09. A partially deuterated dPS-b-PMMA with an average molecular weight of 27 kg/mol was used specifically for neutron reflectivity studies and used as received from Polymer Source. N,N-Dimethylformamide (DMF) (ACS reagent, $\geq 99.8\%$) was purchased from Fisher Scientific and used as received. Polished silicon wafers were purchased from University Wafer with a reported

1-0-0 orientation and resistivity of 56.0-72.5 Ω cm. The diameter and thickness of each wafer is 150 mm and 625 ± 15 μm , respectively.

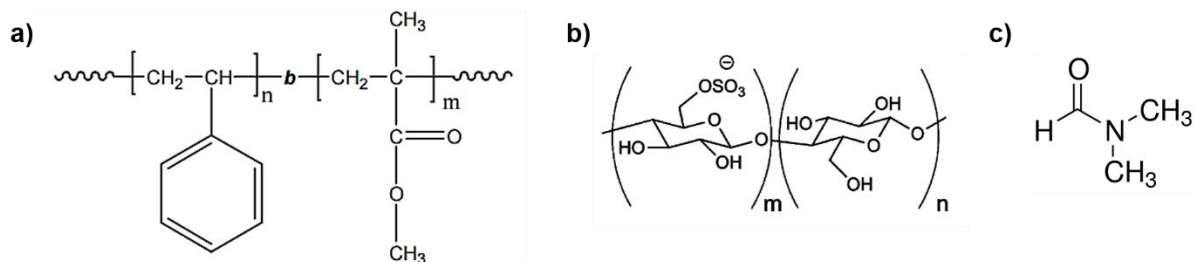


Figure 3.1. Molecular structure of poly(styrene-block-methyl methacrylate), b) cellulose nanocrystals referred to as unmodified CNCs in this work, and c) DMF.

Cellulose nanocrystals were purchased from the University of Maine and received as a 6.2 wt% CNC aqueous suspension. Extraction of native cellulose from a wood pulp source was hydrolyzed using sulfuric acid to further break down and remove amorphous regions of the microfibril. Due to the sulfuric acid hydrolysis procedure, sulfate half-ester groups are introduced onto the nanorod surface, resulting in electrostatic repulsions and colloidal stability. Sulfur content is approximately 0.7% which is determined through XPS measurements. PMMA-grafted-CNCs were synthesized by Cranston Research Group in the Chemical Engineering Department at McMaster University through a one-pot free radical polymerization method in a grafting-from approach. The synthesis is displayed in Figure 3.2 with ceric ammonium nitrate as the initiator.

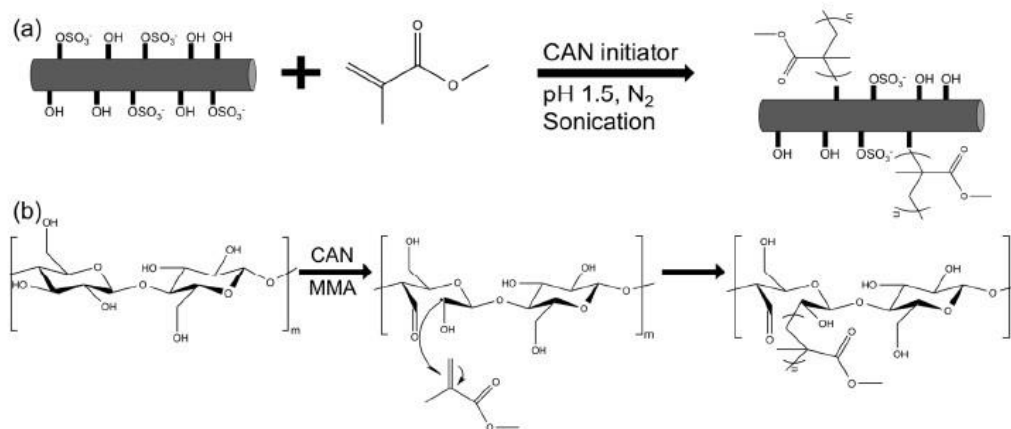


Figure 3.2. Synthesis of PMMA-grafted-CNCs *via* radical polymerization.

Fabrication of Polymer Nanocomposite Thin Films: Polymer solutions are first prepared by mixing 0.5 g of PMMA in 4.5 g of DMF and stirring for 6 hours on a Vortex mixer to ensure a homogenous solution. The PMMA/DMF solution was then filtered using a 0.45 μm GMF filter to remove any contaminants or impurities. Similarly, another solution was prepared in a separate glass vial for PS-b-PMMA/DMF following the same procedure as PMMA. The CNC aqueous suspension (6.2 wt%) was diluted with DMF solvent to achieve a concentration of 1 mg/ml (CNC content with respect to solvent). The 1 mg/ml CNC solution was placed in the sonicator bath (VWR B2500A-MTH model) for 2 hours until completely mixed. Solutions of nanoparticles in polymers were prepared by mixing the separately-made solutions of CNCs (1mg/ml) and polymer (PS, PMMA, and PS-b-PMMA) as a function of nanofiller concentration at 0 wt%, 0.5 wt%, 1 wt%, 2.5 wt%, 5 wt%, 10 wt%, and 20 wt% CNCs in polymer. For these studies, wt% refers to the weight of the CNCs with respect to the weight of the homopolymer or block copolymer. The CNC/polymer solutions were placed in the sonicator for 4 hours to ensure good dispersion.

It is important to note that the particle/polymer solutions were not filtered to reflect accurate representation of its dispersed or aggregated states with the reported particle concentration.

Polymer nanocomposite (PNC) thin films were cast on silicon substrates *via* a flow coating technique.¹³⁴ Prior to flow coating, silicon substrates were subjected to UV-ozone exposure in a Novascan PSD Series Digital UV Ozone System for approximately 1 hour to remove any organic impurities. A thin oxide layer (approximately 2-5 nm) was formed on the silicon substrate (SiO_x) from UVO exposure. PNC thin films were created by adjusting the flow coating speed and acceleration for each solution to generate step gradient film thicknesses ranging from 50 to 400 nm. Due to the high boiling point of DMF (153°C), a heating stage was set up on the flow coater to create uniform films as shown in Figure 3.3. This customized setup was found to facilitate solvent evaporation and minimize solution backflow upon casting a polymer film. The polymer film thickness was measured using a Filmetrics F20-UV thin film interferometer.

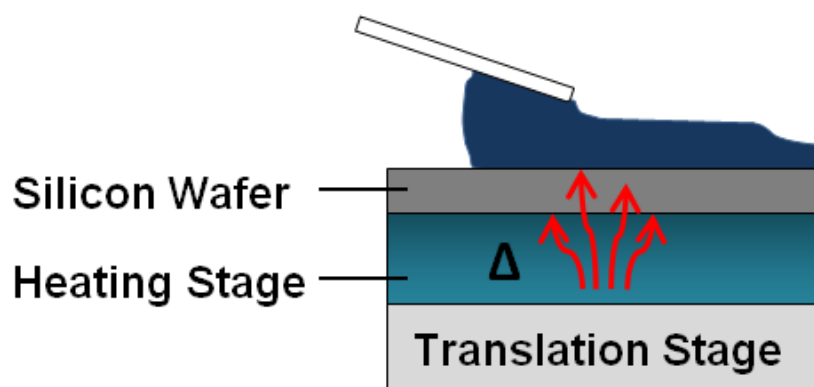


Figure 3.3. Modified flowcoating assembly with a heating stage placed below the silicon wafer to facilitate solvent evaporation and generate films of uniform thickness.

Characterization of Film Morphology: The surface topography was characterized with atomic force microscopy (AFM) using a Dimension ICON (Veeco). Data was collected in Tapping mode, with contrast arising between the particles and matrix giving rise to height and phase profiles. Micrographs obtained through AFM imaging were further analyzed for average particle dimensions with NanoScope Analysis software. Cross-sections of the microphase separated lamellar block copolymer thin films were examined using a Focused Ion Beam (FIB) lift-out technique with transmission electron microscopy at the National Institute of Standards and Technology (NIST).

Thermogravimetric analysis (TGA) studies were performed using a TA Instruments TGA Q50 model to gain insight into the thermal degradation behavior of CNCs. The samples were prepared by drying the CNC aqueous suspensions, or heating under vacuum at 120°C for 24 hours to allow for water evaporation. For each TGA measurement, the sample was heated from 26°C to 700°C at a heating rate of 10°C/min under nitrogen. Data was further analyzed with TA Universal Analysis software to determine the derivative of mass as a function of temperature. Fourier transform infrared spectroscopy (FTIR) data was collected using a Thermo Scientific Nicolet iS50 FT-IR spectrometer. Double-sided polished silicon wafers were used specifically for these studies. Polymer nanocomposite thin films were prepared with varying CNC concentration ranging from 0 to 10 wt% in PS-b-PMMA. The FTIR spectra was obtained in absorbance mode for each sample and baseline corrections were applied using the Thermo Scientific OMNIC software.

To investigate BCP thin film morphology, grazing incidence small angle X-ray scattering (GISAXS) measurements were carried out at Argonne National Laboratory Advanced Photon Source at Sector 8-ID-E beamline. An X-ray beam was impinged on each substrate-supported nanoscale film at a range of incident angles (above and below the film critical angle) with a 7.35 keV energy. A Pilatus 1M detector was used to collect scattering data and GIXSGUI software was used for further data analysis and linecuts.

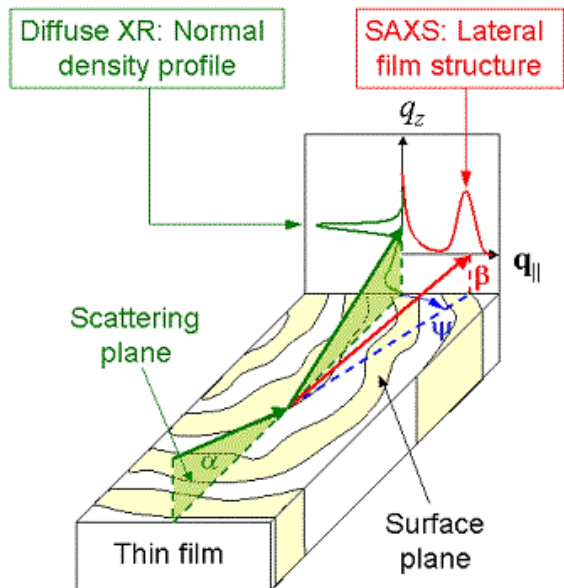


Figure 3.4. Grazing incidence small angle X-ray scattering (GISAXS) geometry. Reproduced with permission from [135].

Neutron reflectivity measurements were performed at the National Institute of Standards and Technology Center for Neutron Research (NCNR) on the NG-7 horizontal neutron reflectometer. A partially deuterated BCP (dPS-b-PMMA) was used in this study

to generate sufficient contrast between components. Thin film samples were scanned over a wave vector q_z range from 0.006 to 0.16 \AA^{-1} with an incident neutron wavelength of $\lambda = 4.75 \text{ \AA}$. ReflPak software was used for data reduction and fitting.

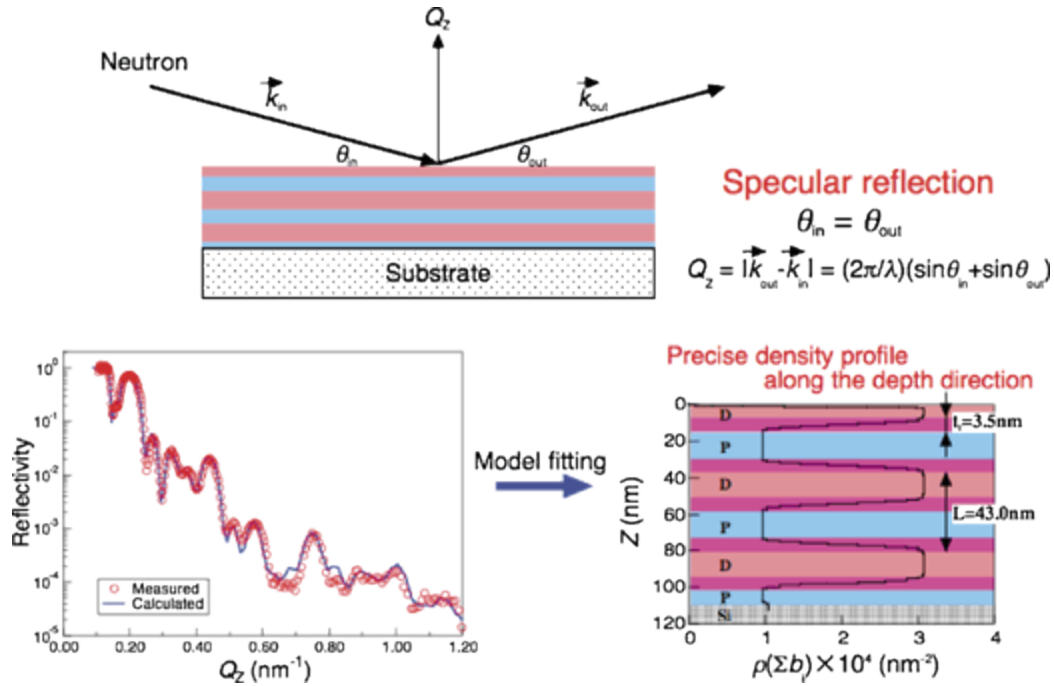


Figure 3.5. Typical geometry of neutron reflectivity with sample reflectivity curve and model fitting. Reproduced with permission from [136].

3.3 Results and Discussion

To investigate the spatial distribution and localization of cellulose nanocrystals in polymer nanocomposite thin films, detailed characterization of the cellulose nanocrystals was first carried out through microscopy and X-ray scattering techniques. It was of critical importance to examine the physical and thermal properties of the nanoparticles prior to dispersing in polymers. Surface topography was examined using atomic force microscopy

(AFM) tapping mode to determine average CNC dimensions. A dilute suspension of pure cellulose nanocrystals in DMF (1 mg/ml) was drop cast onto a silicon oxide substrate to fabricate thin films. The film thickness, h , was utilized to act as 1D confinement, such that nanorods are forced to lie in-plane or within a fixed orientation when $h < L_{NR}$. Figure 3.6 shows a representative AFM micrograph based off phase contrast. Phase imaging reveals CNC dimensions with average length and width of approximately 135 nm and 5.9 nm, respectively. This results in an average aspect ratio of 23 and is summarized in Table 1. The distribution of sizes is mainly due to the cellulose source, extraction process, and specific hydrolysis conditions.

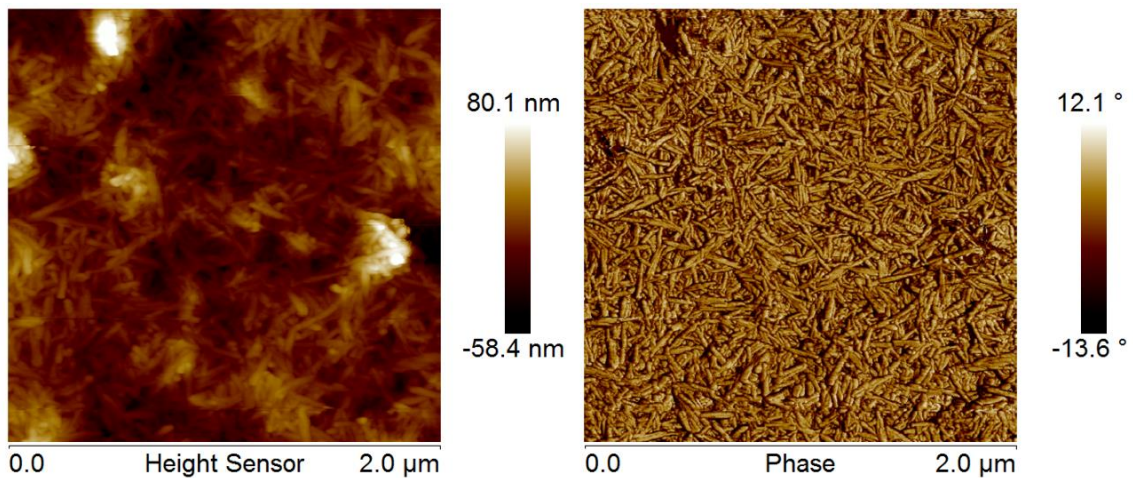


Figure 3.6. AFM micrographs of height and phase images displaying pure cellulose thin films drop cast on silicon substrates from dilute aqueous suspensions. Scan size is 2 μm .

Table 1. Cellulose nanocrystals average dimensions			
Type of CNC	Average length	Average width	Aspect ratio
Unmodified CNCs	130 ± 67 nm	5.9 ± 1.8 nm	23 ± 12

The thermal stability of these rod-like nanoparticles is of critical importance to determine suitable thermal processing conditions and its practicality in potential applications. For our block copolymer system used in this particular study, thermal annealing (above glass transition temperature T_g) was employed to impart sufficient mobility to polymer chains to undergo microphase separation. As such, thermogravimetric analysis (TGA) was performed to investigate the thermal behavior of CNCs. This allows us to find a suitable annealing temperature for the BCP/CNC thin films to ensure the organic NPs are not degrading upon annealing.

The TGA curve of CNCs is shown in Figure 3.7 where weight % is plotted as a function of temperature. A minor weight loss (< 5%) was observed in the lower temperature region, arising from the evaporation of water. Unmodified CNCs are observed to have an onset of degradation at 210°C, which confirms thermal stability of CNCs when annealed well below T_{deg} at 180°C. This lower degradation temperature was attributed to the presence of sulfate groups on the CNC surface from the hydrolysis treatment. While the introduction of surface sulfate groups may contribute to colloidal stability in an aqueous suspension, it has also been reported to act as a dehydration catalyst to facilitate the decomposition mechanism.^{137,138} As a result, the activation energies are significantly lowered which leads to lower thermal stability behavior. The thermal degradation profile can be described by a two-step pyrolysis process, where T_{deg1} has been reported to occur between 150°C and 300°C and T_{deg2} between 320°C and 500°C. From the thermal analysis profile, nearly 40% of the mass was lost in the former T_{deg1} process. In this primary pyrolysis process, the dehydration reaction first occurs at the more accessible cellulose

chains that are in direct contact with the acid groups (amorphous regions) whereas the latter process was related to the breakdown of the crystal interior and slower decomposition of the charred residue. A significant char yield was observed from the TGA curve, which is characteristic for CNCs hydrolyzed with sulfuric acid. There is approximately 30% of char residue remaining at 700°C, likely attributed to the nanoscale size feature of the particles and free end chains.

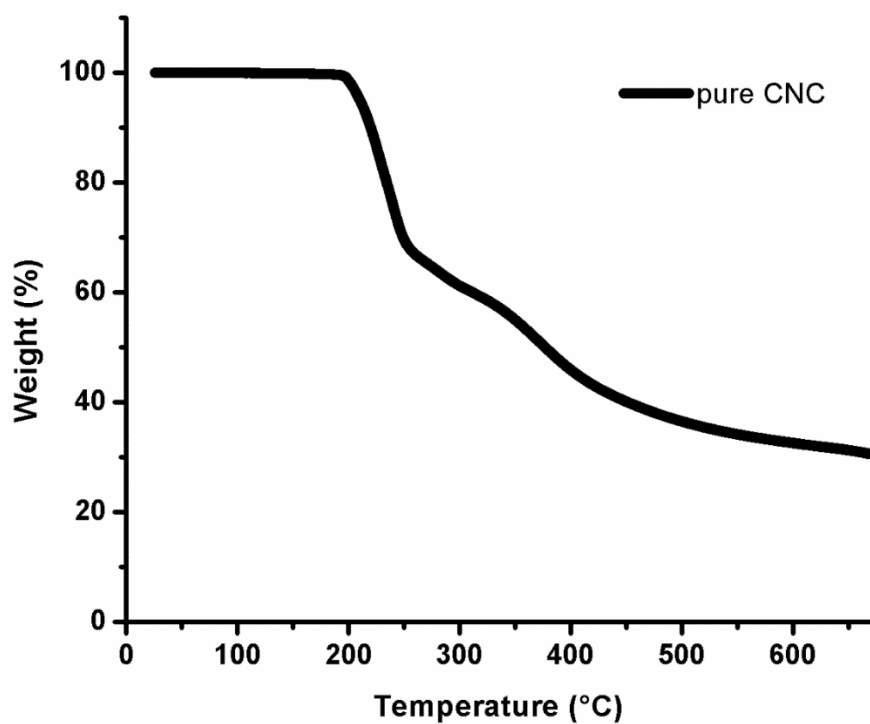
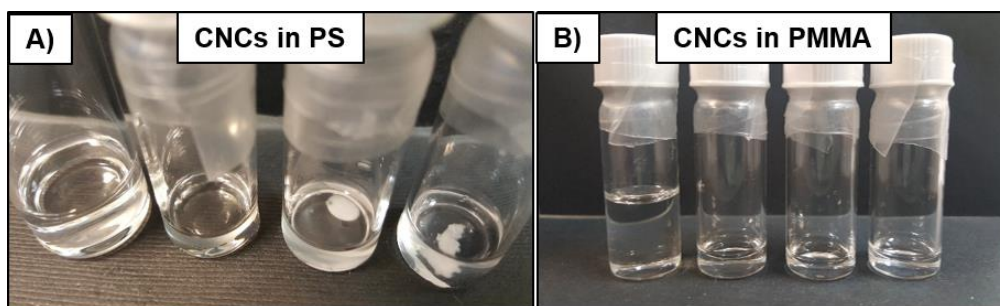


Figure 3.7. TGA curve of unmodified CNCs with sulfate half-ester groups from hydrolysis reaction. Thermal degradation behavior of pure CNCs mainly occurs as a two-step process.

Upon characterizing the cellulose nanocrystals, we next investigate the miscibility of unmodified CNCs in a model diblock copolymer, PS-b-PMMA. It should be noted that CNC dispersion in PMMA was only shown for these studies which can be ascribed to the expected unfavorable interactions with the other BCP component, polystyrene. Due to the

hydrophobic nature of PS, dispersion of hydrophilic cellulosic nanofillers (without any surface chemistry modification) remains a challenge. This can be observed in Figure 3.8a, displaying solutions of increasing nanorod concentration in PS homopolymer after 2 hours of sonication. The CNC concentration was varied from 0 wt%, 1 wt %, 5 wt%, and 10 wt% CNCs in PS (from left to right, respectively). With the higher nanofiller loadings (5 and 10 wt%), the CNCs appear to completely macrophase separate, which is denoted by the visible white gel in solution. This is likely attributed to minimizing any unfavorable interaction between the PS chains and unmodified CNC surface which causes extensive CNC aggregation and network formation from hydrogen bonding, in order to minimize the free energy of the system. In contrast, Figure 3.8b represents solutions of CNCs in PMMA with similar nanofiller concentration ranging from 0 wt% (neat PMMA/DMF), 1 wt% CNCs, 5 wt% CNCs, and 10 wt% CNCs in PMMA. All solutions appeared visibly clear with no noticeable turbidity observed, in which turbid solutions might suggest severe aggregates present.

Figure 3.8. Prepared solutions of unmodified CNCs in glass vials of a) polystyrene and b)



poly(methyl methacrylate) after sonication. The nanofiller concentration was varied from left to right in increasing CNC wt% from 0, 1, 5, and 10 wt%.

The favorable polar interactions between PMMA and cellulose was next examined by understanding the spatial dispersion in a poly(methyl methacrylate) homopolymer of comparable molecular weight to the block copolymer. Surface topography of CNC/PMMA nanocomposite films was characterized through atomic force microscopy (AFM) tapping mode as a function of varying nanofiller, as shown in Figure 3.9.

Representative AFM micrographs are determined from height (a-c) and phase (d-f) contrast between the homopolymer and nanorods. The dark region represents the polymer matrix, whereas the bright areas denote the rod-like cellulosic nanofillers. To gain insight on the spatial dispersion of unmodified CNCs in a polymer matrix, the nanorod concentration was varied from 1 wt%, 5 wt%, and 10 wt% CNCs in PMMA. Individual well-dispersed particles are seen even at high CNC loading (10wt%), with minimal aggregation observed in the AFM micrographs. This is likely attributed to strong hydrogen bonding interactions between the PMMA and cellulose. Figure 3.9 displays cellulose nanocrystals that are randomly oriented with no preferential alignment in a particular direction.

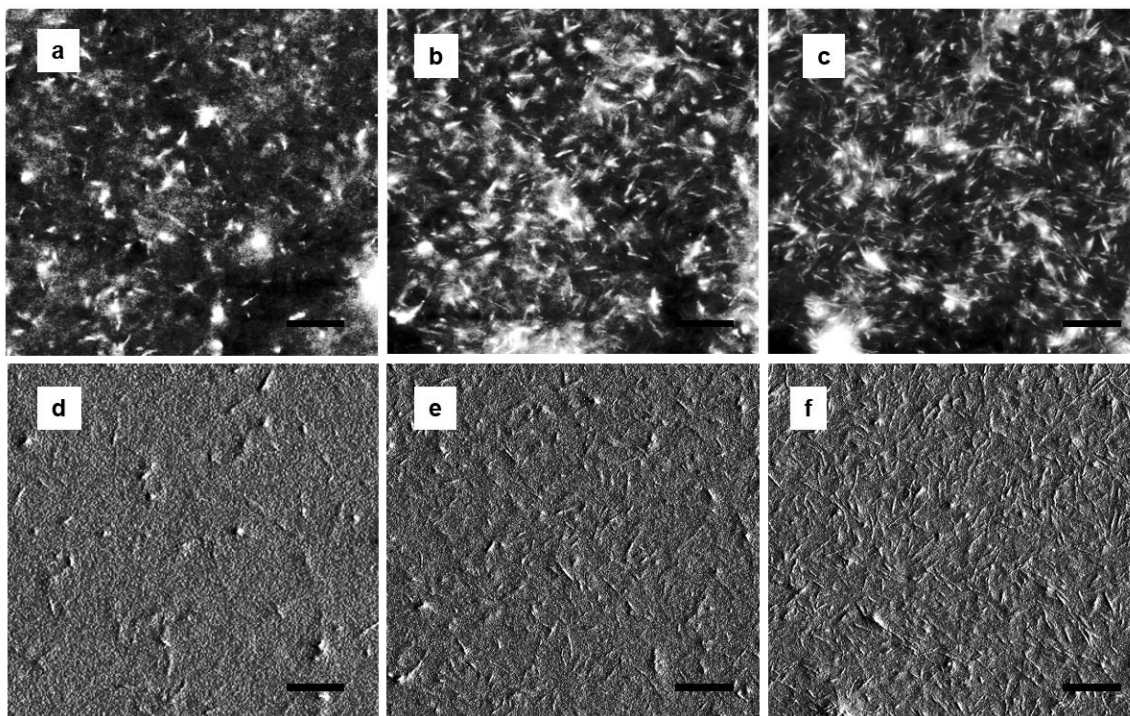


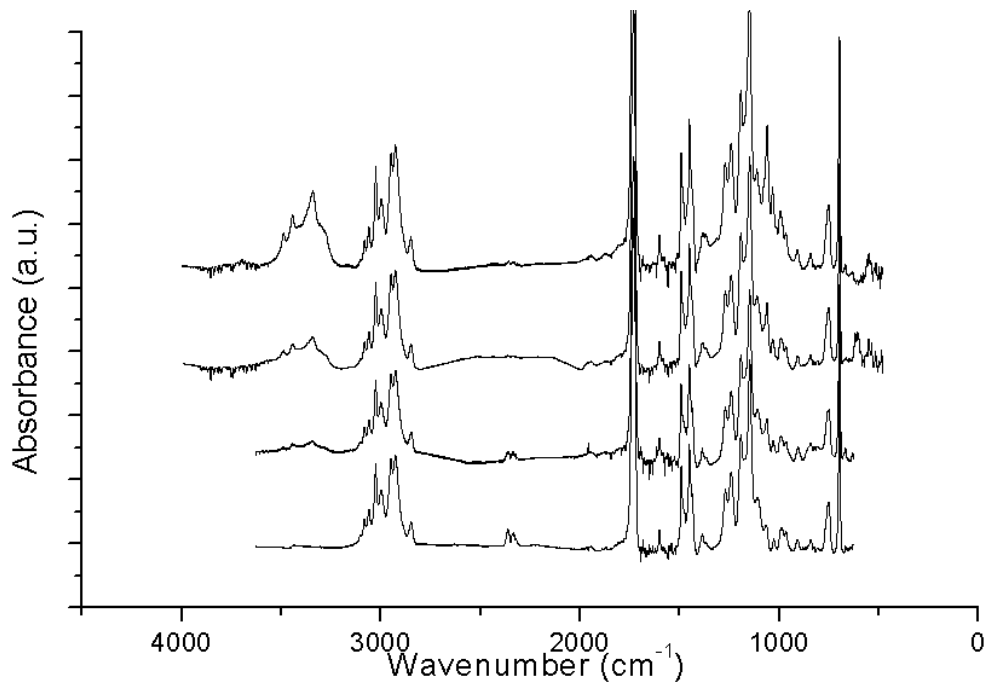
Figure 3.9. AFM height (a-c) and phase (d-f) images obtained with tapping mode as a function of unmodified CNC concentration in PMMA homopolymer. The nanorod concentration is varied from (a,d) 1 wt%, (b,e) 5 wt%, and (c,f) 10 wt% in PMMA. Film thickness for each sample was 50 nm. Scale bar represents 500 nm.

Controlled film thickness (h) in nanoscale thin films can act as 1-D confinement to the orientation and/or alignment of nanorods (NR). More specifically, this can be achieved if $h < L_{NR}$, where L is the average nanorod length. In this study, the film thickness remained fixed at 50 nm for each nanofiller concentration to exploit the nanoconfinement effect. With an average CNC length of 135 nm, a majority of CNCs are expected to be within a fixed orientation range that is predominantly parallel to the substrate. As such, the

AFM height and corresponding phase images can serve as accurate representations for CNC dimensions and its particle dispersion or aggregated states.

However, we seek an additional confinement feature where the spatial distribution and self-organization of CNCs can be controlled within generated nanoscale periodic patterns. The underlying mechanisms governing self-assembly and organization of nanorods under spatial confinement is essential to realize the full technological potential of PNCs in advanced functional materials. In this regard, the directed self-assembly (DSA) of block copolymers (BCP) provides a facile route to create complex morphologies with well-defined nanoscale periodicity that can be manipulated through molecular weight, the volume fraction of components, and segmental interaction parameter χ . The main driving force behind the co-assembly of nanoparticles and block copolymer is the ability to efficiently tune microdomain structures and controlled nanoparticle location in confined BCP domains which is driven by the minimization of free energy. For these studies, the particle size dimensions and shape anisotropy of cellulose nanocrystals relative to the block copolymer domains were taken into account. As such, a model symmetric diblock copolymer poly(styrene-block-methyl methacrylate) was selected for this study, in which the orientation of the lamellar structure was dependent on the substrate affinity and wetting behavior of the blocks.

Figure 3.10. FTIR absorbance spectra of cellulose nanocrystals in PS-b-PMMA with varying CNC concentration. Data is offset for peak clarity.



Fourier transform infrared spectroscopy (FTIR) was used to evaluate the hydrogen bonding interactions between the unmodified CNCs and PS-b-PMMA. FTIR data was studied as a function of nanofiller concentration from 0 wt% (Neat BCP), 1 wt%, 5 wt%, and 10 wt% CNCs in BCP. This was represented by the absorbance spectra, as shown in Figure 3.10 where the data was offset to allow for better clarity of peaks. More specifically, we were interested in the hydroxyl stretching region which is typically in the range from 3100-3600 cm⁻¹. There are four distinct peaks within this region at 3284, 3338, 3440, and 3488 cm⁻¹ which can be attributed to the intermolecular (3284 and 3338 cm⁻¹) and intramolecular (3440 and 3488 cm⁻¹) hydrogen bonding interactions. The peaks are observed to increase in intensity and sharpen with increasing CNC content, suggesting higher densities of hydroxyl groups on the nanorod surface. Additionally, a slight

frequency shift in the 3338 cm^{-1} peak denotes increased hydrogen bonding interactions between the PS-b-PMMA matrix and CNCs. However, this effect is less pronounced due to the sulfuric acid hydrolysis reaction where sulfate groups replaced a significant number of the hydroxyl groups.

To gain insight into the internal nanostructure of these substrate-supported polymer nanocomposite films, grazing incidence small angle X-ray scattering (GISAXS) experiments were performed at Argonne National Laboratory Advanced Photon Source 8-ID-E Beamline. The morphology evolution with addition of cellulosic nanofillers was studied as a function of CNC concentration and compared to the neat block copolymer film (without nanoparticles). GISAXS data was collected over a range of incident angles (α) relative to the polymer critical angle to investigate the film structure in both the out-of-plane q_z and in-plane q_y directions. Information regarding the thin film surface can be revealed at $\alpha < \alpha_c$, whereas $\alpha > \alpha_c$ probes the entire depth of the film. For these studies, there was no observed change in the film morphology from the film surface or bulk at a fixed total film thickness of 250 nm. As such, Figure 3.11 summarizes the two-dimensional (2D) GISAXS patterns of annealed BCP thin films with the addition of cellulose nanocrystals at $\alpha > \alpha_c$, with nanorod concentration varying from a) 0 wt%, b) 0.5 wt%, c) 1 wt%, d) 2.5 wt%, e) 5 wt%, and f) 10 wt% unmodified CNCs in PS-b-PMMA. The line cuts for each data set were taken along the vertical scattering planes and the integrated intensity data was offset for clarification, as shown in Figure 3.12.

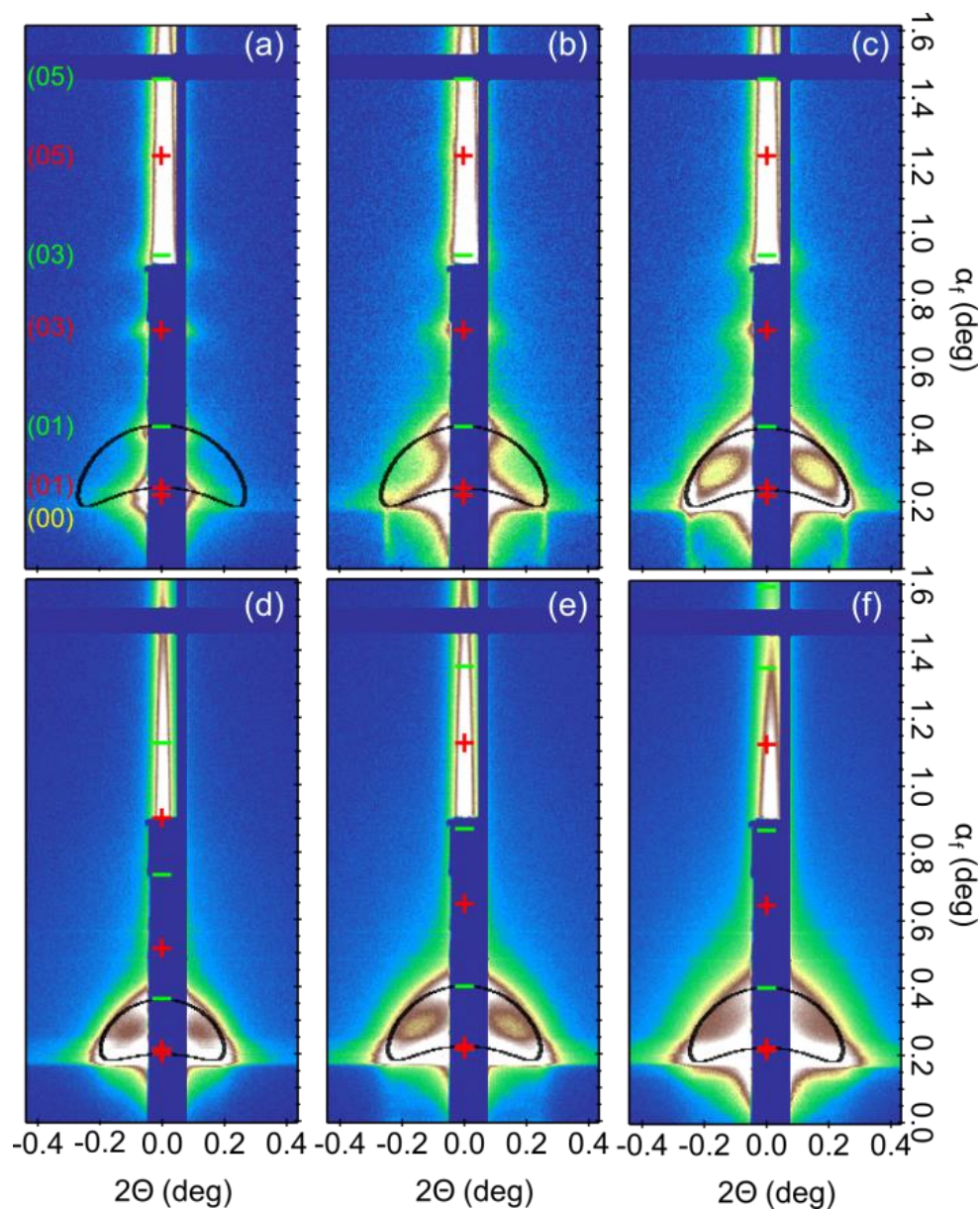


Figure 3.11. 2D Grazing Incidence Small Angle X-ray Scattering (GISAXS) patterns revealing morphology of annealed block copolymer thin films with the incorporation of unmodified CNCs as a function of nanorod concentration at a) 0 wt% (neat BCP film), b) 0.5 wt% CNCs, c) 1 wt% CNCs, d) 2 wt% CNCs, e) 5 wt% CNCs, and f) 10 wt% CNCs. GISAXS measurements were taken above the film critical angle such that the entire film was probed. Film thickness was approximately 400nm.

The morphology of a neat PS-*b*-PMMA (without nanorods) was first investigated through GISAXS measurements. The as-cast BCP thin film attains a kinetically-trapped configuration and disordered state due to solvent evaporation during the film-casting process. Thermal annealing above the glass transition temperature (T_g) of both blocks imparts sufficient chain mobility to microphase separate into periodic arrays of well-defined nanostructures. The resulting microdomain structure is displayed in Figure 3.11a with arrays of lamellar microdomains oriented parallel to the substrate. This can be attributed to the difference in surface tension of BCP components, where the surface energy of PS and PMMA is reported as $\gamma_{PS} = 40.7 \text{ mJ/m}^2$ and $\gamma_{PMMA} = 41 \text{ mJ/m}^2$, respectively. The lower surface energy drives PS to the air-polymer interface and PMMA segregates to the native oxide interface on silicon forming a wetting layer. The strong substrate and surface interactions propagate throughout the film, inducing a parallel orientation of lamellar microdomains. Multiple Bragg peaks observed exclusively in the out-of-plane (q_z) direction and the absence of peaks in the in-plane (q_y) direction are indicative of completely parallel lamellae exhibiting long-range order throughout the annealed BCP film.

To understand the underlying mechanism governing the co-assembly of CNCs in self-assembled nanostructured templates, the film morphology was studied as a function of nanorod concentration ranging from 0.5 to 10 wt% CNCs in PS-*b*-PMMA. In the previous section, the effect of nanofiller concentration was studied in detail to gain insight into how individual CNCs disperse within each BCP component (PS and PMMA). However, the addition of anisotropic nanoparticles in block copolymers becomes significantly more

complex, where the directed self-assembly (DSA) process and subsequent film morphology can be influenced by factors such as chain stretching, packing frustration, and interfacial interactions. As such, it is important to gain a fundamental understanding on how BCP self-assembly drives the distribution and alignment of CNCs within confined domains.

Figure 3.11b displays the 2D GISAXS patterns of symmetric diblock copolymer PS-*b*-PMMA with the addition of 0.5 wt% unmodified CNCs. Similar to the neat BCP, prominent Bragg peaks in the q_z direction were evident. However, the incorporation of CNCs also gives rise to an in-plane structure component which suggests mixed orientation throughout the film. The distribution of lamellar orientations broadens as a function of increasing CNC concentration from 0.5 to 10 wt%. Loss of higher-order peaks in the out-of-plane direction were observed with the addition of 2 wt% unmodified CNCs in PS-*b*-PMMA thin films. At higher CNC concentrations, the GISAXS patterns revealed a fairly disordered and isotropic structure which is represented by the broad ring.

The characteristic domain spacing or equilibrium repeat period (L_0) was extracted from the relationship $L_0 = 2\pi/q$. From GISAXS analysis, the annealed BCP film without nanorods had a measured domain spacing of 36.5 nm. With the addition of 1 wt% unmodified CNCs, the domain spacing increased to 37.4 nm and systematically increased to 39.5 nm with 5 wt% unmodified CNCs.

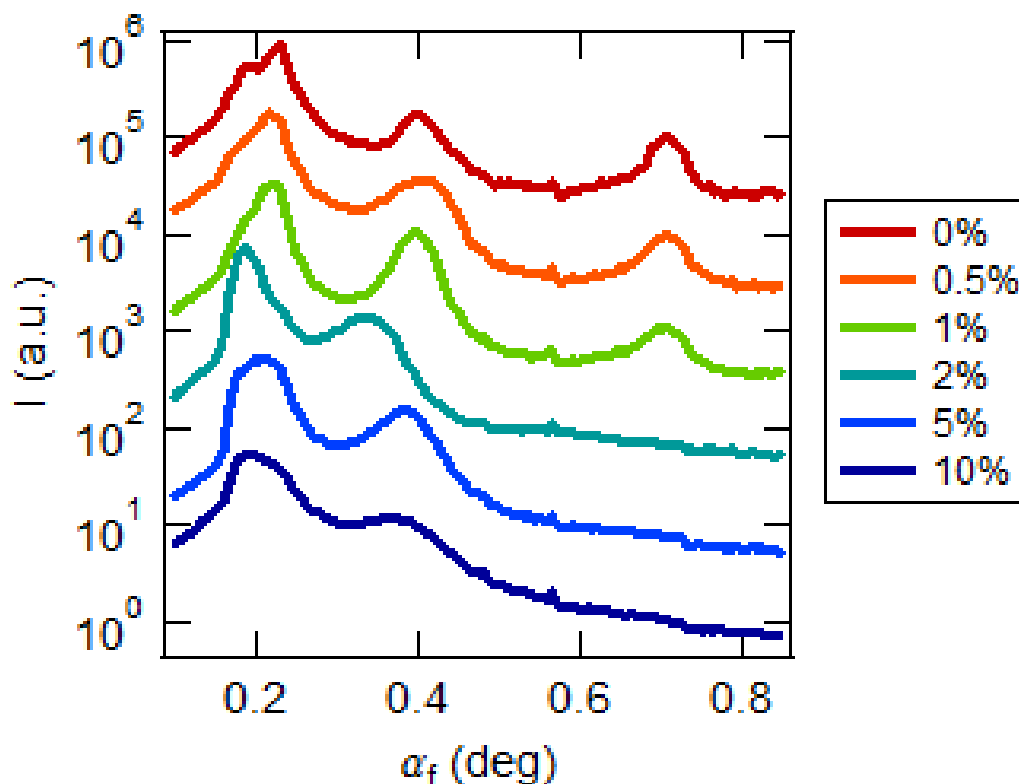


Figure 3.12. GISAXS 1D profiles reflect out-of-plane linecuts with data curves offset for each nanofiller concentration in PS-b-PMMA ranging from 0 to 10 wt%.

From the 2D GISAXS data and its corresponding linecuts, the loss of long-range order can be ascribed to the strong intra- and inter-molecular hydrogen bonding interactions between individual cellulose nanocrystals which increased its susceptibility to aggregate. To minimize unfavorable interactions with PS, the unmodified CNCs form localized particle-rich regions which, in turn, perturb the lamellar structure and BCP morphology. In comparison with spherical nanoparticles of smaller dimensions

(comparable or less than the R_g), nanorods with significantly larger volume cannot as easily be distributed and accommodated between neighboring polymer chains. In fact, this leads to an energetic penalty that consequently excludes CNCs from the block copolymer to recover from its entropic and enthalpic loss and achieve the lowest free energy state.

To further understand the morphology obtained from X-ray scattering, transmission electron microscopy (TEM) was used to confirm the BCP nanostructure with real-space imaging. Cross-sections of nanoscale films on silicon substrates were obtained through a focused ion beam (FIB) lift-out technique. Figure 3.13 displays the TEM cross-sections of annealed thin films of a) PS-b-PMMA without CNCs and b) 5 wt% unmodified CNCs in PS-b-PMMA. The neat BCP film in Figure 3.13a displayed a multi-layer structure with lamellar microdomains oriented parallel to the substrate, which is in agreement with GISAXS results. The light and dark phases in the TEM micrographs correspond to PMMA and PS microdomains, respectively. As illustrated in Figure 3.13b, the completely parallel lamellar morphology was disrupted with the addition of 5 wt% CNCs. While GISAXS data analysis suggested a broad distribution of lamellar orientations, the nanostructure could not be resolved with TEM where clearly defined domain structures proved difficult to detect and can be ascribed to insufficient imaging contrast.

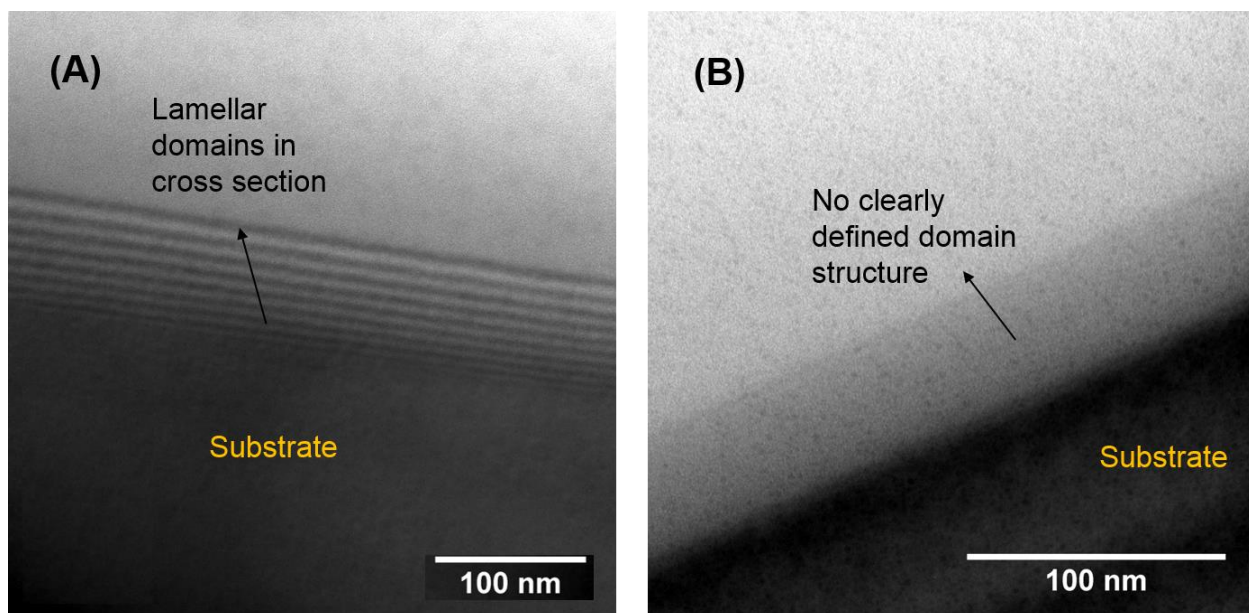


Figure 3.13. TEM images of BCP cross-sectional profiles prepared by a focused ion beam (FIB) lift-out technique. The representative micrographs of annealed a) neat BCP thin film with lamellar microdomains ordered parallel to the substrate and b) PS-*b*-PMMA with addition of 5 wt% unmodified CNCs.

Nevertheless, the introduction of unmodified CNCs (even at 0.5 wt%) caused the loss of multi-layer structure with long-range order. This can be ascribed to strong intra- and intermolecular hydrogen bonding interactions between individual CNCs which caused extensive particle aggregation and eventually resulted in macrophase separation. To overcome current limitations, manipulation of the interparticle and particle-polymer interactions were sought to gain better control over individual particle dispersion, orientation, and spatial arrangement due to self-organization. More specifically, the nanoparticle surface chemistry was modified through the abundance of reactive hydroxyl

groups on the surface of cellulose to increase the compatibility between particles and free polymer chains.

To fully understand the interplay of particle-polymer and particle-particle interactions, the cellulose nanocrystals were tailored by grafting PMMA chains onto the surface through atom transfer radical polymerization (ATRP) reactions as outlined in the experimental section. In this study, a polymer brush was grafted to the CNC surface in a “grafting-from” approach to tailor compatibility with the polymer matrix and aid in the particle dispersion. When the brush and free polymer chains are chemically similar to promote nanofiller dispersion, this results in an *athermal* case. Here, the Flory-Huggins interaction parameter $\chi \approx 0$ and particle dispersion is mainly governed by $\alpha = P/N$ where P and N is the degree of polymerization of the free polymer (matrix) chains and brush chains, respectively. While the brush length and grafting density influence the particle aggregation and dispersion states, the length of the grafted PMMA chain was fixed in this study but will potentially be studied in the future to examine chain brush conformation in further detail.

The particle dispersion was investigated in these studies as a function of polymer grafting density ranging from 0.05 chains/nm², 0.25 chains/nm², and 0.33 chains/nm² which can be referred to as low grafting density (LD), medium grafting density (MD), and high grafting density (HD), respectively. The molecular weight and polydispersity index of the PMMA grafted chains were reported, as determined from free polymer prepared with sacrificial initiator. The MD PMMA-g-CNC had a number average molecular weight (M_n) and weight average molecular weight (M_w) of 22.3 kg/mol and 26.2 kg/mol, respectively, which yields a polydispersity index (PDI) of 1.18. The HD PMMA-g-CNC had a M_n of

19.7 kg/mol and M_w of 22.9 kg/mol, resulting in a PDI of 1.16. The poly(methyl methacrylate)-grafted-cellulose nanocrystals (PMMA-g-CNCs) were observed to have a sulfur content of approximately 0.7% from X-ray photoelectron spectroscopy measurements, which is similar to the unmodified CNCs (due to sulfuric acid hydrolysis reaction for CNC production). From AFM measurements, the average particle dimension sizes have a measured length and height of 110 nm and 5 nm. It should be noted that the weight percentage was reported for these studies where the mass of CNCs was varied with respect to mass of polymer. As such, for comparable CNC concentrations at different grafting densities, there exists a slight variation in the number of individual nanorods present in the polymer.

The incorporation of synthesized PMMA-grafted-CNCs in a chemically similar polymer matrix was first investigated to understand the effect of grafting density on nanorod dispersion. AFM phase imaging was used to characterize the surface topography of PMMA-g-CNCs in PMMA homopolymer (molecular weight 30 kg/mol) of varying grafting density (LD, MD, and HD) and nanorod concentration (1, 5, and 10 wt% CNCs). This was summarized in Figure 3.14 where the dark phase corresponds to the polymer matrix and the light phase corresponds to the rod-shaped nanoparticles. Extensive particle aggregation was observed for the lower grafting density (LD PMMA-grafted-CNC) at higher CNC concentrations (5 and 10 wt%), as shown in Figure 3.14b-c.

However, as the polymer grafting density is increased, the particle dispersion was improved. This was demonstrated to occur in a systematic manner as a function of increasing grafting density where the number and size of particle aggregates or CNC bundles decreased. In the case of HD PMMA-grafted-CNCs, the cellulose nanocrystals

achieved good dispersion in the PMMA matrix, as displayed in Figure 3.14i. The individually well-dispersed nanorods were randomly oriented with no clear alignment in a particular direction, suggesting an isotropic distribution throughout the matrix. A noteworthy observation was the aggregation state of PMMA-g-CNCs in comparison to the unmodified CNCs from the AFM phase images. The unmodified CNCs achieved a well-dispersed particle state compared to the LD and MD grafting density. This can be attributed to the strong hydrogen bonding interactions between the hydroxyl groups on the cellulose and carbonyl groups on the PMMA, suggesting that thermodynamic interactions can be carefully controlled without modifying the surface chemistry upon consideration of filler-polymer interactions.

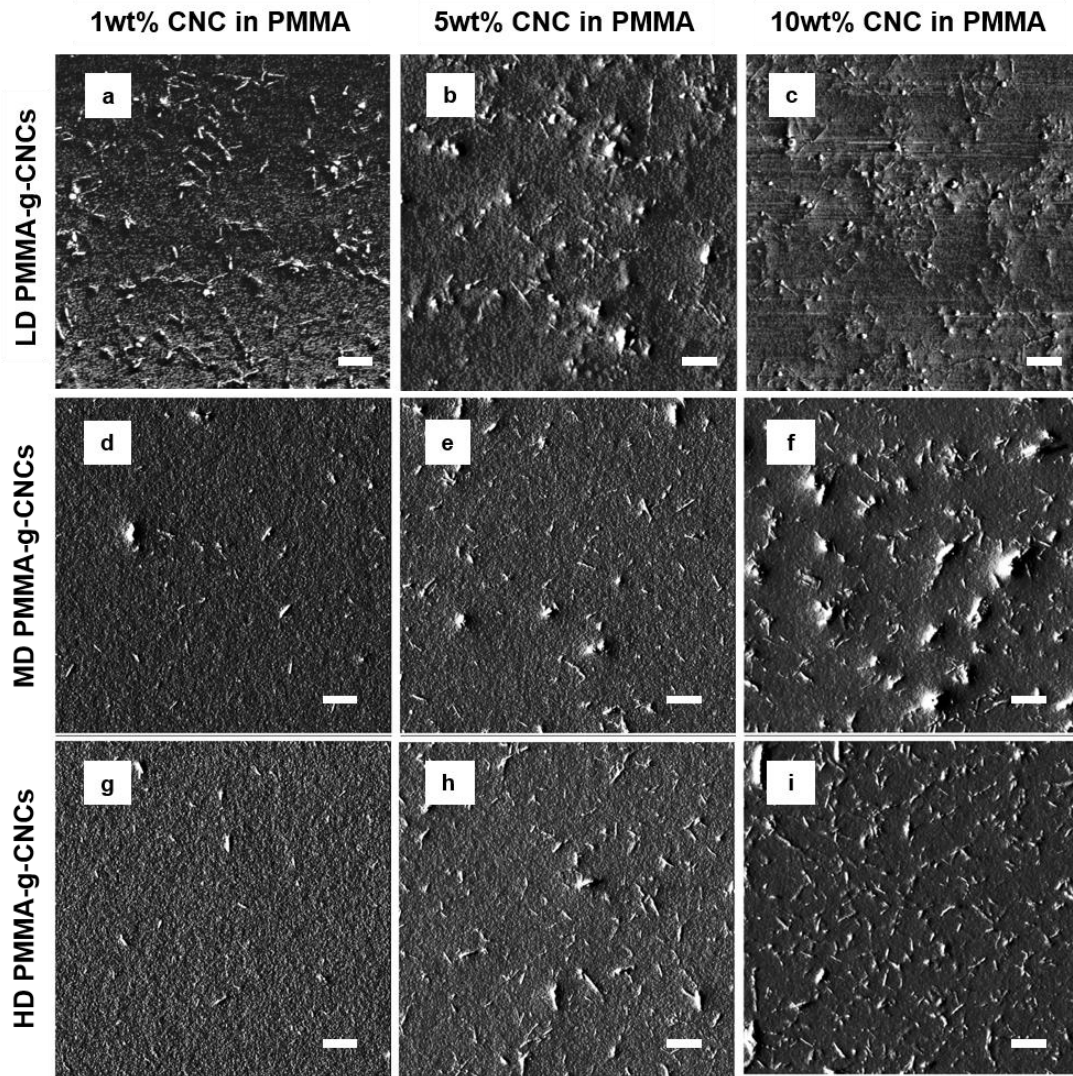


Figure 3.14. AFM phase images of PMMA-grafted-CNCs in a PMMA matrix as a function of grafting density and nanorod concentration.

Similarly, as with the unmodified CNCs, the PMMA-grafted-CNCs were dispersed in PS-*b*-PMMA ($M_w = 37$ kg/mol) to investigate the equilibrium morphology upon addition of nanorods. The co-assembly of cellulosic nanofillers in a symmetric diblock copolymer was studied as a function of nanorod concentration and grafting density. From the previous GISAXS studies, annealing the neat PS-*b*-PMMA thin film (without nanoparticles)

induced a lamellar morphology oriented parallel to the substrate in an asymmetric wetting configuration. This can be ascribed to the preferential interaction and affinity of the PMMA block to wet the native oxide layer on the silicon substrate, as well as the lower surface energy of polystyrene which drives the PS block to the air interface. In the case of asymmetric wetting, islands or holes can form on the film surface if the initial BCP film thickness is incommensurate with quantized film thickness $(n + 1/2)L_0$ where n is an integer and L_0 is the lamellar domain spacing. Therefore, such island and hole structure formation on the free surface can serve as an indication for parallel lamellae. To examine the nanostructure of the annealed BCP thin films with MD PMMA-grafted-CNCs, the surface topography was characterized with AFM. The AFM height images are summarized in Figure 3.15 with nanorod concentration varying from a) 1 wt%, b) 10 wt%, and c) 20 wt% MD PMMA-g-CNCs in PS-b-PMMA.

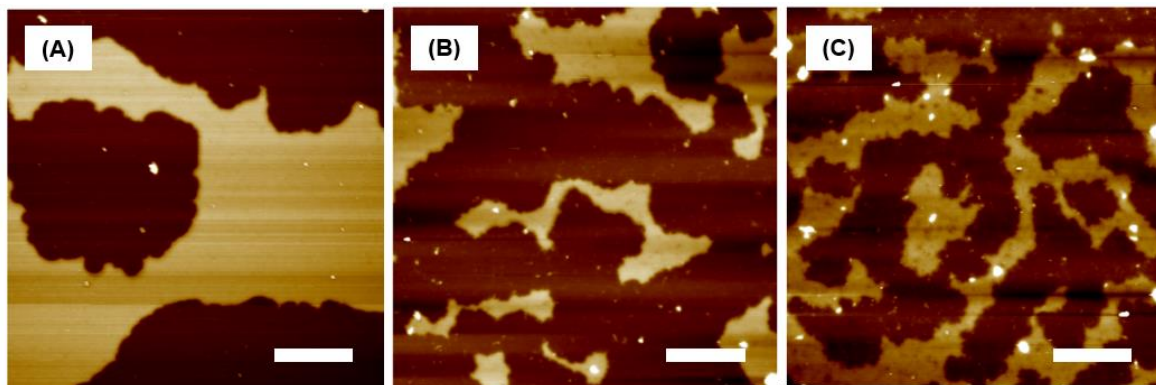


Figure 3.15. AFM height images of MD PMMA-g-CNCs in BCP of a) 1wt%, b) 10wt%, and c) 20wt% MD PMMA-g-CNCs in PS-b-PMMA. Scale bar represents 10 μ m.

For each nanocomposite thin film sample, island and hole formation on the film surface was observed after thermal annealing which is represented by the AFM micrographs in Figure 3.15. The structures observed in Figure 3.15a-c arise from incommensurate film thickness but also suggest the presence of residual solvent in the film during annealing. This can be ascribed to the thin film fabrication and processing conditions where films were cast on silicon substrates with a heating stage (65°C) to facilitate solvent evaporation and generate uniform films. However due to the high boiling point of DMF (153°C), a small amount of residual solvent likely remained trapped within the film.

Thermal annealing above the glass transition temperature of both PS and PMMA segments at 180°C gives sufficient mobility to the chains to microphase separate into lamellar microdomains oriented parallel to the free surface. Yet while enhanced chain mobility rapidly promotes microphase separation, the slow evaporation of DMF simultaneously induces a slight change in the total film thickness. Complete solvent evaporation eventually leads to a small reduction in the BCP thickness which potentially imposes a lateral strain on the lamellae. The step height of the surface layer can be adjusted to the lamellar period, however to accommodate for the total reduced layer thickness, localized hole defects are introduced to alleviate the strained lamellae.

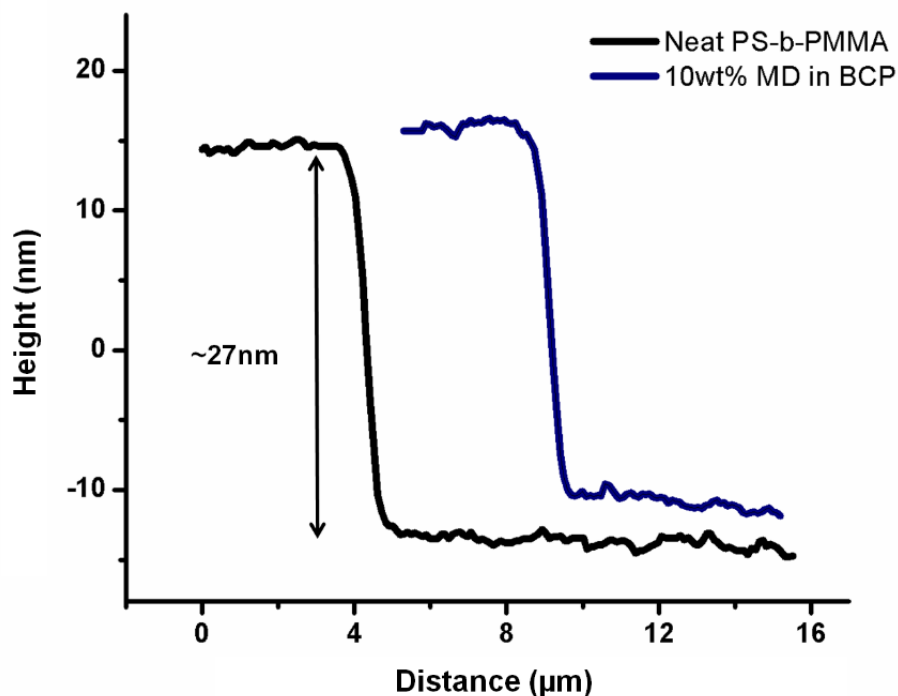


Figure 3.16. Height profile corresponding to linecuts across the AFM micrographs (holes) which reflect a step height of L_0 .

The step height can be extracted from the AFM images by obtaining a height profile for each sample. The BCP system (without nanofillers) used in this study has a measured step height of 27 nm, corresponding to the L_0 . The height profiles indicate that the equilibrium lamellar spacing was sustained (remains unchanged) at approximately 27 nm even with 10 wt% CNCs. Upon addition of PMMA-g-CNCs (MD), the film morphology on the surface suggest the parallel lamellae morphology was maintained up to 20 wt%, despite the high nanofiller content.

The internal nanostructure of the annealed block copolymer nanocomposite thin film was further investigated through neutron reflectivity measurements which were performed at the NG-7 Beamline at NIST Center for Neutron Research (NCNR). Neutron

reflectometry measurements were performed using a horizontal neutron reflectometer where the neutron scattering density was probed in a direction perpendicular to the free surface as a function of depth, or film height (z). In this study, a partially deuterated symmetric diblock copolymer *i.e.* dPS-b-PMMA with total molecular weight 37.6 kg/mol was used to generate sufficient contrast. Neutron scattering contrast was introduced into the BCP by selective labeling of a block with deuterium (d) as a means of altering the scattering lengths that give rise to scattering. The calculated scattering length density (SLD) for dPS and hPMMA is approximately 6×10^{-6} and 1.04×10^{-6} , respectively.

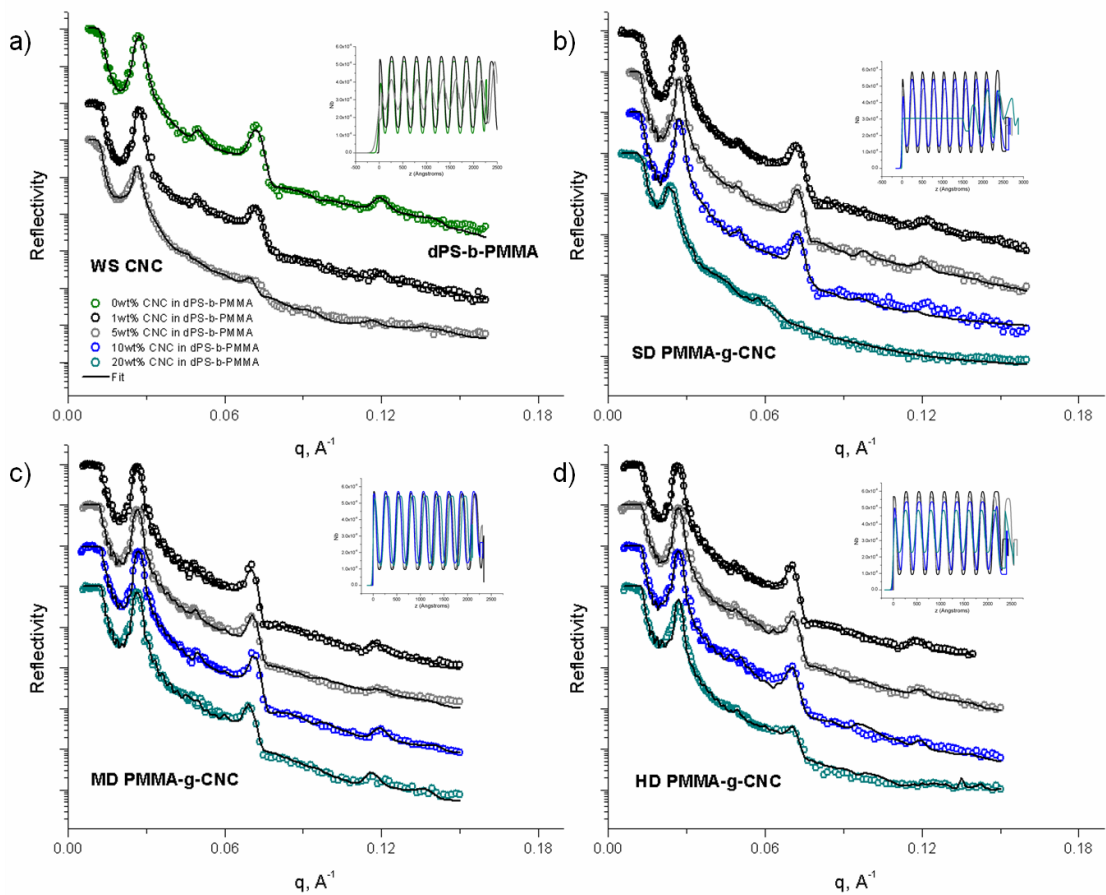


Figure 3.17. Neutron reflectivity profiles of annealed dPS-b-PMMA thin films with the addition of a) unmodified CNCs, and PMMA-grafted-CNCs of b) low grafting density

(LD), c) medium grafting density (MD), and d) high grafting density (HD) as a function of varying nanorod concentration at 1 wt%, 5 wt%, 10 wt%, and 20 wt% CNCs. The raw data is represented by the circles and solid lines corresponds to the fit. SLD profiles are shown as insets.

Thin films of dPS-b-PMMA were cast onto silicon substrates, which were exposed to ultraviolet ozone (UVO) prior to flow coating. For these studies, the total film thickness was measured with interferometry and remained fixed at approximately 8Lo. The film thickness (t) was confirmed from the Kiessig fringes in the reflectivity profiles and the relation $t = \pi/\Delta k_{z,0}$ where k is the neutron momentum normal to the free surface. The as-cast BCP thin film was subjected to thermal annealing above the glass transition temperature at 180°C for 24 hours to reach its equilibrium morphology. The reflectivity profile of the annealed dPS-b-PMMA thin film (without nanofillers) is displayed in Figure 3.17a. The collected raw data is represented by circular symbols whereas the solid line represents the calculated reflectivity profile (fit). The inset denotes the scattering length density (SLD) profile as a function of film depth where $z = 0$ is the polymer-air interface. Four orders of Bragg reflections were observed at $q_z = 0.027 \text{ \AA}^{-1}$, 0.049 \AA^{-1} , 0.072 \AA^{-1} , and 0.12 \AA^{-1} which arises from a multi-layered structure where lamellar microdomains are oriented parallel to the substrate. In agreement with earlier X-ray scattering studies, the favorable interactions with the native oxide layer cause PMMA to preferentially wet the silicon oxide substrate and the lower surface tension drives dPS to be preferentially located at the polymer-air interface.

To investigate the co-assembly of cellulosic nanofillers and block copolymer, neutron reflectivity measurements were studied as a function of nanofiller concentration

for both unmodified CNCs and poly(methyl methacrylate)-grafted-CNCs of varying grafting density. In addition to the neat BCP thin film, the unmodified CNCs in BCP served as control measurements to fully understand the enthalpic and entropic interactions. Similar to GISAXS measurements, the addition of 5 wt% unmodified CNCs resulted in a loss of intensity in Bragg peaks as observed in Figure 3.16a. This suggests that the incorporation of CNCs disrupts the BCP morphology where the lamellar microdomains are not completely parallel to the substrate. In the case of unmodified CNCs, higher nanofiller concentration (10 wt% and 20 wt%) led to complete macrophase separation where the sample could not be measured.

The neutron reflectivity data for the PMMA-grafted-CNCs with low (LD), medium (MD), and high (HD) grafting density are shown in Figure 3.17b, 3.17c, and 3.17d, respectively. The CNC loading was varied to find the optimal loading to maximize mechanical reinforcement without compromising on the BCP self-assembly and morphology. Addition of 1 wt% CNCs (black), 5 wt% CNCs (grey), 10 wt% (blue), and 20 wt% (teal) were dispersed into a dPS-b-PMMA thin film for each grafting density system and annealed above T_g as discussed previously. From the fitted data, SLD profiles were extracted, as shown in the insets.

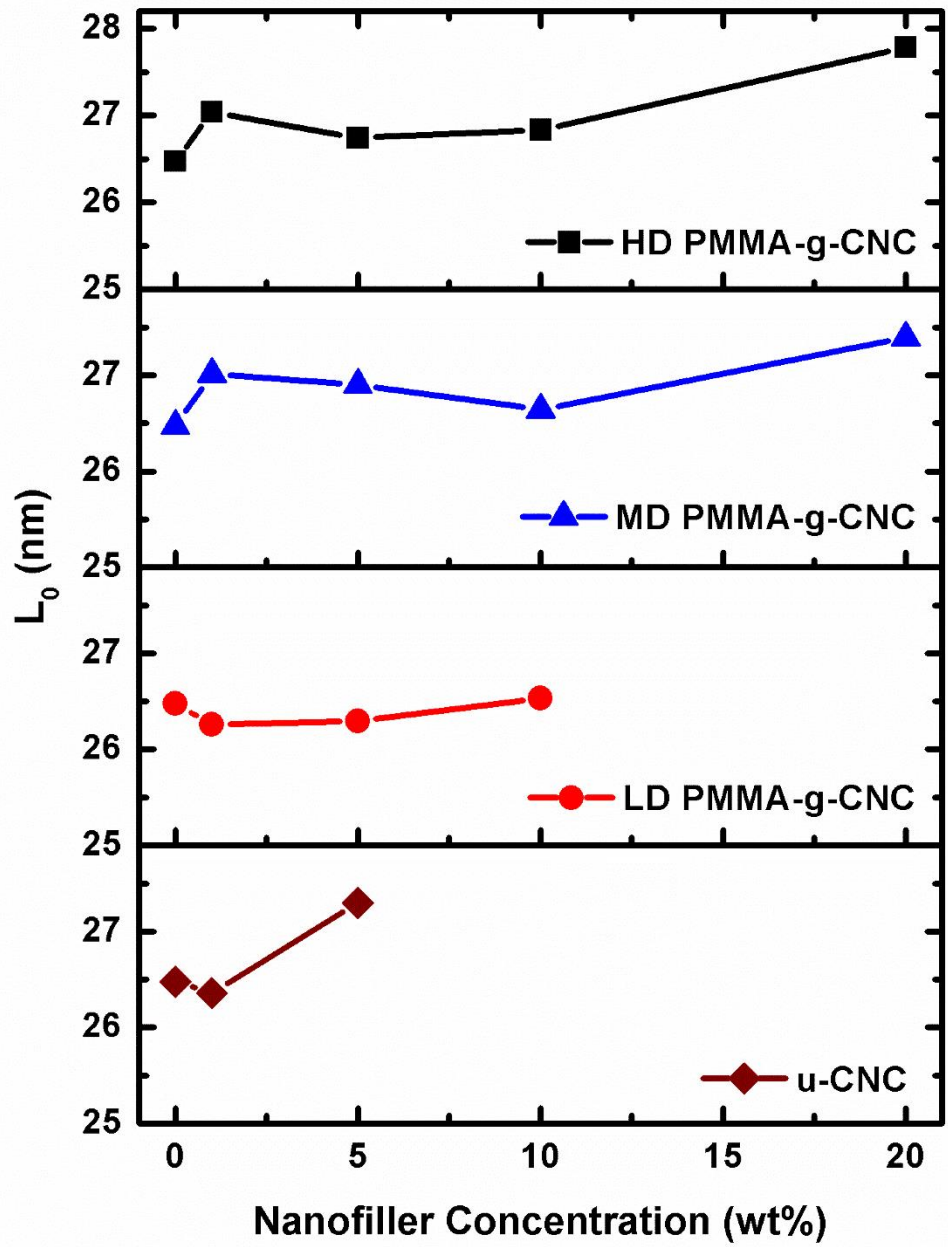


Figure 3.18. Domain size as a function of CNC nanofiller concentration for unmodified CNCs and PMMA-grafted-CNCs of low grafting density (LD), medium grafting density (MD), and high grafting density (HD).

Data acquisition and analysis gives further insight into the internal nanostructure and interfaces. The calculated domain sizes and interfacial widths were summarized in Figures 3.18 and 3.19 for each CNC type (unmodified and PMMA-g-CNCs of varying grafting density) as a function of nanorod concentration. The calculated domain spacing appeared to have a negligible change with increasing particle loading. The domain spacing, L_0 , was observed to remain constant at approximately 26.5 nm even up to 20 wt% CNC loading suggesting minimal swelling of domains and overall film. Rather, a random, isotropic distribution of cellulose nanocrystals within the block copolymer thin film is proposed to be able to accommodate for the large number of cellulose nanocrystals which then contributes to localized swelling. This is contrary to previous findings with highly grafted nanoparticles in block copolymer which reported nanoparticle distribution within a selective domain thereby resulting in swelling of the selective domain. As observed in Figure 3.17, the peak positions for each system were not shown to have any clear shifts in q_z , with the exception of 20 wt% LD, and extracted SLD profiles do not indicate a noticeable increase in peak width. A possible explanation could be resulted from an increase in the number of dPS and PMMA layers and will be examined in further detail.

The measured interfacial width for the neat BCP film was found to be sharp, approximately 50 Angstroms, which agrees with reported values from literature. The calculated interfacial width was observed to increase from 50 to 60 Angstroms for increasing CNC content from 0 to 20 wt%, respectively. However, despite the slight broadening, the interfacial width remained fairly sharp given the high nanofiller concentration.

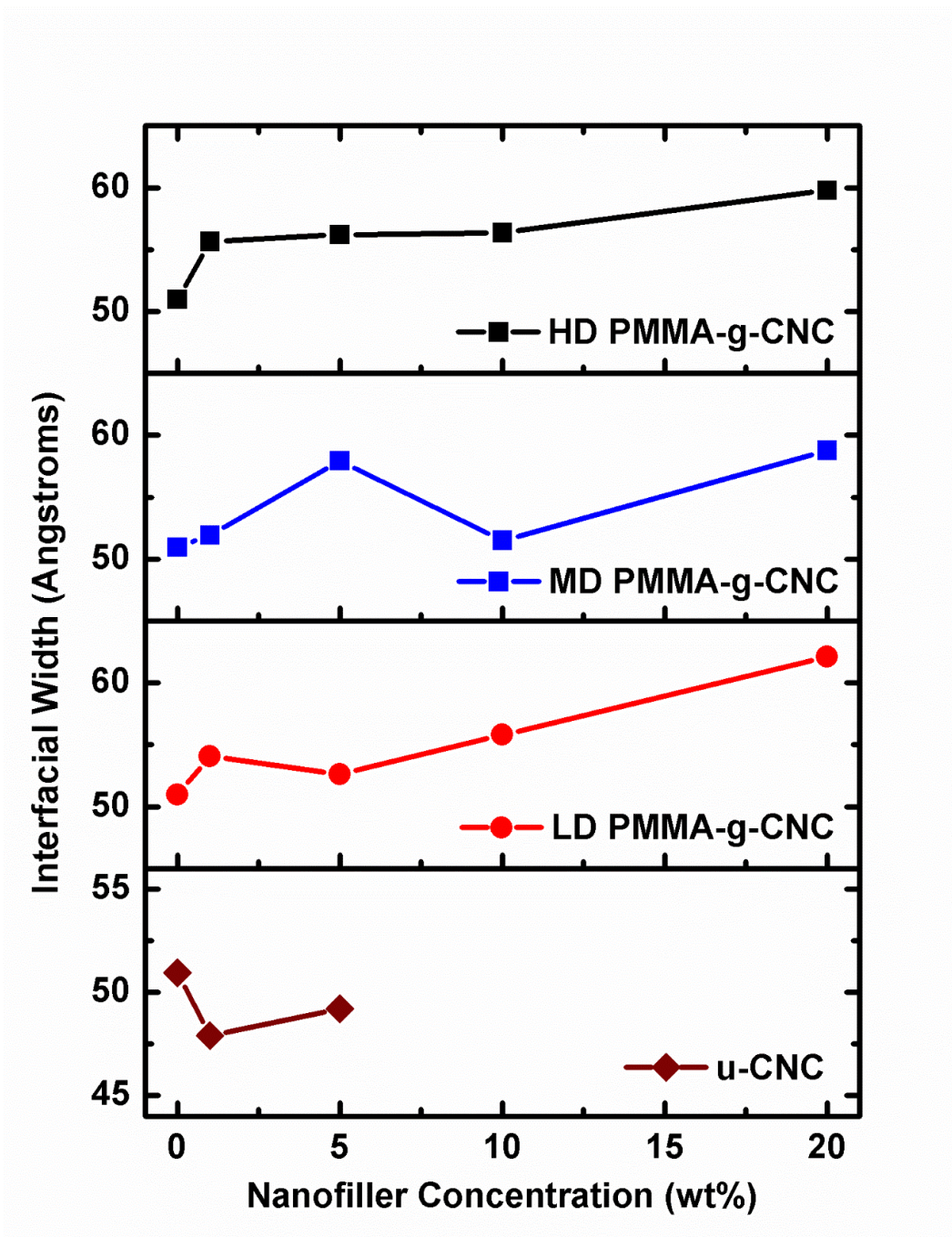


Figure 3.19. Measured interfacial width plotted as a function of CNC nanofiller concentration for unmodified CNCs (u-CNC) and PMMA-grafted-CNCs of low grafting density (LD), medium grafting density (MD), and high grafting density (HD).

Different nanoparticle loadings of MD PMMA-g-CNCs in dPS-b-PMMA varying from 1 to 20 wt% are displayed in Figure 3.17c. From the SLD profiles, information can be obtained regarding the spatial distribution of the nanorods throughout the bulk of the nanocomposite thin film. Upon increasing MD PMMA-g-CNC in BCP, the SLD was observed to systematically increase in hPMMA which indicated to the presence of cellulose nanocrystals. Due to the PMMA grafted chains on the CNC surface, a selective dispersion within PMMA was expected. However, an interesting observation was the simultaneous decrease of SLD in the dPS, suggesting an equal volume fraction of CNCs within dPS as well as hPMMA.

To put in perspective, average CNC dimensions have a length and width of 135 nm and 5.9 nm, respectively while each dPS layer is approximately 13 nm and each PMMA layer is 13 nm ($L_0 = 26.5\text{nm}$). As such, due to the bulky nature of CNCs with respect to domain size ($L_{NR} \sim 10 L_0/2$), CNCs are potentially traversed and partition into the PS domain to accommodate for such a high nanofiller concentration. The portion of the nanorod penetrating into the PS domain would undoubtedly result in an enthalpic penalty due to the unfavorable PS/CNC interaction. However, for each region of the PMMA-grafted-CNC exposed to PS chains, there is an equal surface area that has a strong interaction with PMMA resulting in an enthalpic gain. From previous experimental studies, spherical nanoparticles have been shown to segregate to either a selective block copolymer domain or align along the interface depending on factors such as particle size, nanofiller concentration, and thermodynamic interactions. Controlled NP orientation and alignment within microphase separated BCPs could be achieved due to the aforementioned nanoconfinement effect and chain stretching penalty. However, in our case, the particle

size greatly exceeds each layer thickness (approximately 10x the width of PMMA) and as such, the particle mobility is limited. The CNCs are believed to be in a kinetically trapped orientation state where it is energetically unfavorable to rotate or reorient. This decreased particle translational entropy leads to the nanorods traversed in both PS and PMMA domains (multiple interfacial contacts) to achieve the lowest energy state where the system can still undergo DSA around the incorporated NPs and maintain the lamellar morphology.

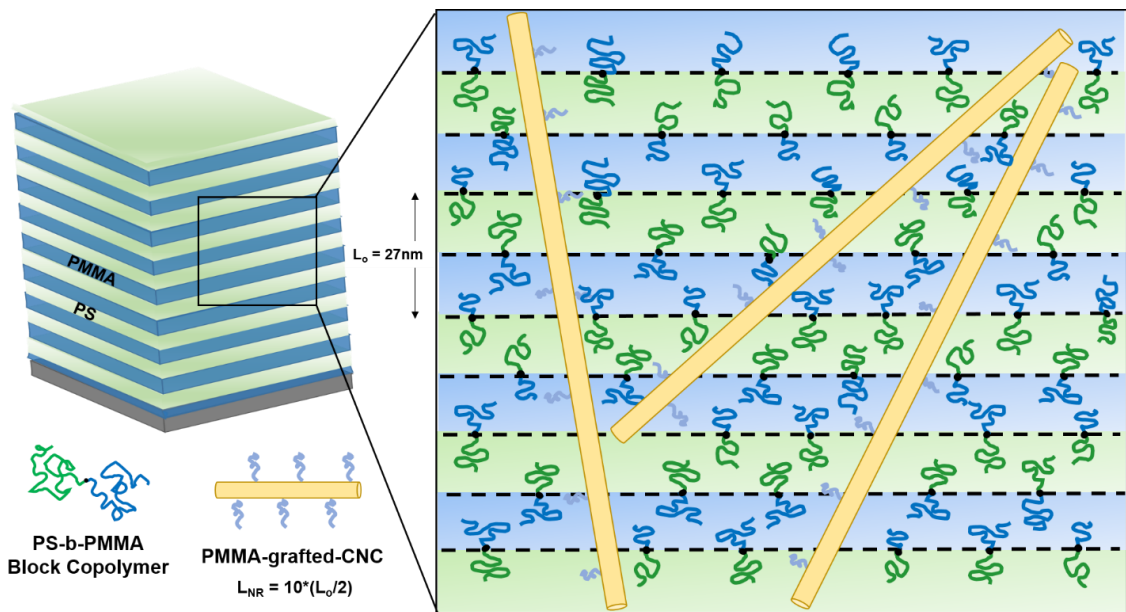


Figure 3.20. A possible representation of a random orientation of PMMA-grafted-CNCs in annealed diblock copolymer thin films which is unaffected by domain swelling or increased layer thickness.

Notably, an interesting observation was the deep fringes up to high q_z observed for both the MD and HD PMMA-g-CNC/BCP systems shown in the reflectivity profiles in Figure 3.17c and 3.17d. These film thickness oscillations, known as Kiessig fringes, are shown for the CNCs with higher grafting densities which indicate that the film is in fact smooth with low roughness despite the high loading of nanorods. The pronounced fringes observed for the annealed CNC/BCP thin films imply less interdiffusion within the film.

In addition to out-of-plane confinement *via* self-assembled block copolymers, the spatial distribution of cellulose nanocrystals was manipulated in-plane through a soft lithography approach known as capillary force lithography (CFL). Capillary force lithography provides an efficient patterning route to generate structures at the microscale and nanoscale over large areas.¹³⁹⁻¹⁴¹ The system is mainly comprised of an elastomeric mold placed directly on a substrate-supported polymer film. When a polymer film under patterned confinement is heated above the glass transition temperature of the polymer, capillary forces drive the polymeric melt into the mold cavity, or rather the void space between the mold and polymer. The mold is removed after cooling to room temperature which results in the negative replica of the patterned mold. The geometric size dimensions of structured surfaces are dependent on the features of the mold and subsequent pattern fidelity can be improved by optimizing the processing conditions.

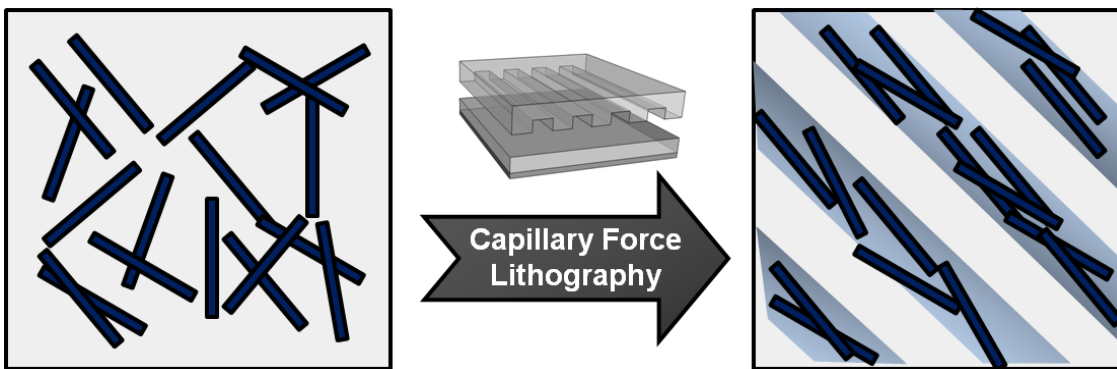


Figure 3.21. Schematic of a soft lithography strategy to generate well-ordered arrays of cellulose nanocrystals through patterned in-plane confinement.

The capillary force lithography approach shown in Figure 3.21 was applied to the polymer nanocomposite system comprised of 1 wt% LD PMMA-grafted-CNCs in poly(methyl methacrylate) homopolymer where the thickness of the film was approximately 90 nm. The mold used as a lithography master for pattern transfer was prepared by pouring poly(dimethylsiloxane) directly onto the polycarbonate mold surface of a commercially available compact disk and placed in the vacuum oven at 120°C for 2 hours to allow for PDMS curing *via* a crosslinking reaction. The pattern dimensions of the elastomeric poly(dimethylsiloxane) mold have a pitch and amplitude of 1.5 μm and 120 nm, respectively. The elastomer mold was placed directly on the surface of the polymer film and thermal annealed above the glass transition temperature of PMMA at 140°C for varying polymer molecular weights and different annealing times to account for the mold filling process. Upon cooling to ambient temperature, the elastomer molds are removed and the surface topography analyzed *via* atomic force microscopy.

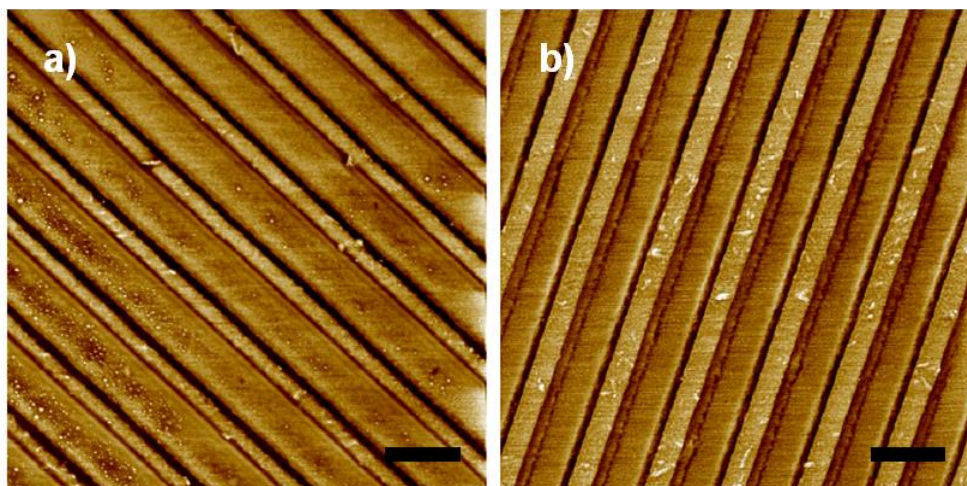


Figure 3.22. AFM phase micrographs of 1 wt% PMMA-grafted-CNCs in PMMA homopolymer with average molecular weight of 3 kg/mol after thermal annealing at 140°C for A) 10 min and b) 16 hrs. Scale bar is 2 μm .

AFM micrographs in Figure 3.22 display phase imaging of the annealed 1 wt% PMMA-grafted-CNCs (LD) in a PMMA homopolymer matrix of average molecular weight at 3 kg/mol. After 10 min of thermal annealing, periodic line channels are observed which denotes successful pattern transfer with short term annealing. The PMMA-grafted CNCs appear to be localized in the channel trenches and randomly oriented. However, CNCs could additionally be located in the upper regions of the patterned structures but cannot be resolved due to limitations of AFM imaging which are restricted to surface characterization. Increasing the annealing time to 16 hours resulted in a higher number of cellulose nanocrystals with preferential localization in the trenches, or lower regions of the patterned structures.

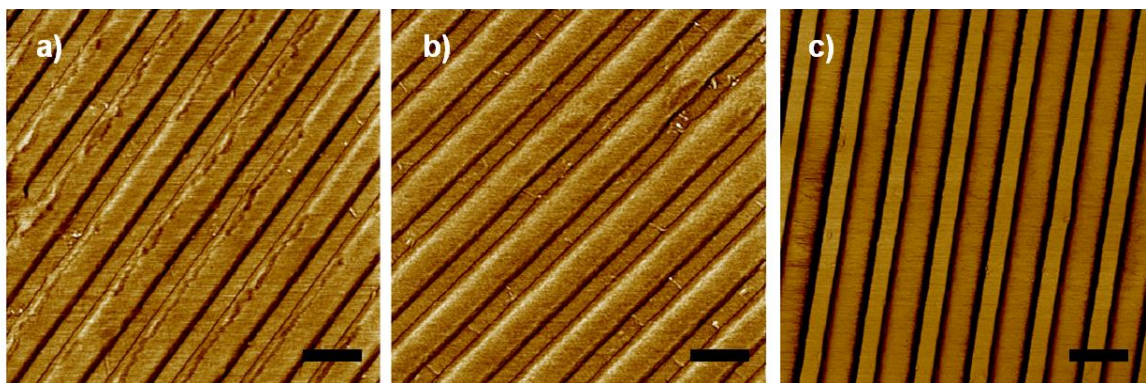


Figure 3.23. AFM phase micrographs of 1 wt% PMMA-grafted-CNCs in PMMA homopolymer with average molecular weight of 30 kg/mol. A) 10 min, b) 4 h and c) 16 h. Scale bar is 2 μm .

The molecular weight of the host polymer matrix (PMMA) was further increased from 3 kg/mol to 30 kg/mol and studied for varying annealing times at 140°C for 10 min, 4 h, and 16 h to manipulate nanoparticle distribution due to entropic confinement effects. Figure 3.23a notably exhibits non-uniformity of the patterned structures which is likely attributed to the short annealing time for pattern transfer. The cellulose nanocrystals were not visible on the surface or confined in the thin regions of the imprinted thin films at 16 h, however, a possible explanation is the segregation of PMMA-grafted-CNCs in the mesa regions which could be embedded in the polymer matrix. The nanorod distribution and alignment within channels can further be controlled by varying the size dimensions of the individual CNC relative to the geometric pattern confinement such as the lateral and step height dimensions. Further studies will be necessary to gain a fundamental understanding on how anisotropic CNC alignment and segregation can occur in well-defined arrays under patterned confinement.

3.4 Conclusion

In this work, we demonstrate a technique to control the dispersion and spatial distribution of cellulose nanocrystals in polymer thin films *via* tailored interparticle and particle-polymer interactions. The dispersion state and spatial distribution (organization) of rod-like nanocellulose in a polymer matrix can strongly influence the inherent macroscopic properties of the composite material. A model symmetric diblock copolymer poly(styrene-*b*-methyl methacrylate) was used to act as an ideal nanostructured template to selectively sequester and organize CNCs. The morphology evolution with the addition of nanoparticles was investigated through X-ray scattering and neutron reflectivity techniques. Polymer grafted nanoparticles were utilized to alter interactions between the polymer free chains and brush as a function of grafting density. To map out regimes of good dispersion, network formation, and aggregation states, the PNC films were studied as a function of nanofiller concentration covering a range above and below the reported percolation threshold. This study can provide insight into how the self-organization of nanorods drives the spatial distribution of cellulosic nanofillers which can further be adapted to optimize and/or tune a composite material's optical transparency or mechanical integrity.

CHAPTER IV

NANOPARTICLE-INDUCED STABILIZATION AND WETTABILITY OF
POLYMER THIN FILMS

4.1 Introduction

The stability of polymer thin films on solid substrates is of significant technological importance in applications ranging from adhesives to microelectronics and coatings where maintaining a homogeneous, defect-free film of uniform thickness is critical to its functionality, performance, and effectiveness.¹⁴²⁻¹⁴⁵ However, films at the nanoscale are susceptible to film rupture via dewetting,^{1,2,33,34} where initially smooth films break up through the formation of holes that continue to grow laterally. Hole coalescence leads to polygonal network arrays that eventually break into droplets due to Rayleigh instability. To address this undesired materials response, it is critical to develop an understanding of the inhibition of dewetting mechanisms in nanoscale thin films.

Barnes et al.¹⁴⁶ developed a novel strategy to achieve kinetic stabilization with the introduction of C₆₀ fullerene nanoparticles in polystyrene and polybutadiene thin films. While the inclusion of particles in a thin film can facilitate or enhance film rupture, the nanoscale feature of the particles was shown to inhibit dewetting due to segregation of the

nanoparticles to the substrate surface. A critical nanofiller concentration was demonstrated to suppress dewetting from nanoparticle surface coverage where hole growth is pinned and the inherent change in interfacial properties and surface energy is attributed to the surface roughness. Mackay et al.¹⁴⁷ demonstrated a similar inhibition effect with the addition of dendrimers for polystyrene thin film stabilization which was also ascribed to the dendrimer wetting layer at the substrate-polymer interface. Furthermore, Luo and Gersappe¹⁴⁸ employed molecular dynamics simulations of nanofillers in polymer to demonstrate the underlying molecular mechanisms governing thin film stability. In addition to previous findings (ie. the ‘pinning effect’), the role of polymer-particle interactions, nanoparticle mobility, and nanofiller size also contribute to local viscosity changes to control dewetting. Moreover, the influence of nanofiller concentration and surface energy on dewetting suppression and film morphology was examined based on the migration of nanoparticles due to relative interfacial energies between components.¹⁴⁹ This inhibition effect was further illustrated with the addition of C₆₀ fullerenes in multi-component systems where NP partitioning to the polymer interface and spatial distribution is exploited in phase separating polymer blends.¹⁵⁰ Similarly, various other studies have been shown to influence dewetting dynamics and/or dewetting inhibition through the addition of POSS nanoparticles^{151,152}, metal nanoparticles,^{153,154} and single-walled carbon nanotubes²¹ or by varying molecular architecture.^{155,156} Bilayers of polystyrene and PMMA with a graphene oxide monolayer acting as a compatibilizer and multiwalled carbon nanotubes (MWCNTs) exhibiting entangled networks have also been demonstrated to promote film stabilization.^{157,158}

In this work, we investigate the stability of polymer thin films on flexible, non-wetting substrates upon thermal annealing. The development of new strategies to stabilize thin films against external stimuli and tailor wettability without substrate modification has significant scientific importance in emerging technology and flexible electronics. The influence of polymer additives on the dewetting mechanism of polymer thin films is investigated, in particular, the effect of nanoparticle shape anisotropy and attractive particle-polymer interactions on film stabilization. To this end, we devised a novel approach to control the morphological evolution of polymer thin film dewetting behavior with the addition of anisotropic nanoparticles (*i.e.* cellulose nanocrystals (CNCs)) in poly(methyl methacrylate) (PMMA) as a function of nanofiller concentration. Cellulose nanocrystals are model 1D rod-like nanoparticles with nanoscale dimensions and unique properties advantageous for polymer reinforcement with characteristics such as high crystallinity, high modulus, high aspect ratio, low density, and low coefficient of thermal expansion.^{132,159} In this work, thin film stabilization is achieved on non-wetting and low surface energy flexible substrates by the presence of cellulosic nanorods at a critical nanoparticle concentration. The hydrophobic surface of PDMS was employed to act as a non-attractive substrate for the unmodified CNCs to investigate the strong affinity of CNCs with the polymer matrix. Furthermore, the directed self-assembly of a symmetric diblock copolymer *i.e.* poly(styrene block methyl methacrylate) (PS-*b*-PMMA) filled with CNCs is used as a model system where the subsequent film morphology is heavily influenced by surface energetics of BCP components relative to PDMS. The co-assembly and self-organization of cellulose nanocrystals and block copolymer phases provides a route to gain a fundamental understanding on how 2D confinement of nanorods in selective layers of

ordered lamellar block copolymer scaffolds affects thin film instabilities. These findings exploit the tunable wettability of nanocomposite thin films on a broadened array of unmodified substrates (flexible or rigid) which have significant ramifications for advanced materials development.

4.2 Experimental Section

Materials: Poly(styrene), poly(methyl methacrylate), and poly(styrene-*b*-methyl methacrylate) were purchased from Polymer Source Inc. and used as received. The average molecular weight and polydispersity index of PS, PMMA, and PS-*b*-PMMA are 21.8 kg/mol and 1.04, 15 kg/mol and 1.09, 37.6 kg/mol and 1.06, respectively. The glass transition temperature of the PS block was reported to be 104°C and the PMMA block was reported to be 128°C. N,N-Dimethylformamide (DMF) (ACS reagent, ≥99.8%) was purchased from Fisher Scientific and used as received. Single-side polished silicon wafers were purchased from University Wafer with (100) orientation and thickness of 625 μm.

Fabrication of Nanocomposite Thin Films: Solutions of PS, PMMA, and PS-*b*-PMMA were individually prepared by mixing each polymer in DMF, resulting in a total polymer concentration of 10wt%. Each polymer solution was placed on the Vortex for 12 hours to ensure complete mixing and filtered using a 0.2 μm PTFE filter. Dilute cellulose nanocrystal suspensions (1 mg/ml) of unmodified and PMMA-grafted-CNCs were prepared with DMF and sonicated before addition to the polymer solution. Nanofiller concentration in PMMA and PS-*b*-PMMA was varied from 0.5 to 10 wt% which refers to the mass of cellulose to that of polymer. Solutions of CNC/polymer/DMF were placed in a VWR B2500A-MTH sonicator for 4 hours to ensure good dispersion. Nanocomposite

thin films were prepared on silicon wafers via a flow coating technique which is described in detail elsewhere. The silicon wafers were exposed to 1 hour of UVO and the flow coating speeding was adjusted accordingly to achieve a film thickness of 100 nm. Due to the high boiling point of DMF, a heating stage was used during the film casting process to facilitate solvent evaporation. The film thickness was measured using Filmetrics UV-20 interferometer software.

Preparation of PDMS substrate: Poly(dimethyl siloxane) (PDMS) was prepared by using a Sylgard 182 kit purchased from Dow Corning. The ratio of crosslinking agent to elastomer base was 10:1 and the solution consisting of crosslinking agent and elastomer base was thoroughly mixed and placed in a desiccator to remove any trapped air bubbles for 30 minutes. The solution was then poured onto a cleaned glass plate (smooth surface) and placed in a vacuum oven to allow for curing at 120°C for 2 hours. The cross-linked PDMS is removed from the oven and quenched to room temperature. PDMS is prepared by cutting into strips with average dimensions of 75 mm x 25 mm x 1 mm.

Nanocomposite Film Transfer via Water Immersion Technique: The nanocomposite thin films on silicon substrates were transferred to a PDMS elastomer strip through a water flotation technique. Films were first cast onto silicon oxide substrates via flow coating and film thickness was measured through interferometry. The edges of the substrate-supported polymer film were scored to allow for ease of thin film release (lift-off) from the silicon substrate. Films were transferred by adhering the substrate-supported polymer film to the smooth PDMS surface and submerged in water where the polymer is eventually delaminated from silicon. Upon complete transfer to PDMS, the polymer/PDMS system is

removed from water and placed in a desiccator to remove residual water and allow for film drying. The transferred nanocomposite thin films were annealed above the glass transition temperature at 180°C over a 24 hour period under vacuum to impart sufficient mobility to the polymer chains.

Characterization: The film morphology was characterized using an Olympus BX41 optical microscope. Detailed image analysis was carried out on each micrograph using ImageJ software to first threshold the image to determine the net area fraction of polymer, number density of domains, and hole size distribution.

4.3 Results and Discussion

To understand the influence of nanoparticle incorporation on film stability, control measurements were first performed on a thin film of PMMA (average molecular weight 15 kg/mol) without the addition of nanoparticles. The film stability was first examined by casting a neat PMMA thin film on a native oxide layer on the surface of a silicon wafer from UV-ozone exposure. For these studies, the film thickness remained fixed at 100 nm. The as-cast film appeared uniform immediately after flow coating and heated well above the glass transition temperature at 180°C over a 24 hour period. Figure 4.1 displays the optical micrographs of the neat PMMA thin film on SiO_x after annealing. The polymer film remained homogeneous and smooth on the spatial scale obtained with optical measurements. This is likely attributed to the strong affinity and favorable interactions between the polymer and substrate. The increased polar interactions and hydroxyl groups on the surface results in hydrogen bonding between the PMMA and SiO₂. Interestingly, the substrate effect appears prominent even when decreasing the film thickness to 40 nm.

The ultrathin polymer film (40 nm) was subjected to identical annealing conditions as the 100 nm film on SiO₂. At the given time scale, the polymer film remained smooth and uniform at the spatial scale under investigation. This stabilization trend was even observed for ultrathin films (40nm) with low molecular weight polymethylmethacrylate which has a reported molecular weight of 3 kg/mol.

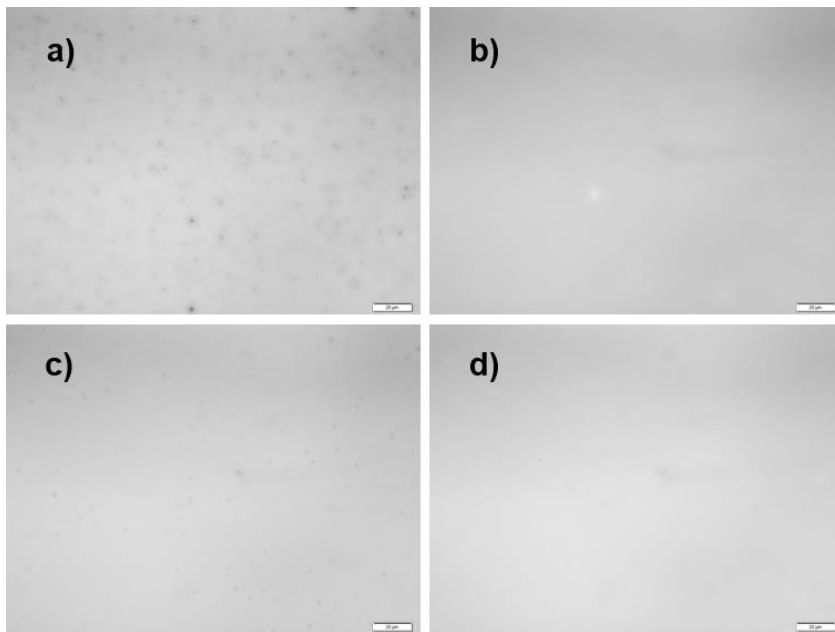


Figure 4.1 Optical micrographs of neat PMMA annealed on SiO_x of molecular weight 3 kg/mol for film thickness of a) 40 nm and b) 100 nm and PMMA molecular weight 15 kg/mol for film thickness of c) 40 nm and d) 100 nm. Films annealed at 180°C over a 24 hour period under vacuum. Scale bar is 20μm.

The stability of polymer thin films was further investigated on non-wetting substrates where films were inherently unstable leading to film rupture. For this study, an elastomer such as poly(dimethyl siloxane) was used as a non-wetting surface having an ultralow surface energy and also sought to transition from rigid, hard substrates (*i.e.* SiO_x) to flexible substrates. The development of new strategies to stabilize thin films against

external stimuli and tailor wettability without modification of the substrate surface has significant technological importance in a broad array of applications. Due to the non-wetting nature of PMMA on PDMS, polymer thin films were transferred to the elastomeric substrate as illustrated in Figure 4.2. Films having a thickness of 100 nm were first cast onto silicon substrates with a thin native oxide layer (SiO_x) *via* a flow coating technique and measured with interferometry. Films were adhered to the PDMS surface, allowing for conformal contact between the polymer and elastomer, and then transferred through a water flotation technique. Transferred films were removed from the water and placed in a desiccator to remove any residual water. Upon complete drying, films were annealed well above the glass transition temperature at 180°C under vacuum for 24 hours. The film morphology was examined prior to annealing to confirm initially uniform films and after thermal processing to determine equilibrium dewet structures.

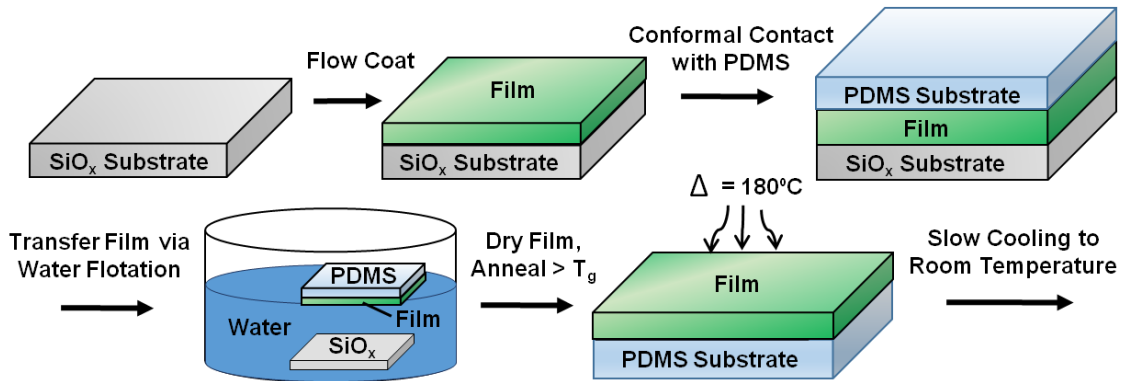


Figure 4.2 Schematic of experimental approach. Thin films are first cast onto silicon substrates *via* a flow coating technique and transferred to PDMS through a water flotation approach. A desiccator is used to remove any residual water on the film. Upon drying,

films are placed in a vacuum oven at 180°C for 24 hours and microscopy is used to determine equilibrium dewet morphology.

To determine the influence of nanoparticle incorporation on film stability, control measurements were performed on homopolymer thin films of PMMA (average molecular weight 15,000 g/mol) annealed on PDMS substrates. Prior to annealing, the transferred film appeared homogeneous, uniform, and defect-free *via* microscopy as shown in Figure 4.3a. The final morphology of the annealed PMMA thin film (film thickness 100 nm) on PDMS is shown in Figure 4.3b. The optical micrographs displayed fully dewet morphology with droplet formation arranged in polygonal arrays (Voronoi pattern). The typical late-stage dewetting behavior can be attributed to the spreading parameter wherein $S < 0$, arising from the large difference in surface tension between PMMA and PDMS where $\gamma_{PMMA} = 41.1 \text{ mJ/m}^2$ and $\gamma_{PDMS} = 19.8 \text{ mJ/m}^2$. This results in a conventional late-stage dewetting pattern to minimize unfavorable interactions between the polymer film and elastomer substrate, achieving a minimum free energy state.

Neat PMMA

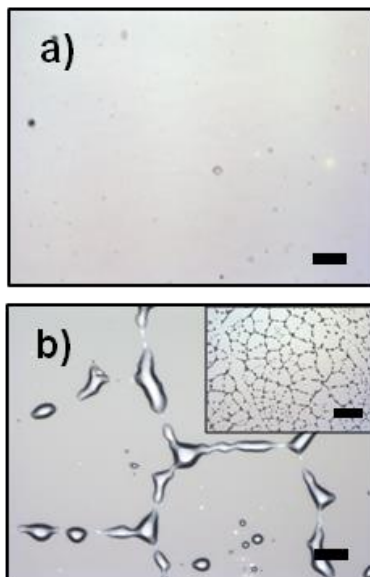


Figure 4.3 Optical micrograph of poly(methyl methacrylate) on PDMS substrate a) before thermal annealing and b) after thermal annealing at 180°C for 24 hours. Scale bar represents 20 μm and higher magnification inset has a scale bar of 100 μm .

To investigate the stability of polymer thin films on a non-wetting flexible substrate, anisotropic nanofillers were introduced into the polymer matrix to gain insight into how nanoparticles can influence film morphology and dewetting dynamics. As such, a range of nanoparticle concentrations were studied varying from 0 to 10 mass% addition to PMMA (molecular weight 15 kg/mol) to determine the effect of nanofiller concentration on film stability. The final morphology was characterized through microscopy as shown in Figure 4 with the addition of a) 0 mass% (neat PMMA), b) 1 mass% unmodified CNCs, c) 2 mass% unmodified CNCs, and d) 5 mass% unmodified CNCs in PMMA. In contrast to the annealed neat PMMA thin film which displays completely dewetted structures, the

addition of 1 mass% unmodified CNCs results in a significant change in the droplet size and number density of domains formed interpreted as a reduced state of dewetting. There is an increase in the number of droplets per unit area, as well as a narrower distribution in the droplet size possibly due to nucleated dewetting by the nanoparticles. For higher nanofiller concentrations at 2 mass%, uniform films are maintained after thermal annealing, as shown in Figure 4.4c. At 5 mass% CNC, the films showed internal aggregation of some kind, but the films are nevertheless stabilized against dewetting (Figure 4.4d). Thus, the addition of cellulose nanocrystals above a threshold concentration leads to complete inhibition of early stages of dewetting that initiate with hole formation. The film stabilization observed with the presence of 2 mass% unmodified CNCs suggests that there exists a critical nanoparticle concentration threshold ($1 \text{ mass\%} < \phi_c < 2 \text{ mass\%}$) to completely suppress thin film dewetting on the time scale of our measurements. This can be ascribed to the strong affinity of the nanorods with the polymer matrix where the abundance of hydroxyl groups on the CNC surface preferentially interact with the ester functional groups (COOCH_3) of the PMMA, which promotes the dispersion of CNCs in PMMA. Hydrogen bonding interactions between the hydroxyl groups on the cellulose nanocrystal surface and carbonyl groups on PMMA likely restrict the motion of polymer segments, contributing to kinetic stabilization and dewetting inhibition.¹⁶⁰ The incorporation of cellulose nanocrystals in PMMA and subsequent hydrogen bonding interactions were in agreement with other studies which have shown a significant effect on thermomechanical properties.^{25,161}

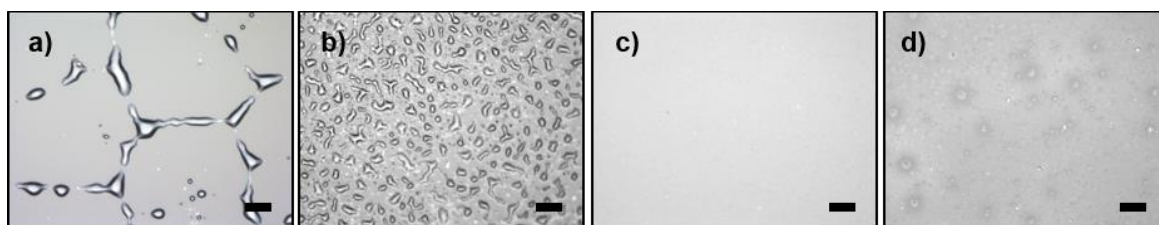


Figure 4.4 Optical micrographs of annealed thin films of a) PMMA, b) PMMA with 1 wt% unmodified CNCs, c) PMMA with 2 wt% unmodified CNCs, and d) PMMA with 5 wt% unmodified CNCs. Films (of film thickness 100nm) are annealed at 180°C for 24 hours. Scale bar represents 20 μm .

Film stabilization with the presence of cellulose nanocrystals was further investigated to determine if there was a similar trend with modified CNCs of similar dimensions. While unmodified CNCs were observed to maintain good dispersion in PMMA due to strong hydrogen bonding interactions, modification of the CNC surface chemistry was sought to understand the underlying molecular interactions which govern film stability against dewetting. PMMA-grafted-CNCs were synthesized via atom transfer radical polymerization (ATRP) with a grafting density of 0.33 chains/nm². The PMMA-grafted-CNCs had a reported M_n of 19.7 kg/mol and M_w of 22.9 kg/mol, resulting in a PDI of 1.16. Similarly with unmodified CNCs, a range of nanofiller concentration varying from 0wt% to wt% PMMA-grafted-CNCs was employed in this study. The morphology of the nanocomposite thin films on PDMS was examined via optical microscopy after annealing at 180°C for 24 hours. Figure 4.5 displays the representative optical micrographs of 100 nm thin films of PMMA (M_w 15 kg/mol) with a) 0wt% (neat system), b) 1wt% PMMA-grafted-CNCs, c) 2.5wt% PMMA-grafted-CNCs, d) 5wt% PMMA-grafted-CNCs, and e) 10wt% PMMA-grafted-CNCs. While the thermodynamic interactions of the examined systems are altered by grafting PMMA chains onto the CNC surface, the nanocomposite

thin film systems appear to show a similar trend in regards to polymer surface coverage with increasing cellulose concentration. Film rupture is observed with the presence of low nanofiller concentration of PMMA-grafted-CNCs in a chemically similar polymer matrix (PMMA), however, the droplet formation shows a significant change in the number and size of droplets with increasing CNC content as compared to the annealed neat PMMA thin film. Complete dewetting inhibition and film stabilization was achieved at the critical nanorod concentration on our given time scale and spatial resolution.

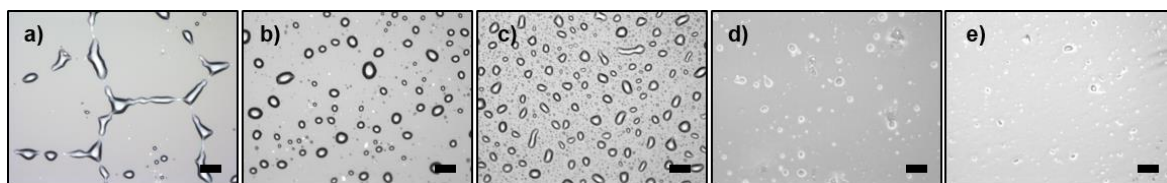


Figure 4.5 Optical micrographs of annealed thin films of a) PMMA, b) PMMA with 1wt% HD PMMA-grafted-CNCs, c) PMMA with 2wt% HD PMMA-grafted-CNCs, and d) PMMA with 5wt% HD PMMA-grafted-CNCs. Films (of film thickness 100nm) are annealed at 180°C for 24 hours. Scale bar represents 20 μm .

The net area fraction (polymer surface coverage) of the nanocomposite thin films after thermal annealing is further compared for the two different types of CNCs: unmodified CNCs and PMMA-grafted-CNCs ($\sigma = 0.33 \text{ chains}/\text{nm}^2$) in polymethylmethacrylate (molecular weight 15 kg/mol). This comparison is studied as a function of nanofiller concentration varying from 0 to 10wt% as illustrated in Figure 4.6. The surface chemistry modification was investigated to determine the role of molecular interactions on dewetting phenomenon and gain insight into how particle dispersion governed by entropy and enthalpy influences thin film stability.

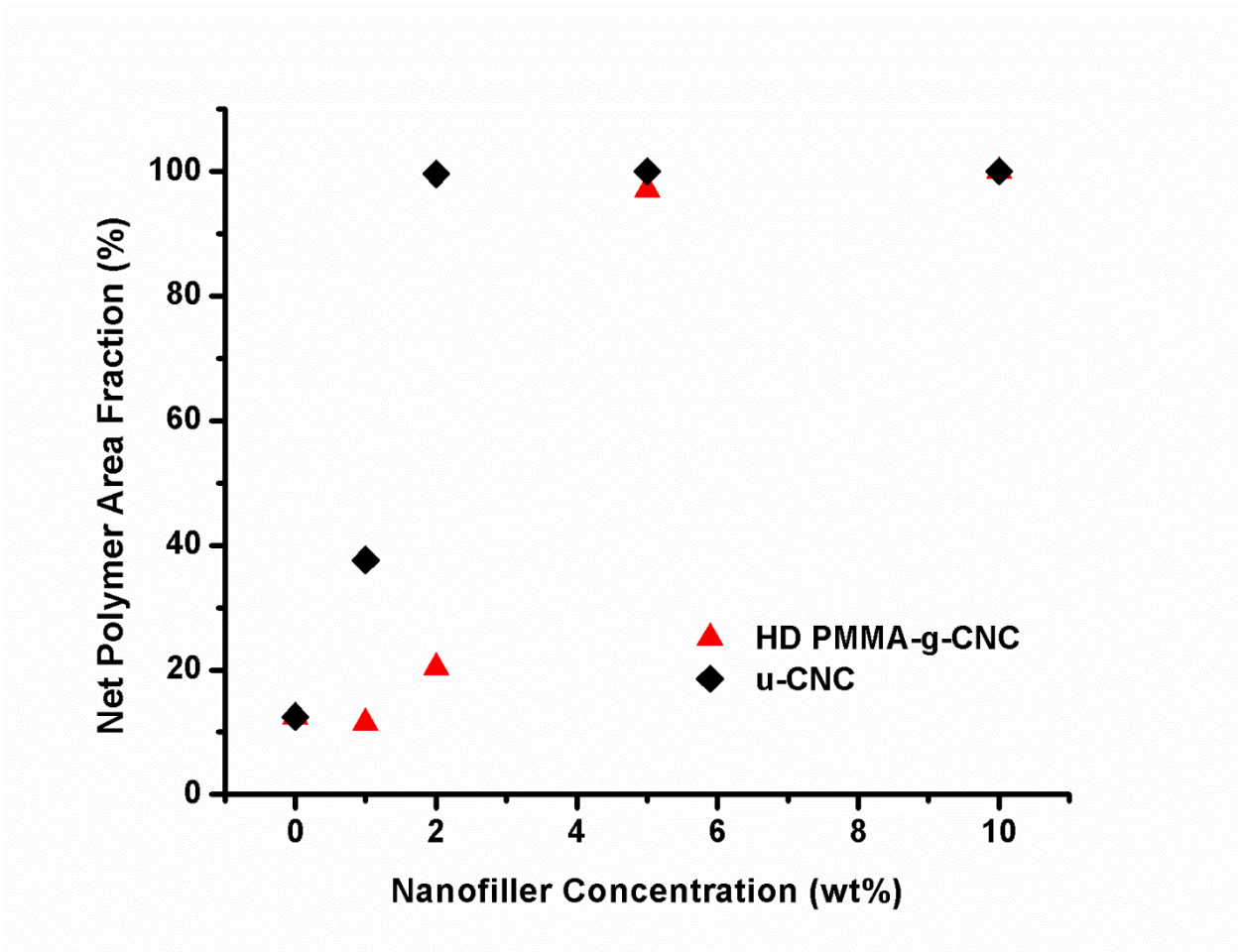


Figure 4.6 Net polymer area fraction as a function of nanofiller concentration for unmodified CNCs (u-CNC) and HD PMMA-grafted-CNCs in poly(methyl methacrylate) homopolymer of molecular weight 15 kg/mol.

While the thermodynamic interactions of the examined systems are altered by grafting PMMA chains onto the CNC surface, the nanocomposite thin film systems appear to show a similar trend in regards to polymer surface coverage with increasing cellulose concentration. The neat polymer thin film without nanoparticles completely dewets upon annealing. However, as discussed, the addition of 2wt% unmodified CNCs or 5wt%

PMMA-grafted-CNCs in a PMMA thin film induces film stability on completely non-wettable surfaces. The ability to tune thin film wettability (and stability) on its underlying solid substrate has significant importance in technological applications ranging from coatings, adhesives, and dielectric layers. Notably, we can transition past rigid substrates (SiO_x) towards flexible substrates that have a low surface energy.

The molecular mass of the polymer system was varied from 15 kg mol⁻¹ to 30 kg mol⁻¹ to examine the molecular weight effects on dewetting kinetics in the presence of anisotropic nanoparticles. Figure 4.7 displays the net polymer area fraction as a function of nanofiller concentration for each PMMA system after annealing. Here, the higher molecular mass (30 kg mol⁻¹) exhibits a similar trend for film stabilization in comparison to 15 kg mol⁻¹. The neat polymer thin film without nanoparticles forms dry patches which results in typical late-stage dewet structures upon annealing. While 0.5wt% CNCs in PMMA displays late-stage dewet structures, nearly 51% of the nanocomposite film remains defect-free at 1wt% CNCs in PMMA (30 kg mol⁻¹). This is in contrast to the addition of 1 wt% CNCs in the slightly lower molecular weight PMMA matrix where 37% of the film retains polymer surface coverage after annealing. Nevertheless, a critical nanorod concentration of 2 wt% CNCs is observed to induce film stability and suppress dewetting on our spatial resolution scale at a fixed 24 hour annealing period at 180°C. The increased molecular weight of the polymer will inherently have a higher viscosity which will likely exhibit slower dewetting dynamics and morphological evolution. However, the slight increase in polymer molecular mass used in this study appears to have a negligible effect on impeding dewetting kinetics, suggesting spontaneous film rupture is dominated

by unfavorable contact area between the polymer and substrate. Film stabilization achieved with the presence of anisotropic nanofillers can be attributed to the reduction of mesh size with incorporated CNCs and entanglement of the nanorod with the polymer matrix.

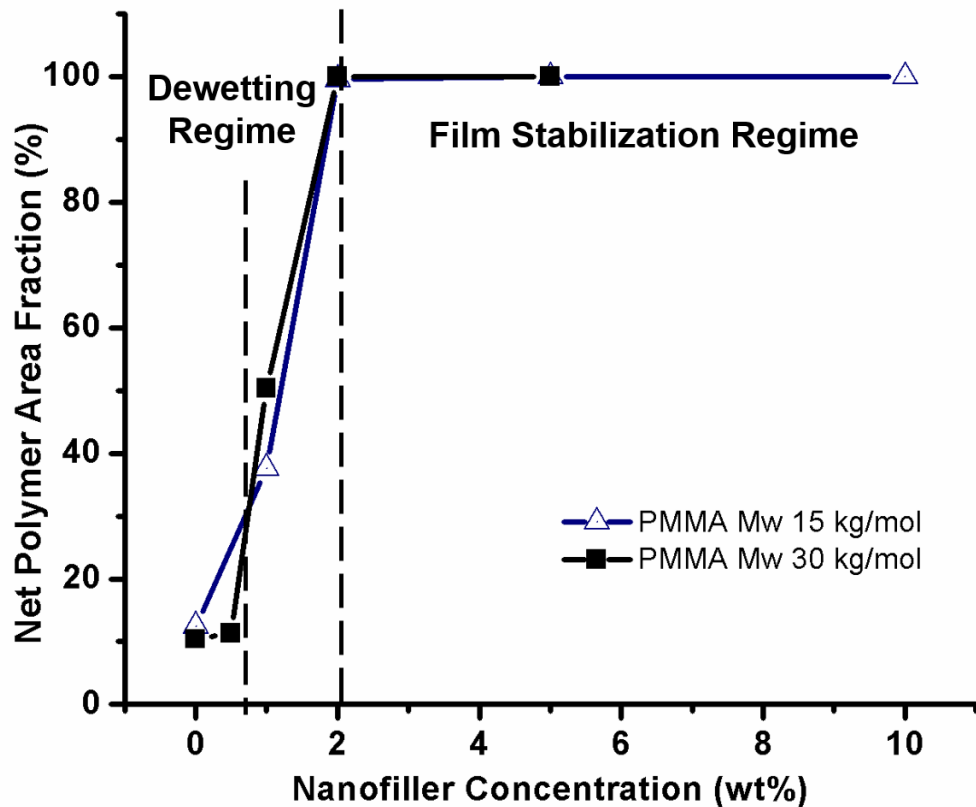


Figure 4.7 Net area fraction of polymer as a function of nanofiller concentration from 0 to 10wt% for unmodified CNCs in PMMA. The molecular weight of PMMA was varied from 15 kg mol⁻¹ (triangular symbols) to 30 kg mol⁻¹ (squares).

We investigate film morphology on completely non-wetting surfaces by examining the dewetting mechanism of a block copolymer (BCP) thin film. Block copolymers are known to self-assemble into well-defined, periodic arrays of nanoscale feature sizes (10 –

100 nm), and the morphology and orientation are highly sensitive to factors such as the substrate surface energy and wetting properties, annealing conditions, and film thickness.^{162,163} The addition of nanoparticles in self-assembled BCPs provides exciting opportunities towards next-generation functional nanomaterials whose overall properties can be tailored by controlling the spatial distribution and orientation of nanoparticles.^{105,118} More recently, these well-defined nanostructures are sought to be compatible with continuous materials nanomanufacturing on flexible substrates,^{164–166} however the low surface energy of the substrate surface or additional substrate modification requirements have imposed limitations on the applicability of this cost-effective approach. While chemical modification of the substrate has been explored as a means to control block copolymer domain orientation, strategies developed to maintain film stability and microstructure without altering the interactions between the substrate and block copolymer film have not been fully investigated. The film stability and ordering dynamics of a PS-*b*-PMMA thin film on a non-wettable surface *i.e.* poly(dimethyl siloxane) (PDMS) by the incorporation of cellulose nanocrystals was examined. In this regard, we investigated the co-assembly of cellulose nanocrystals and lamellar block copolymers on the macroscopic dewetting behavior, ordering dynamics, and film stabilization on PDMS without any required substrate modification.

To determine the wettability of BCP/CNC thin films on PDMS, control measurements were first carried out on neat poly(styrene-*block*-methyl methacrylate) (PS-*b*-PMMA) without nanoparticles. In this study, a model symmetric diblock copolymer *i.e.* poly(styrene-*block*-methyl methacrylate) (PS-*b*-PMMA) with average molecular weight of 37 kg mol⁻¹ was used. The BCP thin film was transferred to PDMS and the substrate-

supported BCP film was annealed well above its glass transition temperature to impart sufficient mobility to the block copolymer chains to enable microphase separation. Figure 4.8 displays the optical micrographs of neat PS-*b*-PMMA and neat homopolymer (PS and PMMA) with similar molecular weight of each BCP component. The BCP and homopolymer thin films exhibit late-stage dewetting after annealing at 180°C over a 24 hour period. The polymer films are unstable on the PDMS substrate which leads to film rupture to reduce the total free energy of the system by minimization of interfacial area between the substrate and polymer film. As a result of thin film stabilities, spontaneous formation of holes and subsequent film breakup into polygonal arrays of polymer droplets is observed.

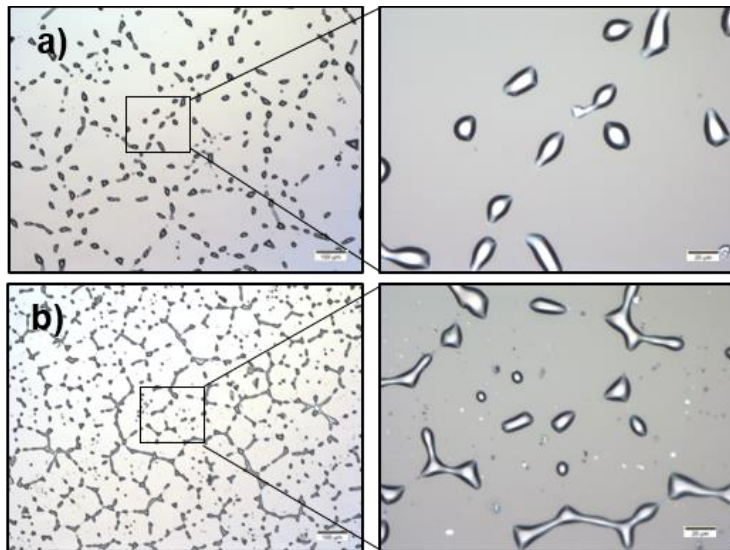


Figure 4.8 Optical micrographs of annealed a) poly(styrene) and b) PS-*b*-PMMA (average molecular weight 37 kg/mol) on PDMS. Scale bar represents 100 μm and higher magnification inset has a scale bar of 20 μm .

The film stabilization effect was further examined by the incorporation of unmodified cellulose nanocrystals in lamellar block copolymers. Figure 4.9 shows optical micrographs of annealed nanocomposite thin films from 0 to 5 mass% CNCs. In contrast to the completely dewetted structures of the neat BCP film, the presence of 1 wt% unmodified CNCs results in suppression of dewetting phenomenon. Similar dewetting inhibition is observed for increasing nanofiller concentration of 2wt% and 5wt% CNCs in PS-b-PMMA.

In addition to film stability with the addition of nanofillers, buckling of the polymer film surface is displayed via microscopy. The wrinkling of the film surface can be ascribed to the expansion and contraction of PDMS during annealing. The reported coefficient of thermal expansion for PS, PMMA, and PDMS are $\alpha_{PS} \approx 70 \times 10^{-6} \text{C}^{-1}$, $\alpha_{PMMA} \approx 50 \times 10^{-6} \text{C}^{-1}$, and $\alpha_{PDMS} \approx 325 \times 10^{-6} \text{C}^{-1}$, respectively. When heated above the glass transition temperature, the underlying substrate (PDMS) expands. However, upon cooling below the T_g to room temperature, the elastomeric substrate contracts, exerting a compressive stress. The slow quenching process of the nanocomposite film was taken to minimize any film cracking or deformations that might result from a rapid cooling rate, in particular with a system that has such a large difference in moduli between the film and substrate.

Neat PS-b-PMMA

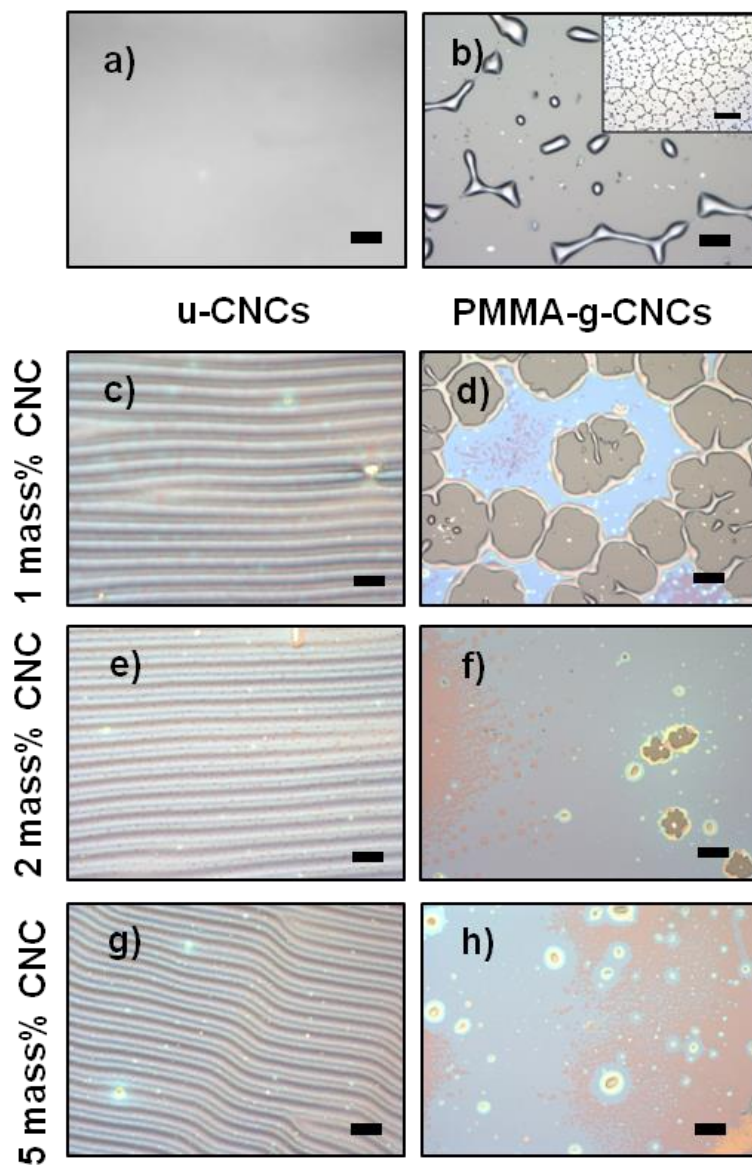


Figure 4.9 Optical micrographs of PS-b-PMMA a) after film transfer (prior to annealing), and b) annealed PS-b-PMMA (neat system) with c,d) 1 mass% CNCs, e,f) 2 mass% CNCs, g,h) 5 mass% CNCs, where c,e,g are unmodified CNCs (u-CNCs) and d,f,h are PMMA-grafted-CNCs. The PMMA-grafted-CNCs have a grafting density of 0.33 chains/nm². Scale bar represents 20 μm and the inset of 2b has a scale bar of 200 μm .

We next investigate the effect of internal nanostructure and morphology on film stabilization. Self-assembled BCPs have been demonstrated to selectively sequester and organize nanofillers where the spatial distribution and dispersion of CNCs can influence the inherent macroscopic properties of a thin film. To fully understand the interplay of thermodynamic interactions (interparticle and polymer-particle interactions) on film stability, PMMA-grafted-CNCs were studied in PS-*b*-PMMA. Figure 4.9d,f,h summarizes the annealed PS-*b*-PMMA thin films with addition of 1, 2, and 5 mass% PMMA-grafted-CNCs.

In contrast to the neat BCP which displays late-stage dewetting, the incorporation of 1wt% PMMA-grafted-CNCs shows intermediate dewetting behavior. While the low nanofiller concentration is unable to control thin film instabilities when annealed above T_g , significant retardation of dewetting kinetics is observed. The optical micrographs in Figures 4.9f and 4.9h display the formation of holes due to film rupture wherein the holes continue to grow in size, removing polymer matter to the edges which form a rim. Hole growth eventually leads to coalescence in which the contacting holes merge. A notable observation is the droplet formation occurring throughout the hole growth mechanism, which is characteristic of polymer thin films on low-wettability surfaces.³ In this case, a fingering instability of the rim is observed as a result of the increased velocity of hole growth which generates droplets during the hole growth process. The hole growth velocity (v) is proportional to the contact angle such that $v \propto \theta^3$. In contrast to high-wettability systems, a higher contact angle (lower wettability) exhibits faster hole growth and higher rim curvature where finger-like structures develop on the moving, unstable rims of the expanding hole. Due to the increased velocity of the moving rim, the fingers ultimately

detach from the retracting mass and generate droplets. As the nanoparticle concentration is increased to 2 mass% PMMA-grafted-CNCs in PS-b-PMMA, early-stage dewetting is observed with the formation of holes, however with 5 mass% and 10 mass% PMMA-grafted-CNCs, no appreciable dewetting is observed on our fixed time scale. It should be noted that the mass% in this study refers to the total weight of the CNCs (including grafted chains) with respect to the polymer. As such, 5 mass% PMMA-grafted-CNCs corresponds to a lower number average of individual particles in the polymer matrix when compared to the unmodified CNCs (approximately equal to 2wt% unmodified CNCs).

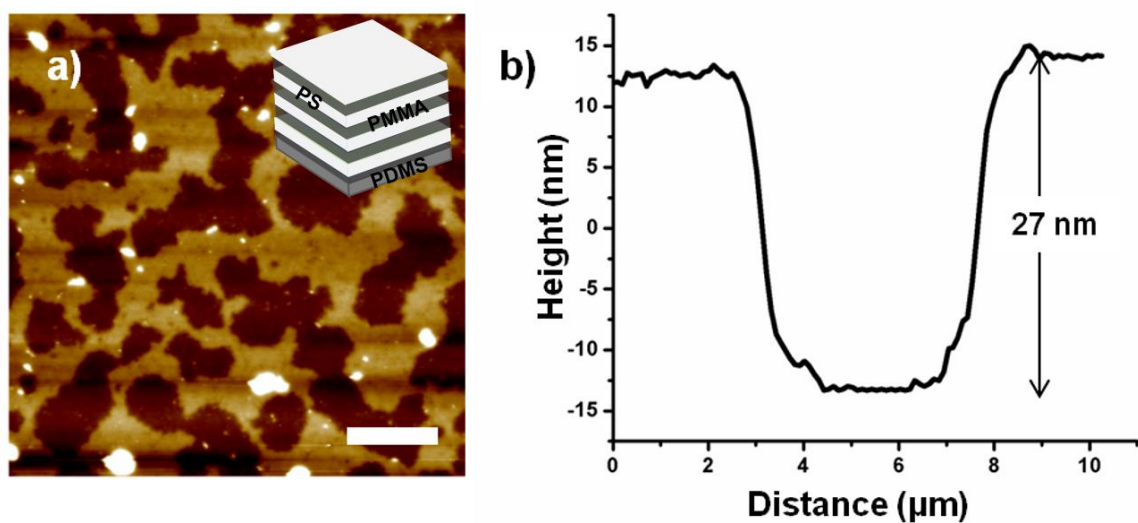


Figure 4.10 AFM height image of annealed PS-b-PMMA with a) 10wt% HD PMMA-grafted-CNCs and b) the corresponding line cut extracted from the height profile. Scale bar is 10 μ m.

In addition to maintaining smooth, uniform films upon thermal annealing above T_g , a particularly interesting observation is the lack of polymer film wrinkling typically initiated from the expansion and contraction of PDMS upon heating and cooling. This is in

contrast to the buckling observed in Figure 4.9c,e,g with the incorporation of unmodified CNCs in PS-b-PMMA, implying there exists a critical stress to induce film buckling. We believe this can be attributed to the film morphology and underlying thin film nanostructure that could potentially be contributing to in-plane reinforcement. The unmodified CNCs disrupt the directed self-assembly of BCPs to minimize the energetic penalty from unfavorable interactions and chain stretching due to accommodation of the high aspect ratio CNCs and particle aggregation. To put this geometric effect in perspective, the CNCs have an average length and width of 135-150 nm and 3-5nm, respectively whereas the lamellar periodicity, or domain spacing L_0 , is approximately 27 nm. In contrast to the unmodified CNCs, the presence of PMMA-grafted-CNCs in lamellar block copolymer thin films indicate well-ordered lamellar domains oriented parallel to the free surface, giving rise to a multi-layered structure when heated above its glass transition temperature T_g . The parallel lamellar morphology can be deduced from the island and hole formation displayed in Figure 4.10, where the sample thickness is incommensurate with the repeat spacing. This can be ascribed to the lower surface tension of polystyrene which drives PS to the polymer-air interface and propagates from the surface throughout the film.

4.4 Conclusion

In this work, we successfully demonstrated an effective strategy to tune the wettability and stabilization of nanoscale thin films on underlying traditionally non-wetting substrate by using polymer systems where the film morphology is sensitive to surface energies and interfacial tension. Neat PMMA thin films rupture and dewet after thermal annealing on non-wetting substrates with a low surface energy. Film stabilization and

dewetting inhibition is achieved with the incorporation of a critical nanofiller concentration of 2wt% cellulose nanocrystals in PMMA nanocomposite thin films due to the high affinity of CNCs with the polymer matrix. The incorporation of anisotropic nanoparticles in a polymer matrix with controlled attractive interactions (hydrogen bonding) has significant importance in technological applications ranging from coatings to adhesives to dielectric layers. In addition to suppressing dewetting, highly ordered lamellar structures are achieved without physical and/or chemical modification of the substrate surface which is typically required for controlled morphology or orientation. Multilayered nanostructures with the addition of cellulose nanocrystals on non-wetting surfaces via directed self-assembly is a simple yet robust strategy to fabricate highly ordered BCPs over large areas viable with roll-to-roll (R2R) nanomanufacturing and moreover, provides a universal route to transition from traditional rigid substrates towards high-throughput fabrication and development of flexible electronics.

CHAPTER V

MECHANICAL REINFORCEMENT OF SUB-MICRON POLYMER NANOCOMPOSITE FILMS VIA BUCKLING MECHANICS

5.1. Introduction

With the rising demand shifting towards fabrication of smaller devices, nanoscale films and coatings are of scientific importance in emerging technologies. Polymer thin films at the nanoscale have been demonstrated to exhibit unique physical properties that may deviate from their bulk counterparts.^{12,15,167} The mechanical strength and thermal stability of thin film systems, in particular, is critical in optimizing the device or material performance which can be subject to deformation or collapsed nanostructures over an extended period of time.¹⁶⁸ In this regard, insight on the mechanical robustness of a thin film system holds great significance to define the scope of its application. However, the mechanical properties cannot be acquired using conventional measurement methods such as tensile testing due to the geometric constraints and instrument limitations associated with substrate-supported films.

Recent studies have addressed the challenges regarding the mechanical integrity of ultrathin polymer films when confined to nanometer dimensions.^{74,76,169-171} For instance, molecular dynamics simulations indicated that there exists a critical thickness threshold (\approx

40 nm) below which point the elastic modulus begins to exhibit different behavior than observed with the bulk.¹⁶⁹ The existence of a small region near the free surface of the film was proposed to contribute to a surface layer of enhanced mobility at the polymer-air interface which results in the reduction of mechanical properties as compared to the bulk. The surface layer has a finite thickness on the order of a few nanometers wherein its contribution to the overall film properties depends on the surface layer thickness relative to the total film thickness. The effect becomes more pronounced with decreasing thickness, but the contribution is negligible for films above the critical thickness threshold and exhibits bulk property behavior. Similarly, attractive or non-attractive interactions between the substrate and film can result in a different property response due to changes in segmental mobility.⁷⁴

Strain-induced elastic buckling instability for mechanical measurements, or commonly referred to as SIEBIMM, provides an alternative approach to obtain direct measurements of the mechanical properties through a buckling-based metrology.^{74,75,172} This approach involves a rigid film transferred to a pre-stretched elastomeric substrate such as PDMS on a customized strain stage. When the system is subjected to a small uniaxial compressive strain, periodic buckling is generated on the film surface which results to minimize the strain energy in the system. The wavelength of the buckling pattern is related to modulus of film, modulus of substrate, Poisson's ratios and film thickness as shown in the relationship below:

$$\frac{E_f}{(1 - \nu_f^2)} = \frac{3E_s}{(1 - \nu_s^2)} \left(\frac{d}{2\pi h} \right)^3$$

where E is the modulus of the film (f) and substrate (s), ν is the Poisson ratio, d is the buckling wavelength, and h is the film thickness.

In this work, we demonstrate mechanical characterization of nanoscale thin films through a buckling mechanics approach to measure the elastic properties. The mechanical properties of sub-micron polymer nanocomposite films are investigated as a function of nanofiller concentration using multi-component systems comprised of anisotropic nanofillers such as cellulose nanocrystals and thermoplastics. The surface chemistry of the CNC is modified to control the interparticle and particle-polymer interactions that govern nanoparticle dispersion and correlated to the elastic properties of the system. Moreover, self-assembled block copolymers are utilized to further elucidate the effect of nanostructure and confinement on the mechanical response of polymeric materials.

5.2. Experimental Section

Materials: Poly(methyl methacrylate) (PMMA) and poly(styrene block methylmethacrylate) (PS-b-PMMA) were purchased from Polymer Source Inc. and used as received without further purification. The molecular weight of PMMA was 30 kg mol^{-1} with PDI of 1.15. The total molecular weight of PS-b-PMMA was 66 kg mol^{-1} with a PDI of 1.09. N,N-Dimethylformamide (DMF) (ACS reagent, $\geq 99.8\%$) was purchased from Fisher Scientific and used as received. Sodium Chloride (NaCl) windows were purchased from Edmund Optics and used as received without any modification.

Polymer nanocomposite solutions: A dilute 1 mg/ml cellulose nanocrystal suspension is first prepared by adding freeze-dried CNCs to dimethylformamide (DMF) solvent and placed in a sonicator bath for 1 hour. Polymer solutions of PMMA and PS-b-PMMA are separately made by dissolving in DMF to generate a 5 wt% polymer solution and placed on the Vortex for 6 hours to ensure mixing. The solutions are filtered using a 0.45 μm Nylon membrane filter to remove any impurities or contaminants. The filtered polymer solutions and CNC suspensions are added accordingly to produce CNC/PMMA and CNC/PS-b-PMMA solutions of varying cellulose nanocrystal concentrations above and below the reported percolation threshold at 0.5 wt%, 1 wt%, 2 wt%, 5 wt%, 10 wt%, and 20 wt% where wt% refers to the ratio of cellulose to polymer weight. The polymer nanocomposite solutions are placed in a sonicator bath to ensure good dispersion of CNCs.

Fabrication of Sub-micron Polymer Nanocomposite Thin Films: Silicon wafers are exposed to 30 min of ultraviolet-ozone (UV-ozone) to clean the surfaces prior to casting films. Films are cast onto the silicon substrates through a flowcoating technique by placing approximately 20 μl of polymer solution between the gap between the blade and silicon substrate. The modified flowcoating setup includes a heating stage on top of the translation stage where the substrate is located. The additional heat facilitates solvent evaporation due to the high boiling point of DMF (153°C) and prevents or minimizes solution backflow to generate films of uniform thickness. The flow coating conditions and parameters are optimized to obtain film thickness accordingly by altering the concentration of the polymer solution, or changing the speed or acceleration of the translation stage. It should be noted that for the annealed BCP thin films, sodium chloride (NaCl) windows were utilized as an

alternative substrate instead of silicon wafers. The films were cast directly onto the NaCl surface without any UV-ozone modification.

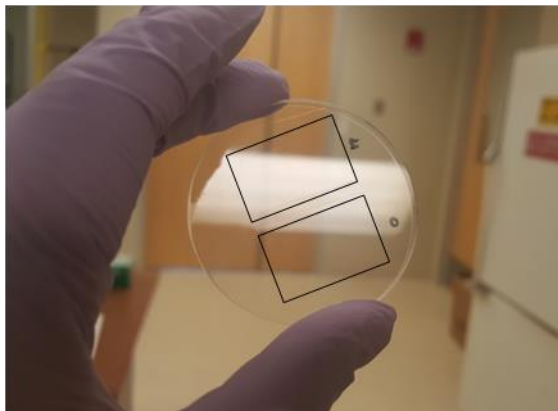


Figure 5.1 Sodium chloride (NaCl) window utilized as an alternative substrate for film transfer to different substrates. The rectangular sections denote the films cast directly on the surface *via* flowcoating.

Preparation of PDMS Substrate: Poly(dimethyl siloxane) was utilized as the elastomeric substrate in this study and prepared using a Sylgard 182 kit comprised of an elastomer base and crosslinking agent. A 20:1 ratio of elastomer base to curing agent was thoroughly mixed and placed in a desiccator to remove any trapped air bubbles. The solution mixture was then directly poured onto the smooth surface of a cleaned glass plate with careful attention to ensure uniform thickness throughout (mm) and placed in the vacuum oven at 120°C for 2 hours to allow for PDMS curing through a crosslinking reaction. Upon cooling to ambient temperature, the PDMS is cut into rectangular sections with typical dimensions of 75 mm x 25 mm.

Thin Film Characterization: The thickness of substrate-supported polymer films were measured for each sample using a FV-20 thin film interferometer. The film morphology was characterized using a BX41 optical microscope. ImageJ analysis was utilized for detailed image analysis of optical micrographs.

5.3. Results and Discussion

To provide nanomechanical characterization for the polymer film systems utilizing CNC as a reinforcing agent, we propose to measure the modulus using a buckling method known as strain-induced elastic buckling instability for mechanical measurements (SIEBIMM). Polymer thin films are first cast on UV-ozone exposed silicon substrates (*ie.* SiOx) *via* flowcoating technique. The edges of the film are scratched to assist in film lift-out and the surface of the substrate-supported film is placed onto a pre-stretched PDMS substrate on a customized stage to allow for conformal contact. The SiOx/thin film/PDMS system is subjected to a water bath *via* a floating technique. Once the film is transferred to PDMS, the silicon substrate will lift-off to allow for minimal destruction to the film. The film/PDMS system is then placed in a desiccator to allow for complete drying to ensure there is no residual water in contact with the film. When a compressive stress is applied to the system, the surface must buckle in order to accommodate for the large difference in moduli of the film and the substrate, which generates a periodic buckling pattern. This representation is displayed in Figure 5.2 for a polymer film of thickness h .

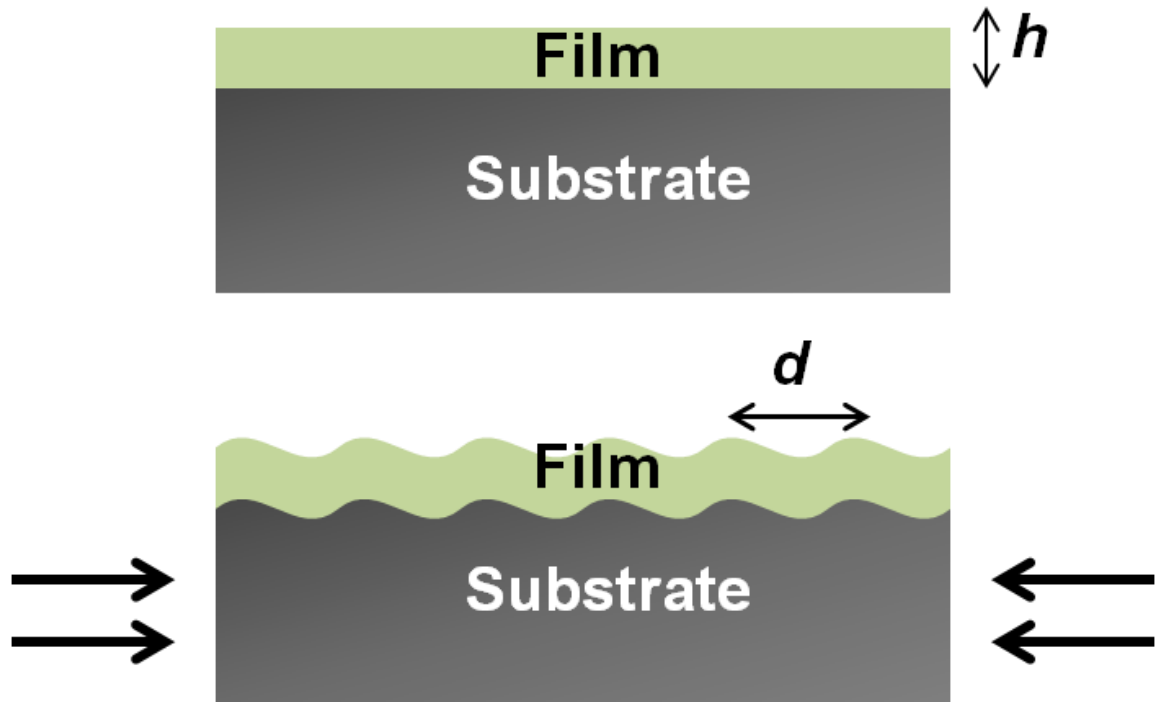


Figure 5.2 Schematic of buckling with a system comprised of a rigid polymer film of thickness h on a soft elastomer substrate. A small compressive strain applied to the system results in periodic buckling with wavelength d due to the large difference in moduli.

Two different types of cellulose nanocrystals were examined in a poly(methyl methacrylate) (PMMA) homopolymer matrix to determine the tailored interactions on CNC dispersion and the relationship to its reinforcing properties in thermoplastics. To obtain accurate modulus measurements, precaution was taken to ensure minimal deformities associated with film transfer such as cracking or film folding. The conformal contact between the PDMS and film proves advantageous in facile transfer of the film to the elastomeric substrate. This technique allows for water to penetrate between the film and silicon substrate wherein the film becomes delaminated from the silicon wafer without

any external force. The polymer nanocomposite film morphology was examined prior to buckling to ensure complete transfer of uniform, defect-free films using optical microscopy. Figure 5.3 represents the optical micrographs of a PMMA of molecular weight 30 kg/mol with up to 10 wt% CNCs incorporated within the homopolymer matrix. The optical micrographs display smooth, homogeneous films of uniform thickness with no apparent defects detected at the given spatial resolution scale.

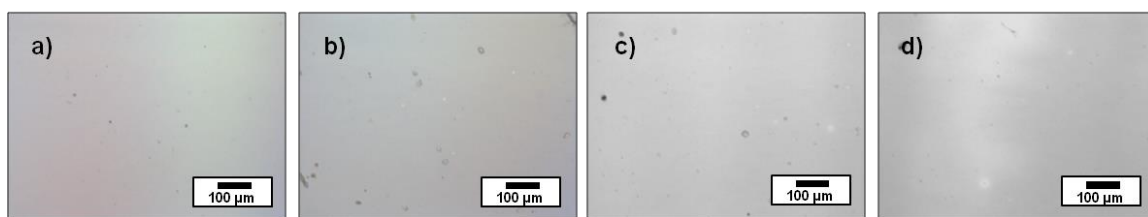


Figure 5.3 Optical micrographs of polymer nanocomposite system after floating films onto PDMS to confirm homogeneous films before applying compressive strain for systems containing varying concentrations of CNCs in PMMA at a) 0 wt% (neat PMMA), b) 1 wt% CNCs, c) 5 wt% CNCs, and d) 10 wt% CNCs.

To induce a buckling instability, a small compressive strain was applied to the film in a uniaxial direction. Figure 5.4 displays the representative optical micrographs for varying nanofiller concentrations including neat PMMA (without nanorods) of molecular weight 30 kg/mol, 1 wt% CNCs in PMMA, and 5 wt% CNCs in PMMA. The subsequent wrinkling of the film surface displayed in the micrographs can be attributed to an interplay between the energy required to bend the rigid film and its underlying elastomeric substrate. The buckling generated appears periodic and uniform for each CNC/PMMA system as

shown in Figure 5.4 which is indicative of the nanoparticle dispersion state of CNCs in the host polymer matrix.

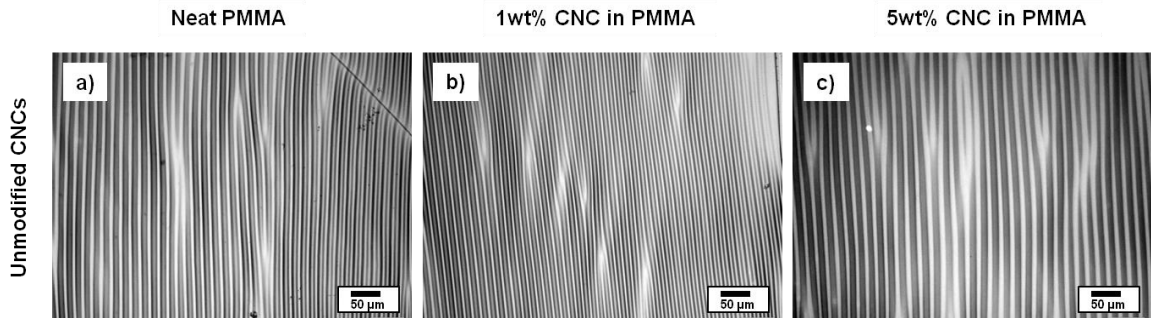


Figure 5.4 Optical micrographs of unmodified CNCs/PMMA system after applying compressive strain for thin film systems with varying concentrations of CNCs in PMMA at a) 0 wt% (neat PMMA), b) 1 wt% CNCs, and c) 5 wt% CNCs.

Buckling measurements were further acquired on modified cellulose nanocrystals to determine the effect of interparticle and particle-polymer interactions on CNC dispersion and its relationship to the elastic modulus. The PMMA-grafted-CNCs with low grafting density (LD) were utilized in this study and investigated as a function of different nanofiller concentrations from 1 wt% to 10 wt% CNCs in PMMA homopolymer of molecular weight 30 kg/mol. Figure 5.5 displays the optical micrographs of the PMMA-g-CNCs in PMMA with nanofiller concentrations of 0 wt% CNCs, 1 wt% CNCs, and 5 wt% CNCs. The sinusoidal buckling patterns observed in the optical micrographs suggest overall regular periodicity, despite minor localized aggregates that are visible with optical microscopy at higher nanofiller concentrations.

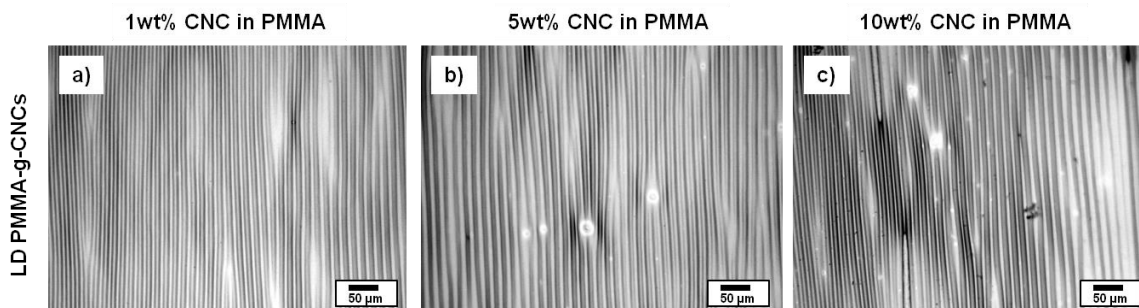


Figure 5.5 Optical micrographs of PMMA-grafted-CNCs/PMMA system after applying compressive strain for each thin film system with varying concentrations of CNCs in PMMA at a) 1 wt% CNCs, b) 5 wt% CNCs, and c) 10 wt% CNCs.

The calculated modulus for each CNC/PMMA thin film system was obtained from the measured buckling wavelength. This is summarized in Figure 5.6 which demonstrates the film modulus for each polymer nanocomposite thin film as a function of nanofiller concentration for incorporation of unmodified CNCs (u-CNC) and PMMA-grafted-CNCs of low grafting density (LD PMMA-g-CNC). The PMMA thin film (without nanoparticles) displays a significant increase in the film modulus with the addition of 5 wt% u-CNCs from 2.63 GPa to 5.07 GPa, respectively. The PMMA-grafted-CNCs exhibit a similar trend with increased modulus with increasing nanofiller concentration, where the incorporation of 5 wt% PMMA-g-CNCs results in a modulus of 3.61 GPa. The modulus of PMMA with 5 wt% PMMA-g-CNCs corresponds to significant enhancement of the thin film system by approximately 37%. Furthermore, increasing the PMMA-g-CNC concentration to 10 wt% in PMMA results in a corresponding modulus value of 4.82 GPa.

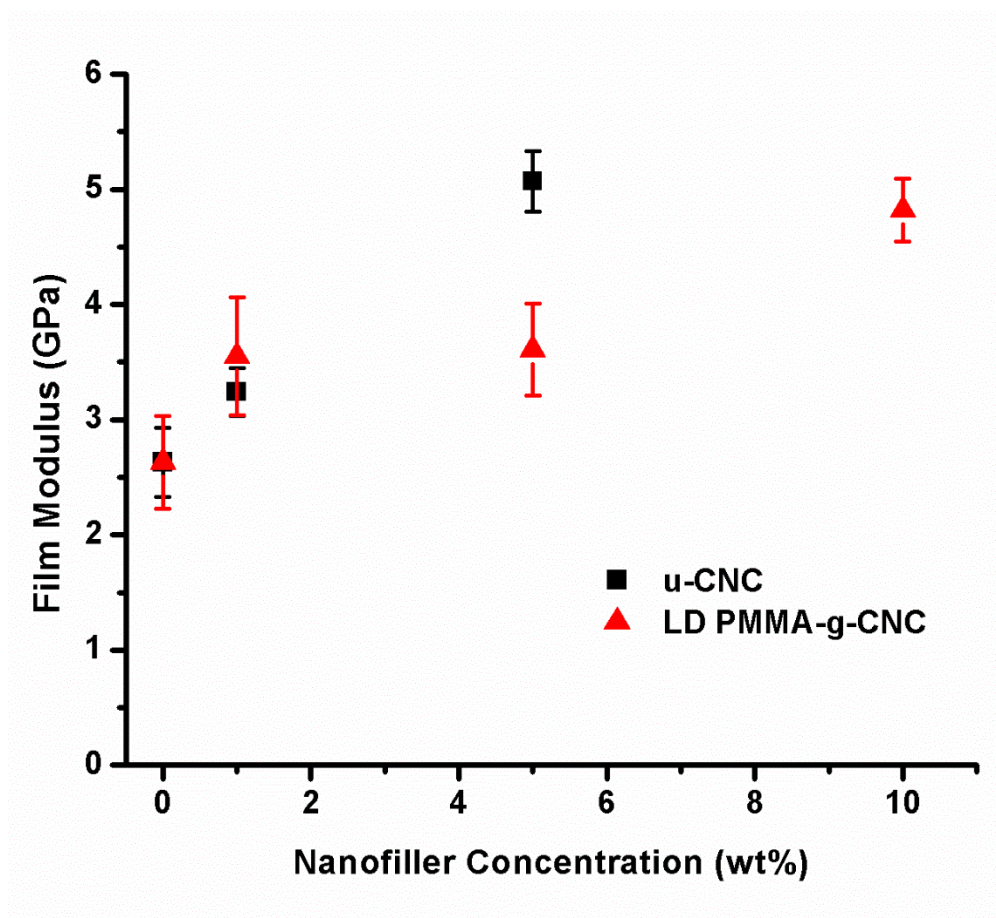


Figure 5.6 Elastic moduli calculated from buckling wavelength as a function of nanofiller concentrations for the thin film systems of unmodified CNCs (u-CNC) in PMMA and PMMA-grafted CNCs of low grafting density in PMMA homopolymer.

While the mechanical enhancement is certainly pronounced for both thin film systems at relatively low nanofiller loadings, in comparison to the u-CNCs, this suggests that less unmodified cellulose nanocrystals are needed to produce a similar reinforcing effect, which can be ascribed to the molecular level interactions. The film morphology from AFM micrographs in the previous Chapter III reflected the nanoparticle dispersion states in a PMMA homopolymer matrix. Due to the low grafting density of PMMA-grafted-CNCs, insufficient surface coverage of the cellulose nanocrystals prompted attractive interparticle

interactions which resulted in particle aggregation observed through surface topography measurements. In contrast, the unmodified CNCs in PMMA showed individually, well-dispersed nanorods in the polymer film which is likely attributed to strong interactions between the filler and polymer matrix. The interactions between the CNCs and PMMA can be ascribed to the formation of hydrogen bonds between the carbonyl groups of PMMA and the hydroxyl groups in cellulose.

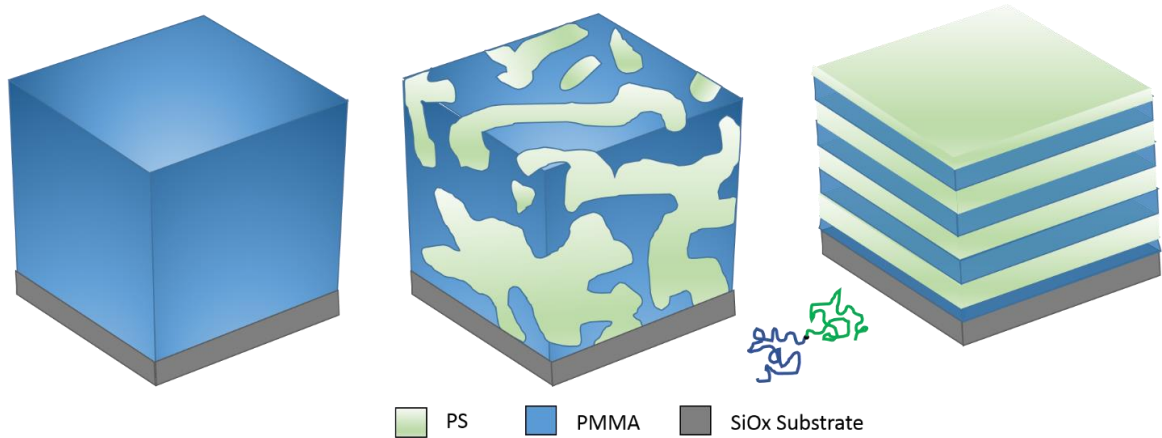


Figure 5.7 Schematic representation of different polymer thin film systems on silicon substrates comprised of poly(methyl methacrylate) homopolymer and poly(styrene-block-methyl methacrylate) in the as-cast and annealed states.

To that end, the CNC reinforcement effect can be further manipulated by precise control over the dispersion of anisotropic nanofillers through tailored interparticle and particle-polymer interactions in a highly ordered block copolymer thin film. The effect of cellulose nanocrystals confined within the subsequent nanostructure will be studied in

further detail as shown in Figure 5.7 to decouple the CNC dispersion and distribution effects, as well as the subsequent nanoparticle alignment and orientation, on its mechanical properties. One of the main challenges with obtaining mechanical characterization of the nanostructured BCP thin film was in transferring the annealed substrate-supported film to the pre-stretched PDMS. The BCP thin films cast on UV-ozone exposed silicon substrates required thermal annealing of the polymer nanocomposite thin films above the polymer's glass transition temperature T_g to microphase separate. However, upon annealing the PMMA has a strong affinity to the native oxide layer on the silicon substrate which proves troublesome for film transfer through the aforementioned water immersion technique.

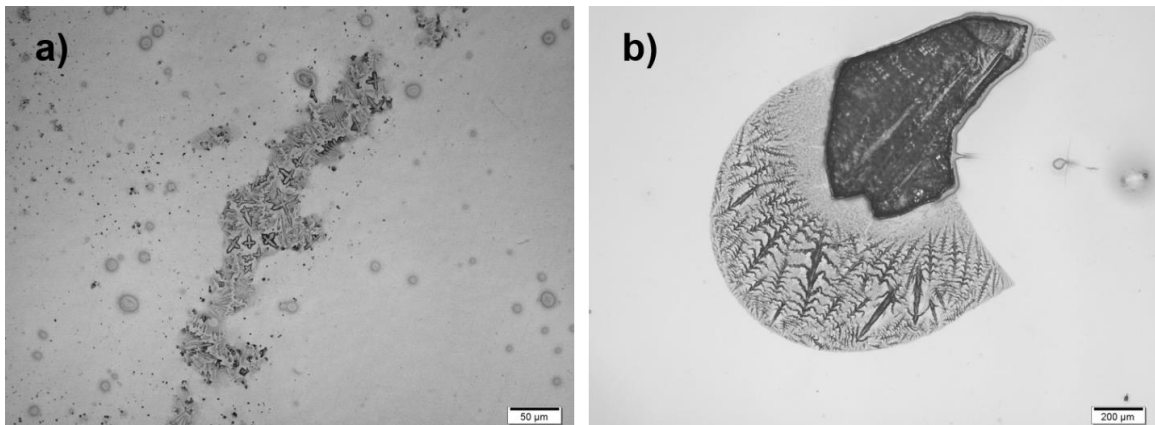


Figure 5.8 Optical micrographs of annealed BCP films transferred to PDMS from the salt crystal substrate with a scale bar of a) 50 μm and b) 200 μm .

An alternative solution was proposed to utilize sodium chloride (NaCl) windows as a substrate to cast films directly onto the smooth surface and subjected to thermal annealing. The NaCl immediately dissolved when submerged in a water bath, allowing for film lift-off and successful film transfer to PDMS. However, microscopy measurements

displayed defects and residual salt on the film surface as shown in Figure 5.8. To obtain accurate mechanical properties of the nanocomposite systems *via* SIEBIMM approach, homogeneous films of uniform thickness are required and thus the film transfer process will need to be optimized in future studies.

5.4 Conclusion

In this work, we provided mechanical characterization of substrate-supported polymer nanocomposite films *via* strain-induced elastic buckling instability for mechanical measurements. The elastic moduli were investigated for the multiphase thin film system comprised of cellulose nanocrystals dispersed in PMMA as a function of varying nanofiller concentrations for unmodified CNCs and LD PMMA-grafted-CNCs. The polymer nanocomposite thin films displayed significant enhancement in the elastic modulus with a relatively low nanofiller concentration wherein cellulose nanocrystals acted as effective reinforcing agents in the nanoscale films. The addition of 5 wt% unmodified CNCs to PMMA resulted in a nearly two-fold increase in the elastic modulus from 2.63 GPa to 5.07 GPa, which can be ascribed to strong hydrogen bonding interactions between the hydroxyl groups on the cellulose and carbonyl groups on the PMMA. For the PMMA-grafted-CNC/PMMA composite system, 1 wt% PMMA-g-CNC displayed a 35% increase in modulus as compared to the neat PMMA thin film without nanoparticles. However further increasing the nanofiller concentration to 5 wt% PMMA-g-CNCs in PMMA only slightly increased by 2%. This trend can be reflected in the dispersion state of the nanorods, where the low grafting density results in relatively low surface coverage which promotes localized particle aggregation. Therefore, tailored interfacial interactions between the polymer

matrix chains and nanofillers are demonstrated to have a significant role on nanoparticle dispersion and the subsequent macroscopic properties of the composite material.

CHAPTER VI

SUMMARY

The objective of this research was to develop a simple yet robust strategy for the controlled dispersion and spatial distribution of anisotropic nanofillers within polymer thin films and to correlate the film morphology with the mechanical performance of multiphase systems. The directed self-assembly of block copolymers (BCP) *via* a thermal annealing approach was utilized as an effective route to fabricate highly ordered multilayer thin films wherein the inherent nanostructures were anticipated to organize the cellulose nanocrystals (CNCs) into alternating layers or localized at the interface depending on preferential interactions. The BCP system was selected where one block could potentially form hydrogen bonds between the CNCs in attempt to minimize NP aggregation from strong intramolecular and intermolecular hydrogen bonding between individual nanofillers. The annealed BCP thin film attained a morphology of completely parallel lamellae in which the lamellar microdomains were oriented parallel to the free surface. The addition of CNCs at a relatively low nanofiller concentration was shown to broaden the distribution of lamellar orientations and further increasing the CNCs in BCP resulted in loss of long range order within the system.

To maintain the multilayered structure and control nanorod dispersion, polymer grafted nanoparticles were utilized with PMMA chains grafted onto the nanorod surface.

The morphology and dispersion states of the PMMA-grafted-CNCs/BCP thin films were investigated as a function of nanofiller concentration and grafting density (σ) at a fixed brush length. Individual, well-dispersed PMMA-grafted-CNCs were observed at higher grafting densities where the increased surface coverage minimized attractive particle-particle interactions and promoted nanoparticle dispersion. The BCP morphology and orientation of the polymer nanocomposite thin films were maintained up to 20 wt% PMMA-g-CNCs which can be ascribed to the tailored interparticle and particle-polymer interactions. The lamellar repeat spacing, L_0 , remained fairly constant whereas the interfacial width exhibited a slight broadening at relatively high nanofiller concentrations.

The stability and wetting behavior of nanoscale thin films were next investigated through microscopy measurements on a non-attractive, low surface energy elastomeric substrate. Neat homopolymer films annealed above the glass transition temperature T_g resulted in film rupture and spontaneous dewetting to minimize unfavorable interactions between the PMMA film and PDMS substrate. The presence of anisotropic nanofillers such as cellulose nanocrystals were observed to significantly retard dewetting kinetics and film stabilization was achieved at a critical particle threshold. This was attributed to the high affinity of the nanofillers with the polymer matrix, rather than nanoparticle-driven segregation to the substrate which was observed in previous dewetting inhibition studies to modify the substrate-film interactions. Furthermore, block copolymer ordering was achieved on flexible, low surface energy elastomeric substrates without any required substrate modification which has important implications towards the field of nanotechnology and flexible electronics.

To gain insight into the mechanical properties of the sub-micron multicomponent systems, the elastic modulus was determined using strain-induced elastic buckling instability for mechanical measurements (SIEBIMM). Significant enhancement in the elastic modulus was observed with the incorporation of cellulose nanocrystals in a PMMA homopolymer thin film. The modulus increased nearly two-fold from 2.63 GPa to 5.07 GPa for the neat PMMA and 5 wt% unmodified CNCs in PMMA systems, respectively. This was attributed to strong hydrogen bonding interactions between the hydroxyl groups on the cellulose and the carbonyl groups on the PMMA which promoted nanoparticle dispersion as confirmed through microscopy techniques. The reinforcement effect was more pronounced in comparison to the modified CNC system of PMMA-grafted-CNCs with a low grafting density which exhibited well-dispersed rod-like particles at low nanofiller concentration and severe aggregates formed in PMMA with increased particle loading. Therefore, strong matrix-filler interactions and the homogeneous dispersion of nanofillers are anticipated to play a key role in governing the degree of enhancement in the mechanical properties of nanoscale films.

The controlled assembly of anisotropic nanofillers in polymer thin films was demonstrated in this work through the use of block copolymer scaffolds and surface chemistry modification to gain a fundamental understanding on how the interfacial interactions and subsequent nanostructures contribute to the macroscopic performance of a polymeric material. This proved to be a novel strategy to manipulate the spatial organization of particles at the nanoscale which can pave the way towards the development of engineered hybrid materials with multifunctional properties. A promising area to explore in the future as an extension of this work involves utilizing renewable biopolymers for the

application of cellulose nanocrystals in biodegradable packaging materials. Nevertheless, the ability to achieve uniform nanoparticle dispersion and create arrays of ordered nanostructures with polymer nanocomposites has great technological significance for reinforced structural components and in the design and fabrication of high performance, yet lightweight materials.

REFERENCES

- (1) Reiter, G. Unstable Thin Polymer Films: Rupture and Dewetting Processes. *Langmuir* **1993**, *9*, 1344–1351.
- (2) Reiter, G. Dewetting of Thin Polymer Films. *Phys. Rev. Lett.* **1992**, *68*, 75–78.
- (3) Sharma A., R. G. Instability of Thin Polymer Films on Coated Substrates: Rupture, Dewetting, and Drop Formation. *J. Colloid Interface Sci.* **1996**, *178*, 383–399.
- (4) Redon, C.; Brzoska, J. B.; Brochard-Wyart, F. Dewetting and Slippage of Microscopic Polymer Films. *Macromolecules* **1994**, *27*, 468–471.
- (5) Brochard-Wyart, F.; de Gennes, P.-G.; Hervert, H.; Redon, C. Wetting and Slippage of Polymer Melts on Semi-Ideal Surfaces. *Langmuir* **1994**, *10*, 1566–1572.
- (6) Choi, S. H.; Zhang Newby, B. M. Suppress Polystyrene Thin Film Dewetting by Modifying Substrate Surface with Aminopropyltriethoxysilane. *Surf. Sci.* **2006**, *600*, 1391–1404.
- (7) Chen, X. C.; Li, H. M.; Fang, F.; Wu, Y. W.; Wang, M.; Ma, G. Bin; Ma, Y. Q.; Shu, D. J.; Peng, R. W. Confinement-Induced Ordering in Dewetting and Phase Separation of Polymer Blend Films. *Adv. Mater.* **2012**, *24*, 2637–2641.
- (8) Peng, J.; Xing, R.; Wu, Y.; Li, B.; Han, Y.; Knoll, W.; Kim, D. H. Dewetting of Thin Polystyrene Films under Confinement. *Langmuir* **2007**, *23*, 2326–2329.
- (9) Bhandaru, N.; Das, A.; Mukherjee, R. Confinement Induced Ordering in Dewetting of Ultra Thin Polymer Bilayers on Nano Patterned Substrates. *Nanoscale* **2015**, *8*, 1073–1087.
- (10) Suh, K. Y.; Park, J.; Lee, H. H. Controlled Polymer Dewetting by Physical Confinement. *J. Chem. Phys.* **2002**, *116*, 7714–7718.
- (11) De Gennes, P. G. Wetting: Statics and Dynamics. *Rev. Mod. Phys.* **1985**, *57*, 827–863.

- (12) Ellison, C. J.; Kim, S. D.; Hall, D. B.; Torkelson, J. M. Confinement and Processing Effects on Glass Transition Temperature and Physical Aging in Ultrathin Polymer Films: Novel Fluorescence Measurements. *Eur. Phys. J. E* **2002**, *8*, 155–166.
- (13) Mundra, M. K.; Ellison, C. J.; Behling, R. E.; Torkelson, J. M. Confinement, Composition, and Spin-Coating Effects on the Glass Transition and Stress Relaxation of Thin Films of Polystyrene and Styrene-Containing Random Copolymers: Sensing by Intrinsic Fluorescence. *Polymer (Guildf)*. **2006**, *47*, 7747–7759.
- (14) Mundra, M. K.; Donthu, S. K.; Dravid, V. P.; Torkelson, J. M. Effect of Spatial Confinement on the Glass-Transition Temperature of Patterned Polymer Nanostructures. *Nano Lett.* **2007**, *7*, 713–718.
- (15) Ellison, C. J.; Torkelson, J. M. The Distribution of Glass-Transition Temperatures in Nanoscopically Confined Glass Formers. *Nat. Mater.* **2003**, *2*, 695–700.
- (16) Paul, D. R.; Robeson, L. M. Polymer Nanotechnology: Nanocomposites. *Polymer (Guildf)*. **2008**, *49*, 3187–3204.
- (17) Thellen, C.; Schirmer, S.; Ratto, J. A.; Finnigan, B.; Schmidt, D. Co-Extrusion of Multilayer Poly(m-Xylylene Adipimide) Nanocomposite Films for High Oxygen Barrier Packaging Applications. *J. Memb. Sci.* **2009**, *340*, 45–51.
- (18) Kashiwagi, T.; Du, F.; Douglas, J. F.; Winey, K. I.; Harris, R. H.; Shields, J. R. Nanoparticle Networks Reduce the Flammability of Polymer Nanocomposites. *Nat. Mater.* **2005**, *4*, 928–933.
- (19) Kashiwagi, T.; Morgan, A. B.; Antonucci, J. M.; Vanlandingham, M. R.; Harris, R. H.; Awad, W. H.; Shields, J. R. Thermal and Flammability Properties of a Silica – Poly (Methylmethacrylate) Nanocomposite. *J. Appl. Polym. Sci.* **2003**, *89*, 2072–2078.
- (20) Palmero, P. Structural Ceramic Nanocomposites: A Review of Properties and Powders' Synthesis Methods. *Nanomaterials* **2015**, *5*, 656–696.
- (21) Besancon, B. M.; Green, P. F. Polystyrene-Based Single-Walled Carbon Nanotube Nanocomposite Thin Films: Dynamics of Structural Instabilities. *Macromolecules* **2005**, *38*, 110–115.
- (22) Ortiz, C.; Boyce, M. Bioinspired Structural Materials. *Science (80-.)*. **2008**, *14*, 1053–1054.
- (23) Petersson, L.; Oksman, K. Biopolymer Based Nanocomposites: Comparing Layered Silicates and Microcrystalline Cellulose as Nanoreinforcement. *Compos. Sci. Technol.* **2006**, *66*, 2187–2196.

- (24) Wang, T. a O. Cellulose Nanowhiskers And Nanofibers From Biomass for Composite Applications. **2011**.
- (25) Dong, H.; Strawhecker, K. E.; Snyder, J. F.; Orlicki, J. a.; Reiner, R. S.; Rudie, A. W. Cellulose Nanocrystals as a Reinforcing Material for Electrospun Poly(methyl Methacrylate) Fibers: Formation, Properties and Nanomechanical Characterization. *Carbohydr. Polym.* **2012**, *87*, 2488–2495.
- (26) Lee, K.-Y.; Aitomäki, Y.; Berglund, L. a.; Oksman, K.; Bismarck, A. On the Use of Nanocellulose as Reinforcement in Polymer Matrix Composites. *Compos. Sci. Technol.* **2014**, *105*, 15–27.
- (27) Xu, X.; Liu, F.; Jiang, L.; Zhu, J. Y.; Haagensohn, D.; Wiesenborn, D. P. Cellulose Nanocrystals vs. Cellulose Nano Fibrils: A Comparative Study on Their Microstructures and Effects as Polymer Reinforcing Agents. **2013**.
- (28) Plackett, D. V.; Letchford, K.; Jackson, J. K.; Burt, H. M.; Jackson, J.; Burt, H. A Review of Nanocellulose as a Novel Vehicle for Drug Delivery. *Nord. Pulp. Pap. Res. J.* **2014**, *29*, 105–118.
- (29) Carpenter, A. W.; De Lannoy, C. F.; Wiesner, M. R. Cellulose Nanomaterials in Water Treatment Technologies. *Environ. Sci. Technol.* **2015**, *49*, 5277–5287.
- (30) Yang, C.; Wong, C. P.; Yuen, M. M. F. Printed Electrically Conductive Composites: Conductive Filler Designs and Surface Engineering. *J. Mater. Chem. C* **2013**, *1*, 4052.
- (31) Favier, V.; Cavaille, J. Y.; Canova, G. R.; Shrivastava, S. C. Mechanical Percolation in Cellulose Whisker Nanocomposites. *Polym. Eng. Sci.* **1997**, *37*, 1732–1739.
- (32) Sharma, A.; Casoli, A.; David, M.; Khanna, R.; Auroy, P. Thin Film Instability Induced by Long-Range Forces. **1999**, 2551–2558.
- (33) Daillant, J and Wyart, F. B. Drying of Solids Wetted by Thin Liquid Films. *Can. J. Phys.* **1990**, *68*, 1084–1088.
- (34) Xie, R.; Karim, a.; Douglas, J.; Han, C.; Weiss, R. Spinodal Dewetting of Thin Polymer Films. *Phys. Rev. Lett.* **1998**, *81*, 1251–1254.
- (35) Higgins, a. M.; Jones, R. a. L. Anisotropic Spinodal Dewetting as a Route to Self-Assembly of Patterned Surfaces. *Nature* **2000**, *404*, 476–478.
- (36) Stange, T. G.; Evans, D. F.; Hendrickson, W. a. Nucleation and Growth of Defects Leading to Dewetting of Thin Polymer Films. *Langmuir* **1997**, *13*, 4459–4465.

- (37) Mukherjee, R.; Bandyopadhyay, D.; Sharma, A. Control of Morphology in Pattern Directed Dewetting of a Thin Polymer Films. *Soft Matter* **2008**, *4*, 2086–2097.
- (38) Rayleigh, Lord. On The Instability Of Jets. *Proc. London Math. Soc.* **1878**, *s1-10*, 4–13.
- (39) Roy, S.; Biswas, D.; Salunke, N.; Das, A.; Vutukuri, P.; Singh, R.; Mukherjee, R. Control of Morphology in Pattern Directed Dewetting of a Thin Polymer Bilayer. *Macromolecules* **2013**, *46*, 935–948.
- (40) Verma, A.; Sharma, A. Taming of Self-Organization in Highly Confined Soft Matter to Sub-100 Nm Scales: Nanolens-Arrays by Spinodal Instability of Thin Polymer Films for High-Resolution Optical Imaging. *Curr. Sci.* **2013**, *104*, 1037–1045.
- (41) Tisserant, J. N.; Hany, R.; Partel, S.; Bona, G. L.; Mezzenga, R.; Heier, J. Dewetting-Driven Hierarchical Self-Assembly of Small Semiconducting Molecules. *Soft Matter* **2012**, *8*, 5804–5810.
- (42) Li, L.; Chen, K.; Sun, L.; Xie, S.; Lin, S. Fabrication of Patterned Carbon Nanotubes with Adjustable Arrays through Controlled Mesoscopic Dewetting. *React. Funct. Polym.* **2013**, *73*, 83–88.
- (43) Farrell, R. a.; Kehagias, N.; Shaw, M. T.; Reboud, V.; Zelsmann, M.; Holmes, J. D.; Sotomayor Torres, C. M.; Morris, M. a. Surface-Directed Dewetting of a Block Copolymer for Fabricating Highly Uniform Nanostructured Microdroplets and Concentric Nanorings. *ACS Nano* **2011**, *5*, 1073–1085.
- (44) Yerushalmi-Rozen, R.; Klein, J.; Fetters, L. J. Suppression of Rupture in Thin, Nonwetting Liquid Films. *Science* **1994**, *263*, 793–795.
- (45) Jiang, N.; Wang, J.; Di, X.; Cheung, J.; Zeng, W.; Endoh, M. K.; Koga, T.; Satija, S. K. Nanoscale Adsorbed Structures as a Robust Approach for Tailoring Polymer Film Stability. *Soft Matter* **2016**, *12*, 1801–1809.
- (46) Feng, Y.; Karim, A.; Weiss, R. a; Douglas, J. F.; Han, C. C. Control of Polystyrene Film Dewetting through Sulfonation and Metal Complexation. *Macromolecules* **1998**, *31*, 484–493.
- (47) Wei, B.; Genzer, J.; Spontak, R. J. Dewetting Behavior of a Block Copolymer/homopolymer Thin Film on an Immiscible Homopolymer Substrate. *Langmuir* **2004**, *20*, 8659–8667.
- (48) Costa, A. C.; Composto, R. J.; Vlček, P. Dewetting of Thin Film Blends Containing Block Copolymer: Effects of Nonadsorbing Block Length and Substrate Hydrophobicity. *Macromolecules* **2003**, *36*, 3254–3260.

- (49) Carroll, G. T.; Turro, N. J.; Koberstein, J. T. Patterning Dewetting in Thin Polymer Films by Spatially Directed Photocrosslinking. *J. Colloid Interface Sci.* **2010**, *351*, 556–560.
- (50) Henn, G.; Bucknall, D. G.; Stamm, M.; Vanhoorne, P.; Jerome, R. Chain End Effects and Dewetting in Thin Polymer Films. *Macromolecules* **1996**, *29*, 4305–4313.
- (51) Balazs, A. C.; Emrick, T.; Russell, T. P. Nanoparticle Polymer Composites: Where Two Small Worlds Meet. *Science* **2006**, *314*, 1107–1110.
- (52) Mohammad, M.; Winey, K. I. Polymer Nanocomposites Containing Carbon Nanotubes. *Macromolecules* **2006**, *39*, 5194–5205.
- (53) Crosby, A. J.; Lee, J. Polymer Nanocomposites: The “Nano” Effect on Mechanical Properties. *Polym. Rev.* **2007**, *47*, 217–229.
- (54) Zhang, S.; Fu, Y.; Du, H.; Liu, Y.; Chen, T. Nanocomposite Thin Films for Both Mechanical and Functional Applications. *Adv. Mater. Micro- Nano-Systems* **2004**, 1–5.
- (55) K. J. Loh, M. Thouless, J. P. L. Enhancing the Mechanical and Fracture Properties of Nanocomposites Using Carbon Nanotubes. *Proc. 12th Int. Conf. Fract.* **2009**, *1*, 1–10.
- (56) Mittal, G.; Dhand, V.; Rhee, K. Y.; Park, S.-J.; Lee, W. R. A Review on Carbon Nanotubes and Graphene as Fillers in Reinforced Polymer Nanocomposites. *J. Ind. Eng. Chem.* **2014**, *21*, 11–25.
- (57) Valentini, L.; Cardinali, M.; Fortunati, E.; Torre, L.; Kenny, J. M. A Novel Method to Prepare Conductive Nanocrystalline Cellulose/graphene Oxide Composite Films. *Mater. Lett.* **2013**, *105*, 4–7.
- (58) Usuki, A.; Kawasumi, M.; Kojima, Y.; Okada, A.; Kurauchi, T.; Kamigaito, O. Swelling Behavior of Montmorillonite Cation Exchanged for Ω -Amino Acids by ϵ -Caprolactam. *J. Mater. Res.* **1993**, *8*, 1174–1178.
- (59) O., K. Synthesis of Nylon 6-Clay Hybrid. *J. Mater. Res.* **1993**, *8*, 1179.
- (60) Kojima Yoshitsugu; Usuki Arimitsu; Kawasumi Masaya; Okada Akane; Fukushima Yoshiaki; Kurauchi Toshio; Kamigaito Osami. Mechanical Properties of Nylon 6-Clay Hybrid. *J. Mater. Res.* **1992**, *8*, 1185–1189.
- (61) Pyun, J.; Kowalewski, T.; Matyjaszewski, K. Synthesis of Polymer Brushes Using Atom Transfer Radical Polymerization. **2003**, 1043–1059.

- (62) Rungta, A.; Natarajan, B.; Neely, T.; Dukes, D.; Schadler, L. S.; Benicewicz, B. C. Grafting Bimodal Polymer Brushes on Nanoparticles Using Controlled Radical Polymerization. **2012**, 1–3.
- (63) Kumar, S. K.; Jouault, N.; Benicewicz, B.; Neely, T. Nanocomposites with Polymer Grafted Nanoparticles. *Macromolecules* **2013**, *46*, 3199–3214.
- (64) Arash, B.; Wang, Q.; Varadan, V. K. Mechanical Properties of Carbon Nanotube/polymer Composites. *Sci. Rep.* **2015**, *4*, 6479.
- (65) Qian, D.; Dickey, E. C.; Andrews, R.; Rantell, T. Load Transfer and Deformation Mechanisms in Carbon Nanotube-Polystyrene Composites. *Appl. Phys. Lett.* **2000**, *76*, 2868–2870.
- (66) Halpin, J. C.; Kardos, J. L. The Halpin-Tsai Equations: A Review. *Polym. Eng. Sci.* **1976**, *16*, 344–352.
- (67) Ye, H.; Lam, H.; Titchenal, N.; Gogotsi, Y.; Ko, F. Reinforcement and Rupture Behavior of Carbon Nanotubes-Polymer Nanofibers. *Appl. Phys. Lett.* **2004**, *85*, 1775–1777.
- (68) Basta, M.; Picciarelli, V.; Stella, R. An Introduction to Percolation. *Eur. J. Phys.* **1994**, *15*, 97–101.
- (69) Takayanagi, M.; Uemura, S.; Minami, S. Application of Equivalent Model Method to Dynamic Rheo-Optical Properties of Crystalline Polymer. *J. Polym. Sci. Part C Polym. Symp.* **1964**, *5*, 113–122.
- (70) Ouali, N.; Cavaille, J. Y.; Perez, J. Elastic, Viscoelastic and Plastic Behavior of Multiphase Polymer Blends. *Plast. Rubber Compos. Process. Appl.* **1991**, *16*, 55–60.
- (71) Favier, V.; Dendievel, R.; Canova, G.; Cavaille, J. Y.; Gilormini, P. Simulation and Modeling of Three-Dimensional Percolating Structures: Case of a Latex Matrix Reinforced by a Network of Cellulose Fibers. *Acta Mater.* **1997**, *45*, 1557–1565.
- (72) Yoshimoto, K.; Jain, T. S.; Nealey, P. F.; De Pablo, J. J. Local Dynamic Mechanical Properties in Model Free-Standing Polymer Thin Films. *J. Chem. Phys.* **2005**, *122*.
- (73) Hartschuh, R.; Ding, Y.; Roh, J. H.; Kisliuk, a.; Sokolov, a P.; Soles, C. L.; Jones, R. L.; Hu, T. J.; Wu, W. L.; Mahorowala, a. P. Brillouin Scattering Studies of Polymeric Nanostructures. *J. Polym. Sci. B* **2004**, *42*, 1106–1113.
- (74) Stafford, C. M.; Vogt, B. D.; Harrison, C.; Julthongpiput, D.; Huang, R. Elastic Moduli of Ultrathin Amorphous Polymer Films. *Macromolecules* **2006**, *39*, 5095–5099.

- (75) Chung, J. Y.; Lee, J. H.; Beers, K. L.; Stafford, C. M. Stiffness, Strength, and Ductility of Nanoscale Thin Films and Membranes: A Combined Wrinkling-Cracking Methodology. *Nano Lett.* **2011**, *11*, 3361–3365.
- (76) Van Workum, K.; de Pablo, J. J. Computer Simulation of the Mechanical Nanostructures. *Nano Lett.* **2003**, *3*, 1405–1410.
- (77) Hall, D. B.; Torkelson, J. M. Small Molecule Probe Diffusion in Thin and Ultrathin Supported Polymer Films. *Macromolecules* **1998**, *31*, 8817–8825.
- (78) Frank, B.; Gast, a. P.; Russell, T. P.; Brown, H. R.; Hawker, C. Polymer Mobility in Thin Films. *Macromolecules* **1996**, *29*, 6531–6534.
- (79) Kawana, S.; Jones, R. a L. Effect of Physical Ageing in Thin Glassy Polymer Films. *Eur. Phys. J. E* **2003**, *10*, 223–230.
- (80) Priestley, R. D.; Rittigstein, P.; Broadbelt, L. J.; Fukao, K.; Torkelson, J. M. Evidence for the Molecular-Scale Origin of the Suppression of Physical Ageing in Confined Polymer: Fluorescence and Dielectric Spectroscopy Studies of Polymer-silica Nanocomposites. *J. Phys. Condens. Matter* **2007**, *19*, 205120.
- (81) Priestley, R. D. Structural Relaxation of Polymer Glasses at Surfaces, Interfaces, and In Between. *Science (80-.)*. **2005**, *309*, 456–459.
- (82) Forrest, J. a.; Dalnoki-Veress, K.; Stevens, J. R.; Dutcher, J. R. Effect of Free Surfaces on the Glass Transition Temperature of Thin Polymer Films. *Phys. Rev. Lett.* **1996**, *77*, 2002–2005.
- (83) Forrest, J. a.; Dalnoki-Veress, K. The Glass Transition in Thin Polymer Films. *Adv. Colloid Interface Sci.* **2001**, *94*, 167–196.
- (84) Forrest, J. a.; Dalnoki-Veress, K.; Dutcher, J. R. Interface and Chain Confinement Effects on the Glass Transition Temperature of Thin Polymer Films. *Phys. Rev. E* **1997**, *56*, 5705–5716.
- (85) Keddie, J. L. I.; Jones, R. a L.; Cory, R. a; Colledge, P.; Cb, C. Size-Dependent Depression of the Glass Transition Temperature in Polymer Films . *Polymer (Guildf)*. **1994**, *27*, 59–64.
- (86) DeMaggio, G. B.; Frieze, W. E.; Gidley, D. W.; Zhu, M.; Hristov, H. a.; Yee, a. F. Interface and Surface Effects on the Glass Transition in Thin Polystyrene Films. *Phys. Rev. Lett.* **1997**, *78*, 1524–1527.
- (87) Kawana, S.; Jones, R. a L. Character of the Glass Transition in Thin Supported Polymer Films. *Phys. Rev. E - Stat. Nonlinear, Soft Matter Phys.* **2001**, *63*, 1–6.

- (88) Fryer, D. S.; Nealey, P. F.; De Pablo, J. J. Thermal Probe Measurements of the Glass Transition Temperature for Ultrathin Polymer Films as a Function of Thickness. *Macromolecules* **2000**, *33*, 6439–6447.
- (89) Yang, Z.; Fujii, Y.; Lee, F. K.; Lam, C.; Tsui, O. K. C. Glass Transition Dynamics and. *Science (80-.)*. **2010**, *328*, 1676–1679.
- (90) Tsui, O. K. C.; Russell, T. P.; Hawker, C. J. Effect of Interfacial Interactions on the Glass Transition of Polymer Thin Films. *Macromolecules* **2001**, *34*, 5535–5539.
- (91) Ponting, M.; Burt, T. M.; Korley, L. T. J.; Andrews, J.; Hiltner, A.; Baer, E. Gradient Multilayer Films by Forced Assembly Coextrusion. *Ind. Eng. Chem. Res.* **2010**, *49*, 12111–12118.
- (92) Ma, M.; Vijayan, K.; Hiltner, a; Baer, E.; Im, J. Thickness Effects in Microlayer Composites of Polycarbonate and Poly(styrene Acrylonitrile). *J. Mater. Sci.* **1990**, *25*, 2039.
- (93) Mueller, C. D.; Nazarenko, S.; Ebeling, T.; Schuman, T. L.; Hiltner, A.; Baer, E. Novel Structures by Microlayer Coextrusion?talc-Filled PP, PC/SAN, and HDPE/LLDPE. *Polym. Eng. Sci.* **1997**, *37*, 355–362.
- (94) Mackey, M.; Hiltner, A.; Baer, E.; Flandin, L.; Wolak, M. A.; Shirk, J. S. Enhanced Breakdown Strength of Multilayered Films Fabricated by Forced Assembly Microlayer Coextrusion. *J. Phys. D. Appl. Phys.* **2009**, *42*, 175304.
- (95) Huntington, B. a.; Chabert, E.; Rahal, S.; Patz, J.; Silva, J.; Harris, P.; Maia, J.; Bonneau, R. T. Distortion of Interfaces in a Multilayer Polymer Co-Extrusion Feedblock. *Int. Polym. Process.* **2013**, *28*, 274–280.
- (96) Schrenk, W. J.; Bradley, N. L.; Alfrey, T.; Maack, H. Interfacial Flow Instability in Multilayer Coextrusion. *Polym. Eng. Sci.* **1978**, *18*, 620–623.
- (97) Gregory, B. L.; Siegmund, a.; Im, J.; Hiltner, a.; Baer, E. Deformation Behaviour of Coextruded Multilayer Composites with Polycarbonate and Poly(styrene-Acrylonitrile). *J. Mater. Sci.* **1987**, *22*, 532–538.
- (98) Zhao, R.; Macosko, C. W. Slip at Polymer–polymer Interfaces: Rheological Measurements on Coextruded Multilayers. *J. Rheol. (N. Y. N. Y.)*. **2002**, *46*, 145–167.
- (99) Hu, H.; Gopinadhan, M.; Osuji, C. O. Directed Self-Assembly of Block Copolymers: A Tutorial Review of Strategies for Enabling Nanotechnology with Soft Matter. *Soft Matter* **2014**, *10*, 3867.

- (100) Sarkar, B.; Alexandridis, P. Self-Assembled Block Copolymer - Nanoparticle Hybrids: Interplay between Enthalpy and Entropy Self-Assembled Block Copolymer - Nanoparticle Hybrids: Interplay between Enthalpy and Entropy Biswajit Sarkar and Paschalis Alexandridis *. **2012**.
- (101) Chiu, J. J.; Kim, B. J.; Kramer, E. J.; Pine, D. J. Control of Nanoparticle Location in Block Copolymers. *J. Am. Chem. Soc.* **2005**, *127*, 5036–5037.
- (102) Chiu, J. J.; Kim, B. J.; Yi, G. R.; Bang, J.; Kramer, E. J.; Pine, D. J. Distribution of Nanoparticles in Lamellar Domains of Block Copolymers. *Macromolecules* **2007**, *40*, 3361–3365.
- (103) Thompson, R. B.; Ginzburg, V. V.; Matsen, M. W.; Balazs, a C. Predicting the Mesophases of Copolymer-Nanoparticle Composites. *Science* **2001**, *292*, 2469–2472.
- (104) Thompson, R. B.; Ginzburg, V. V.; Matsen, M. W.; Balazs, A. C. Block Copolymer-Directed Assembly of Nanoparticles: Forming Mesoscopically Ordered Hybrid Materials. *Macromolecules* **2002**, *35*, 1060–1071.
- (105) Bockstaller, M. R.; Mickiewicz, R. a.; Thomas, E. L. Block Copolymer Nanocomposites: Perspectives for Tailored Functional Materials. *Adv. Mater.* **2005**, *17*, 1331–1349.
- (106) He, L.; Pan, Z.; Zhang, L.; Liang, H. Microphase Transitions of Block Copolymer/nanorod Composites under Shear Flow. *Soft Matter* **2011**, *7*, 1147.
- (107) Horechyy, A.; Nandan, B.; Zafeiropoulos, N. E.; Jehnichen, D.; Göbel, M.; Stamm, M.; Pospiech, D. Nanoparticle Directed Domain Orientation in Thin Films of Asymmetric Block Copolymers. *Colloid Polym. Sci.* **2014**.
- (108) Chen, K.; Ma, Y. Q. Ordering Stripe Structures of Nanoscale Rods in Diblock Copolymer Scaffolds. *J. Chem. Phys.* **2002**, *116*, 7783–7786.
- (109) Zhang, Q.; Gupta, S.; Emrick, T.; Russell, T. P. Surface-Functionalized CdSe Nanorods for Assembly in Diblock Copolymer Templates. *J. Am. Chem. Soc.* **2006**, *128*, 3898–3899.
- (110) Kim, B. J.; Chiu, J. J.; Yi, G. R.; Pine, D. J.; Kramer, E. J. Nanoparticle-Induced Phase Transitions in Diblock-Copolymer Films. *Adv. Mater.* **2005**, *17*, 2618–2622.
- (111) He, L.; Zhang, L.; Liang, H. Mono- or Bidisperse Nanorods Mixtures in Diblock Copolymers. *Polymer (Guildf)*. **2010**, *51*, 3303–3314.
- (112) Deshmukh, R. D.; Liu, Y.; Composto, R. J. Two-Dimensional Confinement of Nanorods in Block Copolymer Domains. *Nano Lett.* **2007**, *7*, 3662–3668.

- (113) Wang, D.; Hore, M. J. a; Ye, X.; Zheng, C.; Murray, C. B.; Composto, R. J. Gold Nanorod Length Controls Dispersion, Local Ordering, and Optical Absorption in Polymer Nanocomposite Films. *Soft Matter* **2014**, *10*, 3404–3413.
- (114) Lo, C. T.; Lin, W. T. Effect of Rod Length on the Morphology of Block Copolymer/magnetic Nanorod Composites. *J. Phys. Chem. B* **2013**, *117*, 5261–5270.
- (115) Shou, Z.; Buxton, G. a.; Balazs, A. C. Predicting the Self-Assembled Morphology and Mechanical Properties of Mixtures of Diblocks and Rod-like Nanoparticles. *Composite Interfaces*, 2003, *10*, 343–368.
- (116) Lee, J.-Y.; Thompson, R. B.; Jasnow, D.; Balazs, A. C. Entropically Driven Formation of Hierarchically Ordered Nanocomposites. *Phys. Rev. Lett.* **2002**, *89*, 155503.
- (117) Huynh, W. U.; Dittmer, J. J.; Alivisatos, a P. Hybrid Nanorod-Polymer Solar Cells. *Science (80-.)*. **2002**, *295*, 2425 LP – 2427.
- (118) Song, D. P.; Li, C.; Li, W.; Watkins, J. J. Block Copolymer Nanocomposites with High Refractive Index Contrast for One-Step Photonics. *ACS Nano* **2016**, *10*, 1216–1223.
- (119) Samant, S.; Grabowski, C. a; Kisslinger, K.; Yager, K. G.; Yuan, G.; Satija, S. K.; Raghavan, D.; Durstock, M. F.; Karim, A. Directed Self-Assembly of Block Copolymers for High Breakdown Strength Polymer Film Capacitors. *ACS Appl. Mater. Interfaces* **2016**, acsami.5b11851.
- (120) Shenhar, R.; Norsten, T. B.; Rotello, V. M. Polymer-Mediated Nanoparticle Assembly: Structural Control and Applications. *Adv. Mater.* **2005**, *17*, 657–669.
- (121) Zhao, Y.; Thorkelsson, K.; Mastroianni, A. J.; Schilling, T.; Luther, J. M.; Rancatore, B. J.; Matsunaga, K.; Jinnai, H.; Wu, Y.; Poulsen, D.; *et al.* Small-Molecule-Directed Nanoparticle Assembly towards Stimuli-Responsive Nanocomposites. *Nat. Mater.* **2009**, *8*, 979–985.
- (122) Xu, X.; Thwe, M. M.; Shearwood, C.; Liao, K. Mechanical Properties and Interfacial Characteristics of Carbon-Nanotube-Reinforced Epoxy Thin Films. *Appl. Phys. Lett.* **2002**, *81*, 2833–2835.
- (123) Cadek, M.; Coleman, J. N.; Ryan, K. P.; Nicolosi, V.; Bister, G.; Fonseca, a.; Nagy, J. B.; Szostak, K.; Béguin, F.; Blau, W. J. Reinforcement of Polymers with Carbon Nanotubes: The Role of Nanotube Surface Area. *Nano Lett.* **2004**, *4*, 353–356.
- (124) Coleman, J. N.; Khan, U.; Gun'ko, Y. K. Mechanical Reinforcement of Polymers Using Carbon Nanotubes. *Adv. Mater.* **2006**, *18*, 689–706.

- (125) Mackay, M. E.; Tuteja, A.; Duxbury, P. M.; Hawker, C. J.; Van Horn, B.; Guan, Z.; Chen, G.; Krishnan, R. S. General Strategies for Nanoparticle Dispersion. *Science* **2006**, *311*, 1740–1743.
- (126) Chandran, S.; Begam, N.; Basu, J. K. Dispersion of Polymer Grafted Nanoparticles in Polymer Nanocomposite Films: Insights from Surface X-Ray Scattering and Microscopy. *J. Appl. Phys.* **2014**, *116*.
- (127) Jayaraman, A. Polymer Grafted Nanoparticles: Effect of Chemical and Physical Heterogeneity in Polymer Grafts on Particle Assembly and Dispersion. *J. Polym. Sci. Part B Polym. Phys.* **2013**, *51*, 524–534.
- (128) He, J.; Sill, K.; Xiang, H. Self-Directed Self-Assembly of Nanoparticle / Copolymer Mixtures. *Nature* **2005**, *404*, 55–59.
- (129) Xu, C.; Ohno, K.; Ladmiral, V.; Composto, R. J. Dispersion of Polymer-Grafted Magnetic Nanoparticles in Homopolymers and Block Copolymers. *Polymer (Guildf)*. **2008**, *49*, 3568–3577.
- (130) Mariano, M.; El Kissi, N.; Dufresne, A. Cellulose Nanocrystals and Related Nanocomposites: Review of Some Properties and Challenges. *J. Polym. Sci. Part B Polym. Phys.* **2014**, *52*, 791–806.
- (131) Peresin, M. S.; Habibi, Y.; Rojas, O. J.; Pawlak, J. J.; Sciences, M. Cellulose Nanocrystals as Reinforcement of Poly Vinyl Alcohol Nanocomposites. North Carolina State University. **2010**, 1–2.
- (132) Habibi, Y.; Lucia, L. A.; Rojas, O. J. Cellulose Nanocrystals : Chemistry , Self-Assembly , and Applications. **2009**.
- (133) Moon, R. J.; Martini, A.; Nairn, J.; Simonsen, J.; Youngblood, J. *Cellulose Nanomaterials Review: Structure, Properties and Nanocomposites.*; 2011; Vol. 40.
- (134) Stafford, C. M.; Roskov, K. E.; Epps, T. H.; Fasolka, M. J. Generating Thickness Gradients of Thin Polymer Films via Flow Coating. *Rev. Sci. Instrum.* **2006**, *77*, 1–7.
- (135) Smilgies, D.; Busch, P.; Papadakis, C.; Posselt, D. Characterization of Polymer Thin Films with Small-angle X-ray Scattering under Grazing Incidence (GISAXS), 2002.
- (136) Torikai, N.; Yamada, N. L.; Noro, A.; Harada, M.; Kawaguchi, D.; Takano, A.; Matsushita, Y. Neutron Reflectometry on Interfacial Structures of the Thin Films of Polymer and Lipid. *Polym. J.* **2007**, *39*, 1238–1246.

- (137) Roman, M.; Winter, W. T. Effect of Sulfate Groups from Sulfuric Acid Hydrolysis on the Thermal Degradation Behaviour of Bacterial Cellulose. *Biomacromolecules* **2004**, 1671–1677.
- (138) Wang, N.; Ding, E.; Cheng, R. Thermal Degradation Behaviors of Spherical Cellulose Nanocrystals with Sulfate Groups. *Polymer (Guildf)*. **2007**, 48, 3486–3493.
- (139) Suh, K. Y.; Lee, H. H. Capillary Force Lithography: Large-Area Patterning, Self-Organization, and Anisotropic Dewetting. *Adv. Funct. Mater.* **2002**, 12, 405–413.
- (140) Khang, D. Y.; Lee, H. H. Pressure-Assisted Capillary Force Lithography. *Adv. Mater.* **2004**, 16, 176–179.
- (141) Jeong, H. E.; Kwak, R.; Khademhosseini, A.; Suh, K. Y. UV-Assisted Capillary Force Lithography for Engineering Biomimetic Multiscale Hierarchical Structures: From Lotus Leaf to Gecko Foot Hairs. *Nanoscale* **2009**, 1, 331–338.
- (142) Meyer, W. H. Polymer Electrolytes for Lithium-Ion Batteries. *Adv. Mater.* **1998**, 10, 439–448.
- (143) Li, X.; Yu, X.; Han, Y. Polymer Thin Films for Antireflection Coatings. *J. Mater. Chem. C* **2013**, 1, 2266–2285.
- (144) Friend, R. H.; Gymer, R. W.; Holmes, a. B.; Burroughes, J. H.; Marks, R. N.; Taliani, C.; Bradley, D. D. C.; Santos, D. a. Dos; Bredas, J. L.; Logdlund, M.; *et al.* Electroluminescence in Conjugated Polymers. *Nature* **1999**, 397, 121–128.
- (145) Chen, L. M.; Hong, Z.; Li, G.; Yang, Y. Recent Progress in Polymer Solar Cells: Manipulation of Polymer: Fullerene Morphology and the Formation of Efficient Inverted Polymer Solar Cells. *Adv. Mater.* **2009**, 21, 1434–1449.
- (146) Barnes, K. a.; Karim, A.; Douglas, J. F.; Nakatani, A. I.; Gruell, H.; Amis, E. J. Suppression of Dewetting in Nanoparticle-Filled Polymer Films. *Macromolecules* **2000**, 33, 4177–4185.
- (147) Mackay, M. E.; Hong, Y.; Jeong, M.; Hong, S.; Russell, T. P.; Hawker, C. J.; Vestberg, R.; Douglas, J. F. Influence of Dendrimer Additives on the Dewetting of Thin Polystyrene Films. *Langmuir* **2002**, 18, 1877–1882.
- (148) Luo, H.; Gersappe, D. Dewetting Dynamics of Nanofilled Polymer Thin Films. *Macromolecules* **2004**, 37, 5792–5799.
- (149) Roy, S.; Bandyopadhyay, D.; Karim, A.; Mukherjee, R. Interplay of Substrate Surface Energy and Nanoparticle Concentration in Suppressing Polymer Thin Film Dewetting. *Macromolecules* **2015**.

- (150) Bandyopadhyay, D.; Douglas, J. F.; Karim, A. Fullerene Nanoparticles as Molecular Surfactant for Dewetting of Phase-Separating Polymer Blend Films. *Macromolecules* **2012**, *45*, 4716–4722.
- (151) Hosaka, N.; Torikai, N.; Otsuka, H.; Takahara, A. Structure and Dewetting Behavior of Polyhedral Oligomeric Silsesquioxane-Filled Polystyrene Thin Films. *Langmuir* **2007**, *23*, 902–907.
- (152) Hosaka, N.; Otsuka, H.; Hino, M.; Takahara, A. Control of Dispersion State of Silsesquioxane Nanofillers for Stabilization of Polystyrene Thin Films. *Langmuir* **2008**, *24*, 5766–5772.
- (153) Mukherjee, R.; Das, S.; Das, A.; Sharma, S. K.; Raychaudhuri, A. K.; Sharma, A. Stability and Dewetting of Metal Nanoparticle Filled Thin Polymer Films: Dynamics. *ACS Nano* **2010**, *4*, 3709–3724.
- (154) Xavier, J. H.; Sharma, S.; Seo, Y. S.; Isseroff, R.; Koga, T.; White, H.; Ulman, a.; Shin, K.; Satija, S. K.; Sokolov, J.; *et al.* Effect of Nanoscopic Fillers on Dewetting Dynamics. *Macromolecules* **2006**, *39*, 2972–2980.
- (155) Krishnan, R. S.; Mackay, M. E.; Hawker, C. J.; Van Horn, B. Influence of Molecular Architecture on the Dewetting of Thin Polystyrene Films. *Langmuir* **2005**, *21*, 5770–5776.
- (156) Che, J.; Jawaid, A.; Grabowski, C. a.; Yi, Y.-J.; Louis, G. C.; Ramakrishnan, S.; Vaia, R. a. Stability of Polymer Grafted Nanoparticle Monolayers: Impact of Architecture and Polymer–Substrate Interactions on Dewetting. *ACS Macro Lett.* **2016**, *5*, 1369–1374.
- (157) Koo, J.; Shin, K.; Seo, Y. S.; Koga, T.; Park, S.; Satija, S.; Chen, X.; Yoon, K.; Hsiao, B. S.; Sokolov, J. C.; *et al.* Stabilizing Thin Film Polymer Bilayers against Dewetting Using Multiwalled Carbon-Nanotubes. *Macromolecules* **2007**, *40*, 9510–9516.
- (158) Kim, T.-H.; Kim, H.; Choi, K.-I.; Yoo, J.; Seo, Y.-S.; Lee, J.-S.; Koo, J. Graphene Oxide Monolayer as a Compatibilizer at the Polymer– Polymer Interface for Stabilizing Polymer Bilayer Films against Dewetting. **2016**.
- (159) Moon, R. J.; Martini, A.; Nairn, J.; Simonsen, J.; Youngblood, J. *Cellulose Nanomaterials Review: Structure, Properties and Nanocomposites*; 2011; Vol. 40.
- (160) Kuo, S. W. Hydrogen-Bonding in Polymer Blends. *J. Polym. Res.* **2008**, *15*, 459–486.

- (161) Qin, X.; Xia, W.; Sinko, R.; Keten, S. Tuning Glass Transition in Polymer Nanocomposites with Functionalized Cellulose Nanocrystals through Nanoconfinement. *Nano Lett.* **2015**, *15*, 6738–6744.
- (162) Bates, F. S.; Fredrickson, G. H. Block Copolymer Thermodynamics: Theory and Experiment. *Annu. Rev. Phys. Chem.* **1990**, *41*, 525–557.
- (163) Bates, F. S.; Fredrickson, G. H. Block Copolymers—Designer Soft Materials. *Phys. Today* **1999**, *52*, 32–38.
- (164) Park, S.; Lee, D. H.; Russell, T. P. Self-Assembly of Block Copolymers on Flexible Substrates. *Adv. Mater.* **2010**, *22*, 1882–1884.
- (165) Singh, G.; Batra, S.; Zhang, R.; Yuan, H.; Yager, K. G.; Cakmak, M.; Berry, B.; Karim, A. Large-Scale Roll-to-Roll Fabrication of Vertically Oriented Block Copolymer Thin Films Large-Scale Roll-to-Roll Fabrication of Vertically Oriented Block Copolymer Thin Films * Correspondence to : **2013**, 5291–5299.
- (166) Cho, J. H.; Katsumata, R.; Zhou, S. X.; Kim, C. Bin; Dulaney, A. R.; Janes, D. W.; Ellison, C. J. Ultrasoother Polydopamine Modified Surfaces for Block Copolymer Nanopatterning on Flexible Substrates. *ACS Appl. Mater. Interfaces* **2016**, *8*, 7456–7463.
- (167) David S. Fryer; Richard D. Peters; Eui Jun Kim; Jeanne E. Tomaszewski; Juan J. de Pablo, and; Nealey*, P. F.; and, C. C. W.; Wu, W. Dependence of the Glass Transition Temperature of Polymer Films on Interfacial Energy and Thickness. **2001**, 5627–5634.
- (168) Alvine, K. J.; Ding, Y.; Douglas, J. F.; Ro, H. W.; Okerberg, B. C.; Karim, A.; Soles, C. L. Capillary Instability in Nanoimprinted Polymer Films. *Soft Matter* **2009**, *5*, 2913.
- (169) Bohme, T. R.; De Pablo, J. J. Evidence for Size-Dependent Mechanical Properties from Simulations of Nanoscopic Polymeric Structures. *J. Chem. Phys.* **2002**, *116*, 9939–9951.
- (170) Yoshimoto, K.; Jain, T. S.; Nealey, P. F.; De Pablo, J. J. Local Dynamic Mechanical Properties in Model Free-Standing Polymer Thin Films. *J. Chem. Phys.* **2005**, *122*, 1–6.
- (171) Posocco, P.; Posel, Z.; Fermeglia, M.; Lísal, M.; Pricl, S. A Molecular Simulation Approach to the Prediction of the Morphology of Self-Assembled Nanoparticles in Diblock Copolymers. *J. Mater. Chem.* **2010**, *20*, 10511.
- (172) Stafford, C. M.; Harrison, C.; Beers, K. L.; Karim, A.; Amis, E. J.; VanLandingham, M. R.; Kim, H.-C.; Volksen, W.; Miller, R. D.; Simonyi, E. E. A Buckling-Based

Metrology for Measuring the Elastic Moduli of Polymeric Thin Films. *Nat. Mater.* **2004**, 3, 545–550.